FEDERAL UNIVERSITY OF SÃO CARLOS
CENTER FOR EXACT SCIENCES AND TECHNOLOGY
POST-GRADUATION PROGRAM IN MATERIALS SCIENCE AND ENGINEERING

THE EFFECT OF CHEMICAL COMPOSITION ON THE MICROSTRUCTURE AND MECHANICAL PROPERTIES OF Ti-Nb-Mo THIN FILMS DEPOSITED BY DCMS ON AISI 316L SUBSTRATE FOR BIOMEDICAL APPLICATIONS

Katherine Judith Martínez Orozco

São Carlos - SP
2025

FEDERAL UNIVERSITY OF SÃO CARLOS
CENTER FOR EXACT SCIENCES AND TECHNOLOGY
POST-GRADUATION PROGRAM IN MATERIALS SCIENCE AND ENGINEERING

THE EFFECT OF CHEMICAL COMPOSITION ON THE MICROSTRUCTURE AND MECHANICAL PROPERTIES OF Ti-Nb-Mo THIN FILMS DEPOSITED BY DCMS ON AISI 316L SUBSTRATE FOR BIOMEDICAL APPLICATIONS

Katherine Judith Martínez Orozco

Doctoral Thesis presented to the Graduation Program in Materials Science and Engineering as a partial requirement to obtain the title of DOCTOR IN MATERIALS SCIENCE AND ENGINEERING

Advisor: Prof. Pedro Augusto de Paula Nascente, Ph.D.
Funding agency: CAPES process 88882.332730/2019-01

São Carlos - SP
2025

DEDICATED

To God, to my mother Fides, my daughter Gaby, my grandmother Alba and in memory of my father Marco, who would be happier and prouder than anyone for the achievement of his daughter.

VITAE

Master of Science degree in Materials Science and Engineering received by the Federal University of São Carlos (UFSCar), (2018)
Bachelor’s degree in Materials Engineering, received by Universidad Autónoma del Caribe (Uniautonoma) (2016)

UNIVERSIDADE FEDERAL DE SÃO CARLOS

Centro de Ciências Exatas e de Tecnologia
Programa de Pós-Graduação em Ciência e Engenharia de Materiais

Folha de Aprovação

Defesa de Tese de Doutorado da candidata Katherine Judith Martinez Orozco, realizada em 30/01/2025.

Comissão Julgadora:

Prof. Dr. Pedro Augusto de Paula Nascente (UFSCar)

Prof. Dr. José Eduardo Spinelli (UFSCar)

Prof. Dr. Claudemiro Bolfarini (UFSCar)

Prof. Dr. Carlos Roberto Grandini (UNESP)

Prof. Dr. Diego Rafael Nespeque Correa (UNESP)

O Relatório de Defesa assinado pelos membros da Comissão Julgadora encontra-se arquivado junto ao Programa de Pós-Graduação em Ciência e Engenharia de Materiais.

ACKNOWLEDGMENTS

I want to express all my gratitude to the Almighty, The Holy God of Israel, without him nothing of this would be possible. Only he gave strength to finish this work.

I am really grateful with the Postgraduate Program in Materials Science and Engineering (PPGCEM) at the Federal University of São Carlos and the entire professor's council, for the knowledge shared that contributed to my academic training, especially with my advisor, Prof. Pedro Augusto de Paula Nascente, who gave me the opportunity to be part of his research group, for his patience, advice and support. Also, thanks to the Laboratory of Structural Characterization (LCE/DEMa/UFSCar). Thanks to Prof. Guilherme Zepon for his collaboration in Thermodynamic calculations, and to Prof. Carlos Alberto Della Rovere for the support in the corrosion tests.

This study was financed in part by the Coordenação de Aperfeiçoamento de Pessoal de Nível Superior - Brasil (CAPES) - Finance Code 001. I want to thank CAPES - Coordination for the Improvement of Higher Education Personnel for the financial support to carry out this work with a scholarship, process number 88882.332730/2019-01

FAPESP is acknowledged for financial support within the FAPESP projects with the following grant: FAPESP (process 2017/25983-8).

CNPq is acknowledged for financial support within the CNPq projects with the following grant: CNPq (grant 303802/2021-6).

CNPEM/LNNano is acknowledged for financial support within the the following: CNPEM/LNNano (proposal 20240541).

The author would like to thank Angelo L. Gobbi from CNPEM/LNNano, for his assistance in the production of the thin films, and Prof. Haroldo C. Pinto, as well as Dr. Raíra Chefer Apolinario, from USP/EESC, for their assistance in some of the analysis. To Dr. María Helena Ramirez Acosta from LaMaV for her support with nanoindentation tests.

I want to thank all my colleagues from PPGCEM and for their discussions, suggestions, and valuable help during these doctoral years. Especially to

Doctors: Cesar Adolfo Escobar Claros, Brenda Juliet Martins, Cristie Luis Kugelmeier and Ernesto David Gonzalez Cruz for their academic advice and support during the research, also very especial thanks to Bruno Barbosa de Aquino, M.Sc.

I would like to express my especial thanks to my friends: Cesar, Shirly, Nicolas, Aldair, Juan Pablo, Cris, Brenda, for all the unconditional support and friendship, for encouraging me to go on in this journey and not to give up.

All my gratitude to my mom Fides, my daughter Gaby, to my family, and last but not least, to my love José Zapelini for his support. Thank all of you guys, for your support, patience and unconditional love!

RESUMO

O EFEITO DA COMPOSIÇÃO QUÍMICA NA MICROESTRUTURA E NAS PROPRIEDADES MECÂNICAS DE FILMES FINOS DE Ti-Nb-Mo DEPOSITADOS POR DCMS EM SUBSTRATO AISI 316L PARA APLICAÇÕES BIOMÉDICAS

O objetivo deste trabalho é estudar o efeito da composição química na microestrutura e nas propriedades mecânicas de cinco filmes finos de ligas β de titânio: $Ti_{74}Nb_{21}Mo_{5}$, $Ti_{74}Nb_{19}M_{7}$, $Ti_{72}Nb_{19}Mo_{9}$, $Ti_{67}Nb_{22}Mo_{11}$, and $Ti_{71}Nb_{29}$ (como referência) depositados em substratos de aço AISI 316 L. Filmes com espessuras de 671 nm, 573 nm, 841 nm, and 963 nm foram depositados por meio da técnica de pulverização magneto-catódica de corrente direta (DCMS). A caracterização microestructural foi realizada por microscopia eletrônica de varredura (MEV) acoplada à espectroscopia de raios X por dispersão de energia (EDS), microscopia de força atómica (AFM), e difração de raios X por incidência de ângulo rasante (GIXRD). As propriedades mecânicas foram avaliadas por meio de ensaios de nanoindentação, tensão residual e polarização potenciodinâmica. Em geral, foram obtidos filmes finos homogêneos com tamanhos de grão nanométricos. Os filmes apresentaram aglomerados e poros. Foram medidas tensões residuais compressivas e trativas, e foram encontrados resultados expressivos relacionados à morfologia dos filmes. Quanto mais homogêneo o filme, maior o valor da tensão residual compressiva. Foi observada uma relação Hall-Petch inversa, explicada pela diminuição dos valores de dureza acompanhada da redução no tamanho de grão.

Keywords: Pulverização magneto-catódica de corrente direta; filmes finos; recobrimentos; corrosão; propriedades mecânicas; ligas Ti-Nb-Mo; ligas biomedicas; módulo elástico; nanoindentação; tensão residual; GIXRD.

ABSTRACT

The aim of this work is to study the effect of chemical composition on the microstructure and mechanical properties of five titanium β-alloys thin films: $Ti_{74}Nb_{21}Mo_5$, $Ti_{74}Nb_{19}M_7$, $Ti_{72}Nb_{19}Mo_9$, $Ti_{67}Nb_{22}Mo_{11}$, and $Ti_{71}Nb_{29}$ (as reference) deposited on AISI 316 L substrates. Films having thicknesses of 671 nm, 573 nm, 841 nm, and 963 nm were deposited by means of direct current magnetron sputtering (DCMS). Microstructural characterization was carried out by scanning electron microscopy (SEM) coupled with energy-dispersive X-ray spectroscopy (EDS), atomic force microscopy (AFM), and grazing incidence X-ray diffraction (GIXRD). The mechanical properties were tested by means of nanoindentation test, residual stress, and potentiodynamic polarization test. In general, homogeneous thin films were obtained with nanometric grain sizes. The films exhibit clusters and pores. Compressive and tensile residual stress were measured, and expressive results correlating with the morphology of the films were found. As more homogeneous the thin film, the higher the compressive stress value. Inverse Hall-Petch relation was observed, explained by the decreasing in the hardness values simultaneously with decreasing in grain size.

Keywords: Direct current magnetron sputtering; thin-films; coatings; corrosion; mechanical properties; Ti-Nb-Mo alloys; biomedical alloys; elastic modulus; nanoindentation; residual stress; GIXRD.

PUBLICATIONS

K.J. Martinez-Orozco, R.A. Chefer, P.T. Avila, H.C. Pinto, V.R. Mastelaro; P.A.P. Nascente. **The effect of thickness on Ti80-Nb20-based alloys coatings deposited DCMS on AISI 316L substrate for biomedical applications.** XIX Brazil MRS Meeting, held in online format, from August 30th to September 03rd, 2021.

C. R. M. Afonso, K.J. Martinez-Orozco, J. E. Spinelli, V. Amigó, C. A. Della Rovere, C. S. Kiminami. **Characterization, corrosion resistance and hardness of rapidly solidified Ni-Nb alloys.** *Journal of Alloys and Compounds*, *829*, 154529. doi.org/10.1016/j.jallcom.2020.154529.

TABLE OF CONTENTS

LIST OF TABLES

LIST OF FIGURES

LIST OF SIMBOLS AND ABREVIATIONS

AC	Alternating current
A	Atomic mass
Z	Atomic number
BCC	Body centered cubic
CP	Commercially pure titanium
ρ	Density
DCMS	Direct current magnetron sputtering
E	Elastic modulus
χ	Electronegativity
ECR	Electron cyclotron resonance
H	Hardness
HCP	Hexagonal close packed
HiPIMS	High power impulse magnetron sputtering
IE	Ionization energy
M_p	Melting point
PVD	Physical vapor deposition
v	Poisson ratio
RF	Radio frequency
G	Shear modulus
sccm	Standard cubic centimeters per minutes
T	Temperature
$T_{Transus}$	Transus temperature

1 INTRODUCTION

The field of biomaterials is continually expanding, a multidisciplinary hub where diverse knowledge areas meet with the common objective to design and manufacture medical devices to improve the quality of life in humans (e.g. total hip joint replacement) and in some cases save the patients' lives (e.g. stents, pacemakers). The development of new, superior, cheaper, and available biomaterials mainly involves biomedical, mechanical, and materials engineering with the direct and indirect intervention of other diverse disciplines associated (i.e. biology), and it currently exists countless technologies and materials used to pursue that common goal.

Surface engineering is one of those technologies, which is continuously on development, not only at service of the automotive, aerospace or communications areas, but for sure has thrived in the biomedical field. The main objective of surface engineering is to improve the properties of a substrate by either modifying its surface or adding another material onto it, or a combination of both processes [1].

For biomedical applications the most common materials utilized for prosthetics are metals, since, in many cases, they exhibit the most suitable features for a required application (i.e. high strength, high corrosion resistance, and biocompatibility). Due to many of the existing metallic biomaterials present disadvantages regarding to their chemical composition (i.e. stainless steels, nickel-based alloys), that may result toxic for human tissue or cause allergies if used at long term, or due to their high cost (i.e. titanium-based alloys and precious metals), the surface engineering enlarges the possibilities to produce devices with the best characteristics of a substrate/coating system to meet the conditions for an optimal performance at lower cost.

This is one of the main reasons that titanium-based alloys are, by far, among the better options for biomedical applications (i.e. Ti6Al4V, Ti6Al7Nb). Titanium exhibits high strength/density ratio, superior corrosion resistance, biocompatibility, and it is known that CP-Ti promotes the osteointegration process in the implants [2]. However, its high cost is the principal drawback, hence the utilization of titanium-based alloys as coatings offers a promising solution. At this moment, there are a wide variety of deposition processes that are being explored to manufacture biomedical devices and implants. The physical vapor deposition (PVD) processes belong to this group, consisting of the evaporation of a material in the solid state by the bombardment of its surface with energetic ions that are further deposited on a substrate [3]. The direct current magnetron sputtering (DCMS) is a PVD process employed to deposit coatings that present excellent characteristics. At this moment, this process seems to offer coatings with good adhesion, wear and corrosion resistance, among other desirable properties [1].

In our research group we have studied Ti-Nb-based thin films deposited with DCMS process, varying deposition parameters and chemical composition (i.e. Ti-Nb-Zr, Ti-Nb-Mg and Ti-Nb-Mo), always depositing films with thicknesses less than 1 µm and deposited onto silicon or ASTM 316L substrates [4]. This work is part of the research sequence on Ti-Nb-based alloys, whose objective is to explore different chemical compositions on the Ti-Nb-Mo thin films coatings in order to assess their influence on the mechanical properties. This is a next step to get closer to the objective of implementing this process commercially, specifically for the implant market.

This is an exploratory work with the purpose of producing Ti-Nb-Mo thin films with different chemical compositions, deposited on AISI 316L stainless steel substrate, for biomedical applications, such as in prosthetics. The depositions were carried out by means of DCMS process. Then, the microstructure and mechanical properties were evaluated with the aim to analyze the effect of the chemical composition on the mechanical properties and microstructure.

2 SCIENTIFIC BACKGROUND

2.1 Physical Vapor Deposition (PVD) Processes

In the surface engineering field, the main goal is to improve the properties of a substrate by either modifying its surface or adding another material onto it, or a combination of both processes [1]. Metal, polymers, and ceramic surfaces are enhanced by the deposition of coatings with a combination of materials (e.g. metal-ceramic) or with the same material type (e.g. metal-metal). Sometimes the substrate surface is modified before a coating deposition, and in other cases the coating surface is submitted to a further treatment to be modified. A wide variety of methods exists, in surface engineering, and they are employed to satisfy a specific requirement. For coatings and thin films deposition, the most common methods are classified into two groups according to the type, i.e. occurring at atomistic/molecular or at bulk level. The atomistic deposition is subdivided into several categories depending on the environment: electrolytic, vacuum (e.g. vacuum evaporation), plasma (e.g. sputter deposition), chemical vapor (e.g. chemical vapor deposition, CVD.), chemical solution, thermal spray, impact and plating. For bulk coatings there are: chemical solvent deposition, fusion coatings (e.g. sol-gel) [1, 3]. In Table 2.1 these groups of surface engineering processes are listed [3].

The so-called PVD belongs to the atomistic deposition family and encompasses a group of overlay processes consisting of the vaporization of a material in solid or liquid phase (the target), where atoms are removed by bombarding the surface with high energy ions. The removed species travel through the chamber either in low pressure-plasma or vacuum environment (under 10^{-4} Pa), until they are finally deposited onto the substrate surface [1, 3, 5]. PVD can be classified according to the methods to remove the atoms from the target, i.e. sputtering (momentum transference) and evaporation (application of thermal energy) and it is subdivided into four basic categories: vacuum deposition, sputter deposition, arc vapor deposition, and ion plating [3].

Table 2.1 – Atomistic/molecular and bulk coatings deposition and processes employed in surface engineering [1].

Atomistic / Molecular Deposition	Bulk Coatings
Electrolytic Environment	***Wetting Processes***
Electroplating	Dip coating
Electroless plating	Spin coating
Displacement plating	Painting
Electrophoretic deposition	***Fusion Coatings***
Vacuum Environment	Thick films
Vacuum evaporation	Enameling
Ion beam sputter deposition	Sol-gel coatings
Ion beam assisted deposition (IBAD)	Powder coating
Laser vaporization	***Solid Coating***
Hot-wire and low pressure CVD	Cladding
Jet vapor deposition	Weld overlay
Plasma Environment (PVD PHYSICAL PAV)	Gilding
Sputter deposition	***Surface Modification***
Arc vaporization	***Chemical Conversion***
Ion plating	Wet chemical solution (dispersion & layered)
Plasma enhanced (PE) CVD	Gaseous (thermal) plasma
Plasma polymerization	**Electrolytic Environment**
Chemical Vapor Environment	Anodizing
Chemical vapor deposition (CVD)	Ion substitution
Pack cementation	Plasma electrolysis
Chemical Solution	***Mechanical***
Spray pyrolysis	Shot peening
Chemical reduction	Work hardening
Particulate Deposition	***Thermal Treatment***
Thermal Spray	Thermal stressing
Flame spray	***Ion Implantation***
Arc-wire spray	Ion beam
Plasma spraying	Plasma immersion ion implantation (PIII)
D-gun	***Roughening and Smoothing***
High-velocity-oxygen-fuel (HVOF)	Chemical
Impact Plating	Mechanical
Mechanical plating	Chemical–mechanical polishing
	Sputter texturing
	Enrichment and Depletion
	Thermal
	Chemical

A scheme of the PVD configurations is illustrated in Figure 2.1. PVD techniques are used to manufacture multilayer coatings and thin films [1, 3, 5]. In general, thin films are those with thickness less than 1 µm [1, 3].

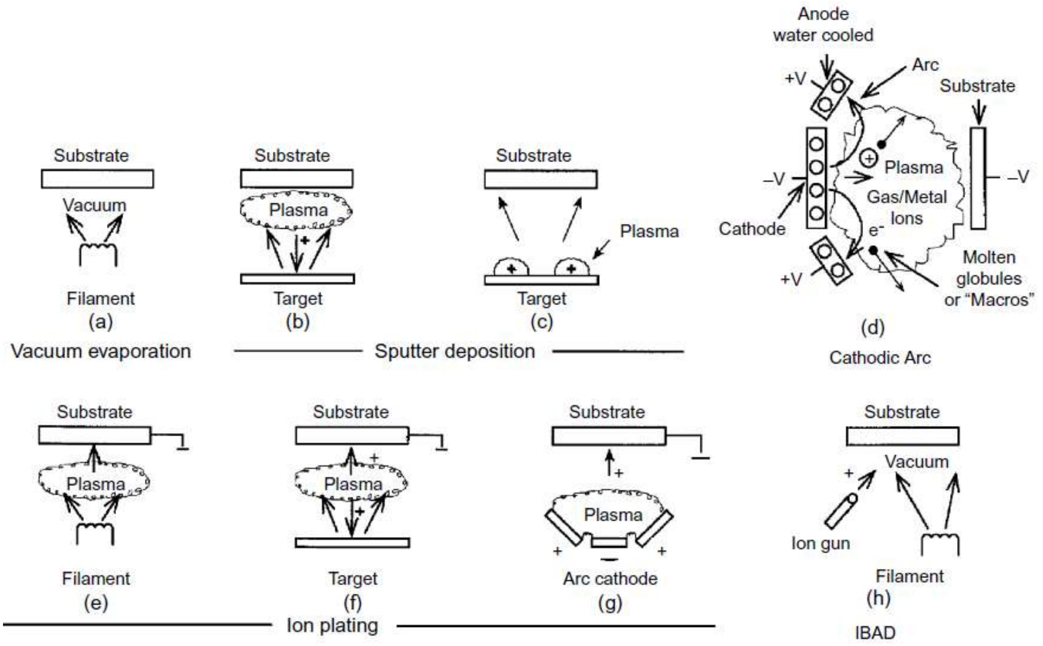

Figure 2.1 – Illustration of the different PVD processes: a) Vacuum evaporation, b) and c) Sputter deposition in plasma environment, d) Sputter deposition vacuum, e) Ion plating in plasma environment with a thermal evaporation source, f) ion plating with a sputtering source, g) Ion plating with an arc vaporization source and h) Ion beam-assisted deposition (IBAD) with thermal evaporation source and ion bombardment from an ion gun [1, 3].

2.1.1 Sputter Deposition

The sputter deposition process (also known as back-sputtering, cathode sputtering or impact evaporation), is a plasma assisted PVD process [3]. Plasma, which is the fourth state of matter, is conventionally produced by the ionization of a neutral gas when it is submitted to extremely high temperatures (about 10^6 K), and this leads to violent collisions between atoms, producing free electrons and positive ions [6, 7, 8]. The density of these charged particles is balanced; thus, plasma is the matter in a particular state that has the fundamental property of global electrical neutrality. It is important to point out that plasma not only exists as gas, but as liquid and solid conductors [9]. Since plasma is an electricity conductor fluid and presents an organized behavior, it results extremely useful to improve the PVD deposition mechanisms. Plasma-assisted deposition presents advantages such as: the improvement of coating adhesion, because plasma can be used to pre-heat and clean the substrate surface by the bombardment of the surface with energetic ions and neutrals. The gas scattering effect and the possibility to rotate and displace the substrates result in the production of uniform coating thickness [6].

Inert (i.e. Ar, Kr) or active (i.e. Hg, O_2 or N_2) gases can be used to create plasma. When active gases are used, the PVD process is named reactive. Frequently the plasmas in the PVD processes present a low degree of ionization, i.e. major quantity of neutral species than ions. To create a good plasma environment, a good vacuum system is required, that ensures a long mean free path for the sputtered adatoms, improving the deposition rate [1]. When charged and energetic particles (accelerated ions) provided by the plasma hit the target surface, removing atoms as depicted in Figure 2.2, physical sputtering process takes place. Part of the sputtered atoms still near the target can be ionized. Depending on the incident ion energy, ion implantation on the target also occurs. The sputtered atoms further condensate on the substrate. Inside the chamber it occus the interaction of the different energetic species such as ions, neutral atoms, neutrons, electrons, and photons [3].

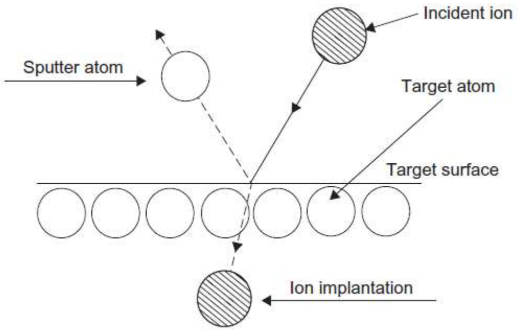

Figure 2.2 – Scheme of the physical sputtering mechanism [3].

The physical sputter deposition is a non-thermal PVD process; the vaporization of the atoms from the sputtering target is non-thermally induced and occurs as result of a momentum transfer of the particles collisions. Vacuum deposition presents higher deposition rates than sputtering, and a solution to this is to low the sputtering pressure to enhance deposition rate [3]. In the plasma environment, the chamber is filled with inert gas (usually argon) that is ionized to create the plasma that can be located near to the target region or occupying the entire chamber. Variations of the different configurations for sputtering deposition systems are: ion bean sputtering (in vacuum), medium-frequency sputtering (alternating current (AC) sputtering), electron cyclotron resonance (ECR) plasma sputtering, direct current (DC) diode sputtering (non-magnetron), radio frequency (RF) diode sputtering, and magnetron sputtering (e.g. direct current magnetron sputtering, DCMS; high power impulse magnetron sputtering, such as direct current magnetron sputtering (DCMS), high power impulse magnetron sputtering (HiPIMS), balanced and unbalanced magnetron sputtering (UBS), and radio frequency magnetron sputtering (RFMS) [1, 3]. The DC diode sputtering is the simplest configuration of the existing sputtering processes, and it consists of a chamber and a pair of planar electrodes as depicted in Figure 2.3 a. One of them is the cold cathode and the other is the anode where the substrate is placed at ground potential. The chamber is filled with gas and a DC potential (several thousand volts) is applied, then the plasma is generated close to the cathode surface. In DC sputtering the target is always a metal [1, 3].

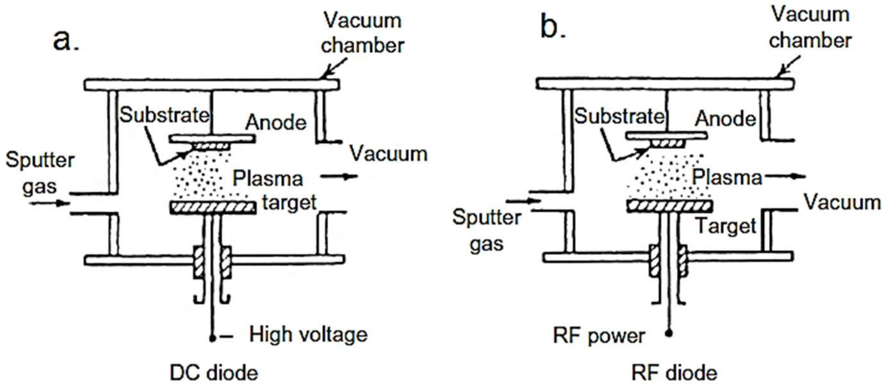

Figure 2.3 – Schematic of the conventional sputtering configurations: a) DC diode evaporation and b) RF diode [3].

For sputter depositions, as for all deposition processes, the main goal is to obtain a film with the best characteristics and properties, but with an acceptable efficiency making the process economically viable. An important variable defining the process efficiency is the rate of deposition (the quantity of atoms successfully deposited on the substrate per time unit), which is directly related with the sputter yield (S), defined as the ratio between the number of atoms removed from the target and the number of incident ions. S depends on a set of variables such as the type of target and its crystal structure, the energy and the incident angle of the incident ions (i.e. S presents a maximum for incident angles between 60° and 80°, above that values S starts to decrease), at the same time it exists an interval of the ion energy, a minimum and a maximum critical values. The minimum must be exceeded in order to sputtering occurs, then S increases until the maximum critical value is reached, S starts to decrease beyond. As well as S, the velocity and the energy of the sputtered species also depend on the energy and the incident angle of the incident ions, and this velocity is higher than the gas molecules [3].

The ion bombardment energy is controlled by a parameter known as the bias voltage. The bias voltage is a DC voltage applied to guarantee adequate operating conditions in the process. A negative bias is applied to the substrate to attract ions from the surrounding plasma in order to increase the substrate ion current and deposition rate. The bias also permits the growth and microstructure of the films [3, 7]. In the case of non-conducting materials, it is necessary to work with pulsed bias, i.e. RF sputtering, as shown in Figure 2.3 b. For non-conducting targets, as is the case of DC sputtering, the surface would be charged with positive ions, disrupting the sputtering discharge. The solution to sustain the glow discharge is to replace the DC for a RF voltage supply [3]. In ion beam sputtering technique, no bias voltage is used. Biasing is applied to the substrate to guarantee a good adhesion of the film. Before deposition, a high bias voltage (approximately 1 kV) is applied, creating glow discharge in order to clean the surface, and a lower voltage is employed during the deposition. It is necessary to maintain certain level of ionization around the substrate to sustain the deposition; this depends on the voltage applied. The bias also helps to accelerate the ions directly to the target, promoting more collisions on the target and rising S, improving the deposition rate, and consequently producing more compact coatings with better characteristics [3].

2.1.2 Direct Current Magnetron Sputtering (DCMS)

As already mentioned, in the DC sputtering configuration a DC voltage is applied to the cathode (the target) yielding to electron ejection. These electrons are accelerated away from the cathode, but they poorly contribute to sustain the discharge. In the magnetron sputtering configuration, a geometrically appropriate array of permanent magnets is placed under the cathode surface, producing a magnetic field that forces the electrons to circulate in the vicinity of the surface, creating a high flux of electrons that increases the plasma density [1]. The two magnetron sputtering configurations, planar and cylindrical (coaxial), are presented schematically in Figure 2.4.

In a planar magnetron different shapes can be used but the most common are rectangular and circular as illustrated in Figure 2.5. The magnets arrangement is inserted under the cathode and are geometrically configurated in a convenient manner to produce a closed path magnetic field of certain dimensions depending on magnets separation, as detailed in Figure 2.5 a. The magnet pattern usually is composed of three bars separated by a gap, disposed down the longitudinal cathode axis, with the two outermost magnets pointing their north pole up and the magnet in the middle pointing its north pole down [10]. The magnetic field (B) contribution on the cathode surface (represented by the red field lines on Figure 2.5 a. is considered to be perpendicular to the electric field E and forms an oblong enclosed path whose width is equal to the gap between magnets.

Secondary electrons are emitted from the cathode and accelerated in direction to the substrate, but the non-uniform magnetic field transverse to the cathode surface acts like a trap and keeps them in the closed trajectory. These electrons produce an erosion pathway on the target surface (the green and blue ones illustrated in Figure 2.5 a. The electron concentration enhances the plasma ionization in the vicinity of the target surface and restricts the discharge to this region, thus plasma density is higher. The higher the plasma density, the higher the current density, i.e. the quantity of ions accelerated from the plasma to hit the target, thus increasing the sputtering rate [3]. For a better understanding on how the DCMS process works an illustrative diagram is presented in Figure 2.6 [11,12,13].

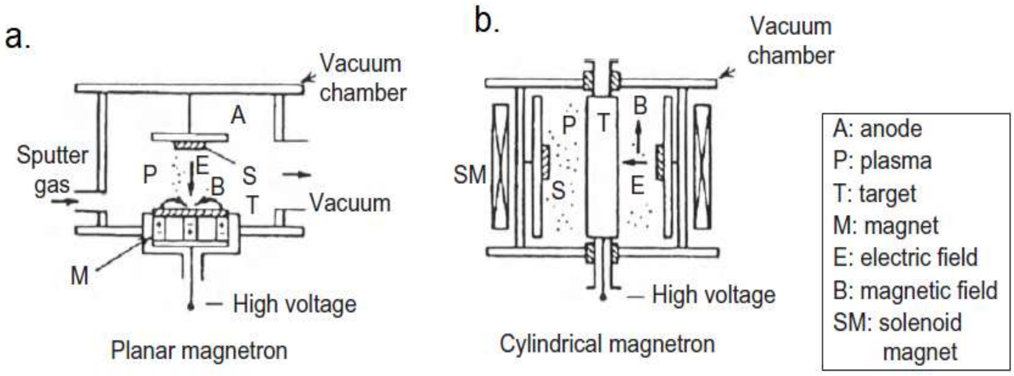

Figure 2.4 – The two configurations of the magnetron sputtering process: a.) Planar magnetron system and b.) Cylindrical magnetron system [3].

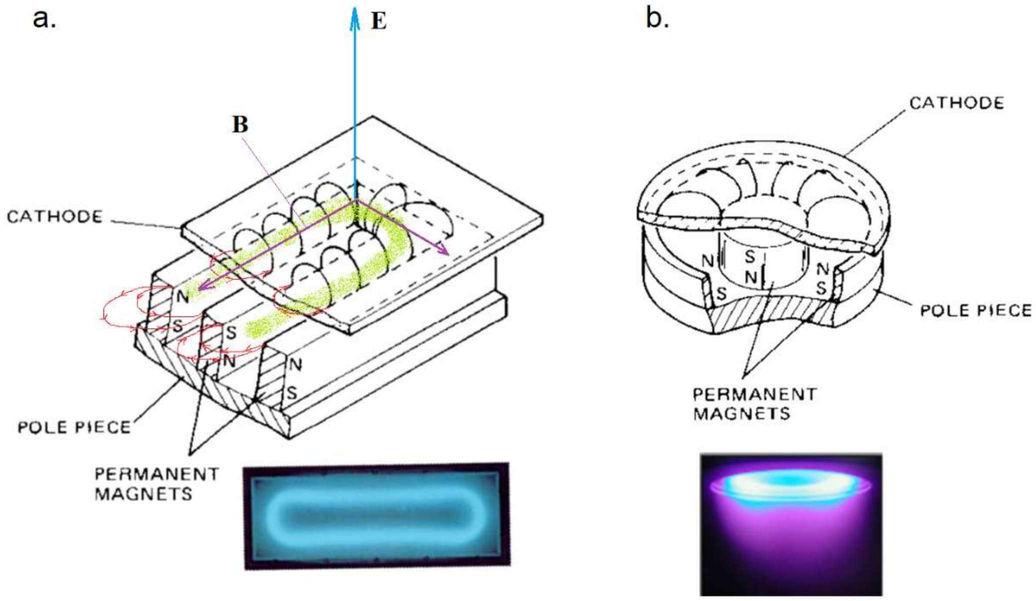

Figure 2.5 – The permanent magnets array under the cathode in the planar magnetron sputtering configuration: a.) rectangular and b.) circular. [9, 10, 12]

When the erosion patterns on the target surface appear with abnormal shapes, this is used as indicators and in the diagnosis of a possible issue with the magnets, i.e. misalignment or missing of one of them.

DCMS occurs at lower potential (300 – 700 V) and lower pressure (between 1 to 10 mTorr) as compared with DC sputtering [10]. The low pressure inside the chamber inhibits the sputter particles from colliding while they travel to the substrate, as a consequence a higher deposition rate is observed [3]. A clear disadvantage regarding the non-uniformity of the plasma is that it leads to a non-uniform utilization of the target as well. This is a noticeable disadvantage since only 10% to 30% of the target is used [1, 3].

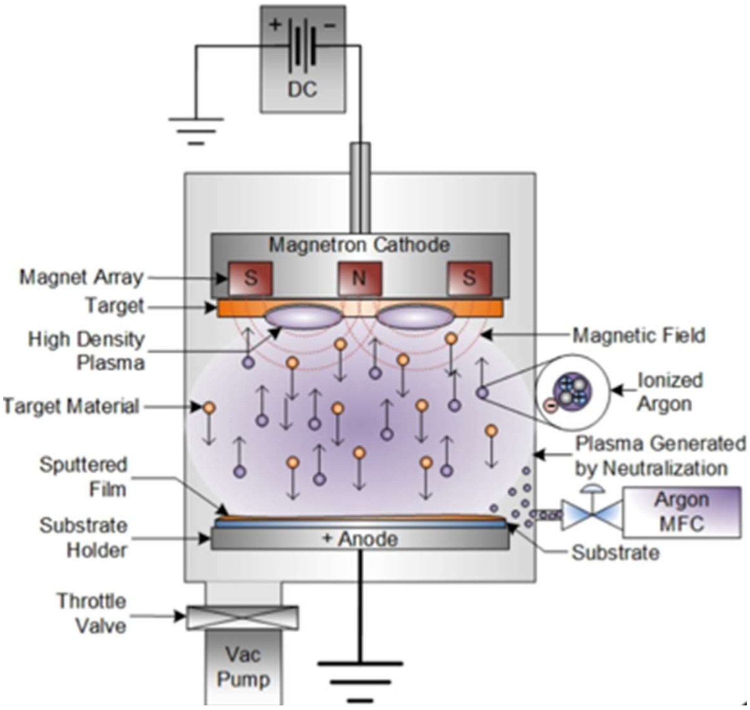

Figure 2.6 Illustration of the DC magnetron sputtering deposition process [13].

2.1.3 Balanced and unbalanced DCMS

As mentioned previously, in magnetron sputtering process, a target material is bombarded with energetic ions, causing atoms from the target to be ejected and deposited onto a substrate. A magnetic field is used to trap electrons near the target, enhancing ionization of the plasma and improving the sputtering efficiency. Balanced and unbalanced direct current magnetron sputtering are specific configurations of the magnetic field in the magnetron sputtering process [1].

In the balanced DCMS configuration, all the magnets have the same power, and all the field lines out of the external magnets pass through the central magnet. The magnetic field lines are closed, and the electrons cannot escape from the magnetic field. As a result, the plasma remains only around the cathode (i.e. the target). The magnetic field lines are designed so that the inward (towards the substrate) and outward (away from the substrate) magnetic flux densities are equal or nearly equal. This balance ensures that the plasma remains confined (dense plasma) near the target, reducing plasma dispersion toward the substrate.

This is ideal for efficient sputtering, however, the reduced plasma density near the substrate may limit ion bombardment effects on the growing film [1, 3]. The balanced magnetron sputtering configuration is depicted in Figure 2.7 a.

Plasma can reach a region up to 60 mm high from the target surface. If the substrate is placed out of this region, the ion flux on the substrate will be not enough (< 1 mA/cm^2) for surface modifications. Higher energy ions bombarding the substrate can be supplied by applying bias voltage on the substrate, but it results in more defects and stress in the layer and in general, deteriorates layer properties [14].

On the other hand, for unbalanced DCMS the configuration of the magnetic field, the configuration allows some magnetic field lines to extend beyond the target region, reaching toward the substrate as depicted in Figure 2.7 b. and c (Type I and II unbalanced DCMS, respectively). The magnetic field near the target is intentionally unbalanced, thus the magnetic flux density is stronger in just one direction (usually outward). This allows a portion of the electrons and plasma to escape the target vicinity and move toward the substrate. Higher plasma density concentrates near the substrate, increasing the ion flux reaching the film during deposition, which helps to improve the film properties, such as adhesion and density (reduced porosity). Due to the higher energy of the ions, higher residual stress can be induced in the film, impacting its long-term stability [3].

The unbalanced DCMS can be configurated with the central magnet stronger than the ring magnet (type 1). Here, the unclosed magnetic field lines are pointed toward the chamber walls and the plasma density in the substrate region is low. This configuration is not commonly used due to its insufficient ion current on the substrate [14]. In Table 2.2 are listed some aspects of balanced and unbalanced DCMS for comparative purposes.

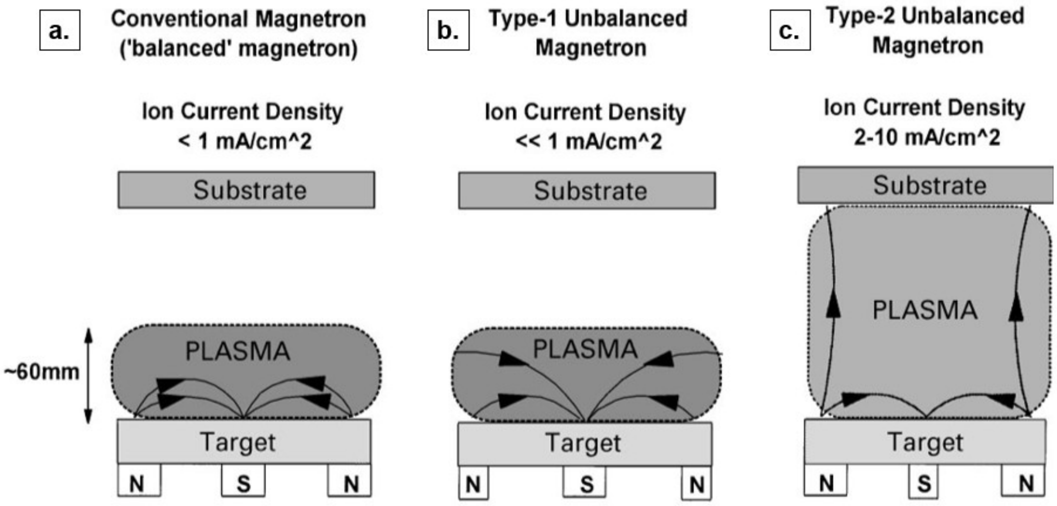

Figure 2.7 – Configuration of balanced and unbalanced DCMS [14].

Table 2.2 – Comparative aspects between balanced and unbalanced DCMS configuration [14].

Aspect	Balanced DCMS	Unbalanced DCMS
Magnetic field	Plasma confined near the target	Plasma extends toward the substrate
Plasma density (near substrate)	Lower	Higher
Ion bombardment	Minimal	Significant
Film adhesion	Moderate	Enhanced
Residual Stress	Lower	Higher
Substrate heating	Minimal	Higher

2.2 Microstructural aspects of films deposited by magnetron sputtering

From the fundamental knowledge in materials science and engineering, one understands the correlation among the four principles that govern the materials design, i.e. processing, structure, properties, and performance. Keeping that in mind, the parameters of the deposition process must be carefully set in order to achieve the best film features and properties to guarantee the optimum performance of the final product. From section 2.1.1, it can be understood that most of the parameters in the deposition system affect directly the sputter yield, the deposition rate, the nucleation, and growth mechanisms. The list of parameters is proportional to the process complexity, but there are three of them with high relevance: the power input density (a determinant factor for the sputter yield), a high vacuum that guarantees a long enough mean free path, and the bias voltage applied to the substrate to improve the deposition rate [1].

The type of film formed will vary as a function of the deposition conditions, and may result in amorphous, mono or poly-crystalline coatings [3]. In practice, the film growth may occur through various mechanisms, the most common are the polycrystalline films exhibiting in general columnar growth whose preferential orientation is led by the crystallographic orientation of the substrate surface, i. e. epitaxy [15]**.** When a crystalline layer of one material (i. e. the epitaxial layer) grows on the surface of a crystalline substrate made of a different material, the substrate and the epitaxial layer typically have different crystal lattice constants, presenting crystal misfit, and this is known as heteroepitaxy [16]. The occurrence of small lattice mismatch can lead to strain, that will influence the properties of the material. Thin epitaxial layers will present strain due to the conformation to the substrate lattice structure, on the other hand, in thicker layers, it occurs relaxation of such strains, leading to defects (e.g. dislocations). Although the substrate and the coating must present different chemical compositions, in some cases they can share similarities as having the same crystal structure, which ensures an orderly growth [16].

The film growth is initiated by the adatoms (sputtered atoms from the target) condensing on the substrate surface, this phenomenon occurs far from equilibrium due to the growth conditions such as: the high cooling rates (e.g. 10^{13} $K.s^{-1}$), the deposition temperature being around $0.7T_m$ of the target material, and the high deposition rates about 10^{17} atoms/m^2s, and all of them contribute to the formation of coatings with metastable phases and with unique properties as compared with bulk material [17]. Figure 2.8 presents the growth stages of a polycrystalline coating, the most common practical case of island-type nucleation and growth. The atoms condense randomly on the substrate surface, but eventually they form islands of atoms (a statistical process of nucleation), then these islands start to grow until coalescence occurs, leading to the formation of a polycrystalline coating [17].

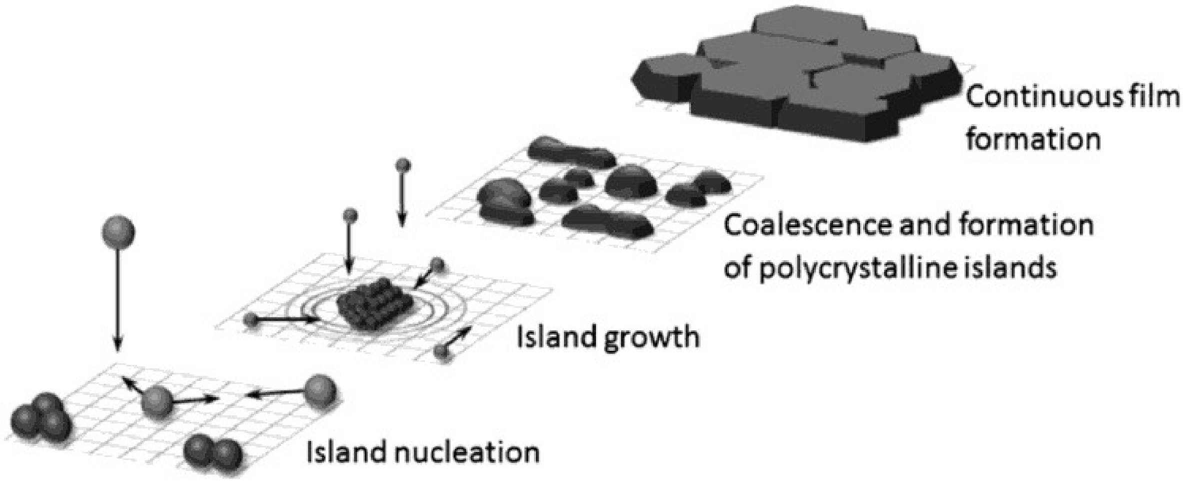

Figure 2.8 – Growth stages of polycrystalline films [17].

The coating morphology, topography, and microstructure are a function of the substrate characteristics and its temperature [3, 17]. An attempt to predict, in a qualitative way, the growth evolution of films and coatings as function of some deposition parameters is the so-called structure zone diagrams (SZD). The first model of an SZD for single-phase films was proposed in 1969 by Movchan and colleagues [18], and it is a practical approach to describe the microstructure, consisting of a diagram of the film area divided into three different regions. Sabet *et al.* [19] used the Movchan's SZD, as depicted in Figure 2.9, to illustrate the microstructural evolution of a CsI:Tl film on a silicon photomultiplier as function of temperature. Each zone in the diagram represents the microstructure evolution depending on the ratio between the substrate temperature (T_s) and the melting point of the film material (T_m), known as the homologous temperature (T_h). A continuous increment of T_h is observed from zone 1 to 3. In zone 1, when $T_h < 0.2$ the condensed atoms have low mobility, they tend to remain in the same place nucleating grains with coarse and crowded and messy-like appearance, oriented with the arriving vapor flux, and the grain size is determined by the nucleation density. These grains present many point defects such as pores and voids [15, 20]. Between 0.3 and 0.5, the atoms present mobility such that cause the growth of uniform columnar grains, and the grain size continues increasing as function of T_h, but at some point, at higher temperatures recrystallization occurs, and the film becomes denser with larger grains [19].

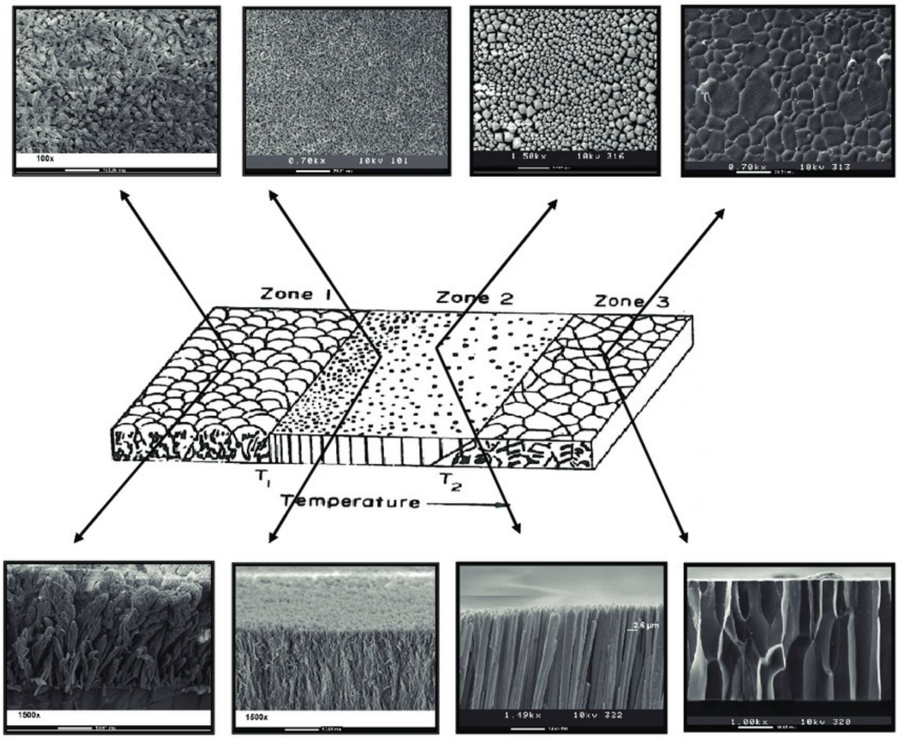

Figure 2.9 – Illustration of a polycrystalline CsI:Tl film on a SiPM microstructural evolution as function of temperature, correlated with the Movchan’s Structure Zone Diagram [18, 19].

In 1998, Barna and colleagues [21] published a modified version of the Movchan’s SZD, as illustrated in Figure 2.10, that includes a new transition intermediate zone, named zone T located between zones 1 and 2 that occurs in an interval of T_h values about 0.2 to 0.4. This diagram is a qualitative description as well as Movchan’s and the representation of zones 1, T, and 2 considers an impurity-free deposition, while for zone 3 it is considered the presence of low impurity concentration [22].

In this case, the surface diffusion is the main variable leading to the grain growth that presents competitive character at the interface, producing dense and fibrous structures. The ion bombardment produces defects on the film that induce a continuous re-nucleation disrupting the columnar growing and producing a cone-like morphology [22 – 24].

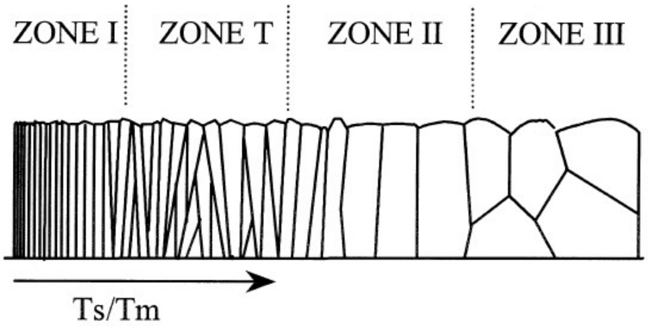

Figure 2.10 – The SZD modified by Barna, showing the introduction of a new transition intermediate zone, the zone T [21, 24].

The most recent diagram, depicted in Figure 2.11, was proposed by Anders [20] in 2010 and is an extended version of the SZD that includes the plasma and ions effect on the film growth. The modified diagram includes a few changes: the x axis represents a generalized temperature T^*, instead of only the T_s/T_m ratio, and the temperature shift originated by the potential energy of the arriving particles. The potential energy includes the heat of sublimation and the ionization energy. The y axis is a normalized energy E^*, that represents the displacement of the heating effect caused by the kinetic energy contribution of the atoms when they impact the surface. Finally, the z axis represents t^*, the net thickness of the film, indicating the reduction caused by ion etching on the surface that erodes the surface producing a "negative thickness" [20].

Figure 2.12 shows the cross-section SEM images of tantalum thin films on a silicon substrate deposited by HiPIMS and DCMS on a cavity with 1 cm^2 and 2 cm depth. The growth of the thin film deposited by HiPIMS was columnar and perpendicular to the interface according to zone 2 type, while the film deposited by DCMS presented pores and a tilted columnar growth, resulting from an effect known as atomic shadowing that is suppressed on the HiPIMS. As mentioned earlier, HiPIMS represent an excellent alternative for deposition on complex-shaped substrates [22].

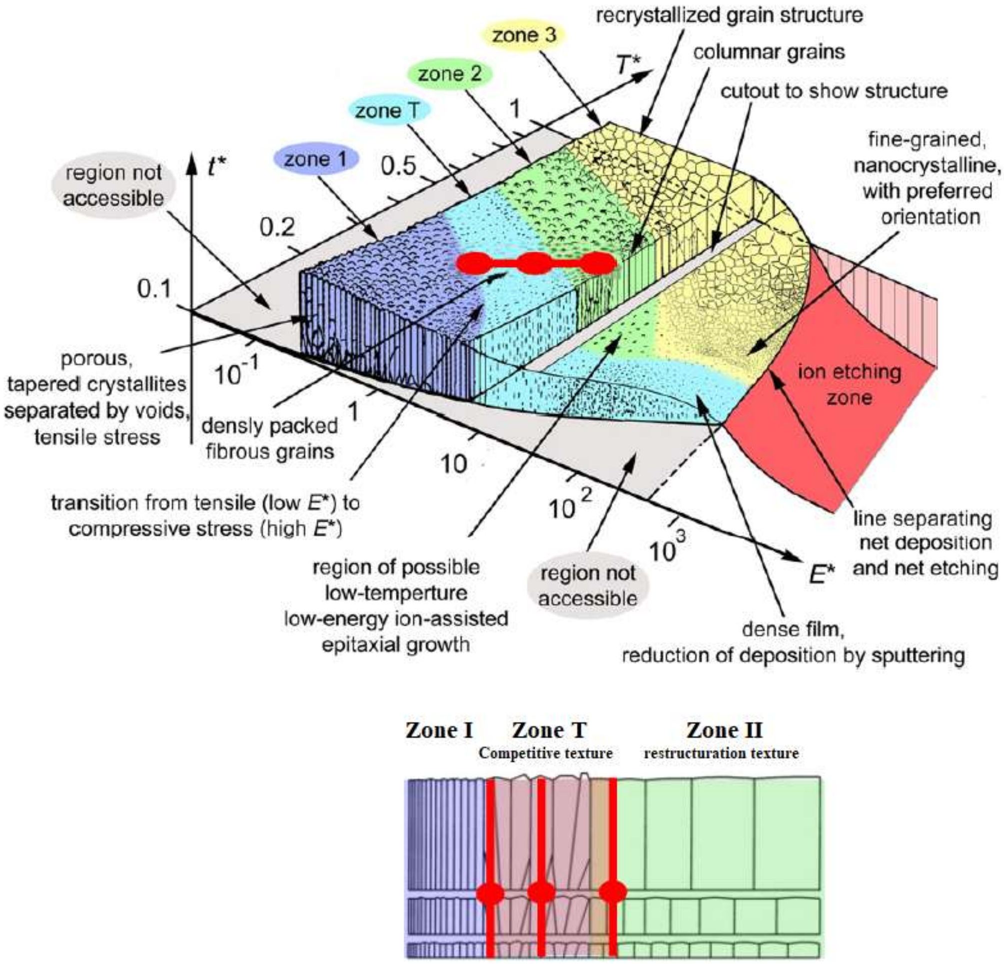

Figure 2.11 – Illustration of the SZD proposed by Anders, which includes a new eroded region cause by plasma and ions bombardment [20].

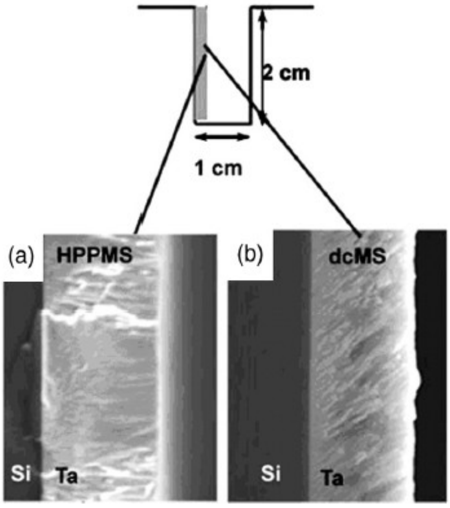

Figure 2.12 – Tantalum thin film growth on silicon substrate deposited by a) HPPMS and b) DCMS on a complex-shaped substrate [22].

As mentioned earlier, heteroepitaxy refers to the growth of a crystalline layer of one material on the surface of a crystalline substrate made of a different material. Three different heteroepitaxial growth modes are reported in the literature: Frank–van der Merwe (layer by layer), Volmer–Weber, and the Stranski–Krastanov [25, 26]. Figure 2.13. schematically illustrates these three heteroepitaxial growth modes. The Stranski-Krastanov configuration is described as a thin layer deposited followed by additional material forming tridimensional islands (clusters) on the top. The clusters form directly on the surface of the substrate (Volmer-Weber mode) or they can grow on the surface of the previous deposited thin and uniform layer (Stranski-Krastanov). One of the factors that influences the formation of tridimensional islands during crystal growth is the strain energy. The films usually grow following the Frank–van der Merwe (layer by layer configuration), until reaching a critical thickness value in which tridimensional clusters start to form because of the energetically favorable scenario started by the strain induced by substrate-film misfit, and the island growing is a mechanism to reduce that strain energy [26, 27].

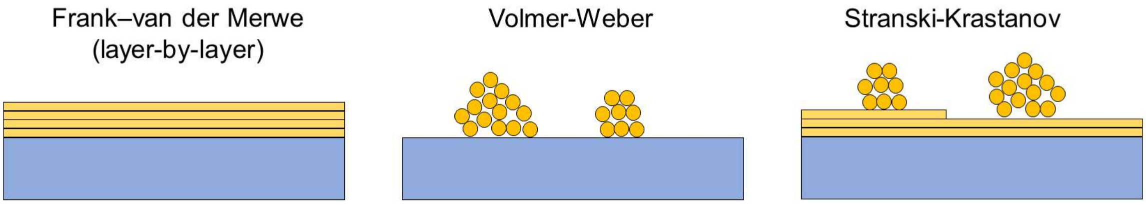

Figure 2.13 – Illustration of the three possible thin film growth modes.
Font: author.

2.3 Inverse Hall-Petch behavior in nanocrystalline materials

A polycrystalline material is considered nanocrystalline whenever it presents a grain size up to 100 nm [28]. A noticeable difference in nanocrystalline materials is the superior fraction per volume of grain boundaries within, where a higher concentration of atoms is located. When the atoms are perfectly ordered at crystalline domains, a lower energy state is found in those areas. On the other hand, there are regions of disorder and higher energy with structures out or far from equilibrium state. These are areas in which mismatch can produce deformation that can promote grain growth, for example, due to the fact that they act as the driving force for growing [28].

Superior mechanical properties are expected to be obtained from nanocrystalline materials as compare with microcrystalline ones, but in many cases, inconsistencies can be found between those materials, leading to strong differences in the mechanical behavior. Generally, the relationship between grain size and strengthening is governed by the Hall-Petch law, which describes how the grain size affects the yield strength and hardness of a material. i.e. It highlights that the yield stress increases with the inverse of the square root of the grain size of a polycrystalline material, in other words, increases its strength states. The Hall-Petch equation is [29]:

$$\sigma_y = \sigma_0 + kd^{-1/2} \qquad \textit{eq. (1)}$$

Where:

σ_y is the yield strength of the material

σ_0 is the friction stress (intrinsic strength of the material, independent of grain size)

k is the Hall-Petch constant (a material-specific coefficient related to grain boundary strengthening), generally between 2.5 and 3.5

d is the average grain size

Nonetheless, several experimental results reported in the literature show that the Hall–Petch relationship, which is perfectly functional at large grain sizes, cannot be extrapolated to grain sizes smaller than 1 μm Meyers and coworkers [30] reviewed the mechanical properties of nanocrystalline materials, emphasizing on the fundamental physical mechanisms, such as the inverse Hall-Petch behavior and the effects of porosity, the difference between tensile and compressive strength, among others aspects. They plotted the Hall–Petch trends ($d^{-1/2}$ Vs. yield strength) of four different metals: Cu, Fe, Ni, and Ti. In figure 2.14 the plots for Ti and Fe are shown, and it can be noticed that the grain sizes go from micrometer to nanometer. On the nanocrystalline range the Hall–Petch curve exhibited a deviation from the regular trend, a decrease in the slope for smaller grain sizes. It is important to point out the behavior of Ti for a d range between 0.05 and 0.12 $nm^{-1/2}$, the yield strength oscillated (increased and decreased) [30].

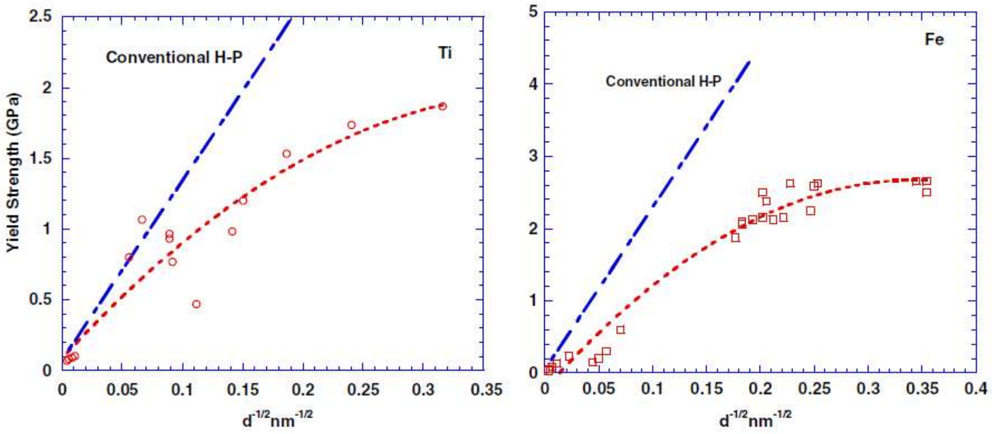

Figure 2.14 – Hall-Petch response observed in Ti and Fe related to the yield strength behavior [30].

A reduction in hardness with decreasing in grain size (ranging between 15 to 5 nm) was observed in Cu and Pd [31]. A similar behavior was reported by Lu and coworkers [32]. They synthesized Ni-P nanocrystalline alloys with average grain size from 9 to 120 nm. The chart of $d^{-1/2}$ Vs. hardness is presented in Figure 2.15.

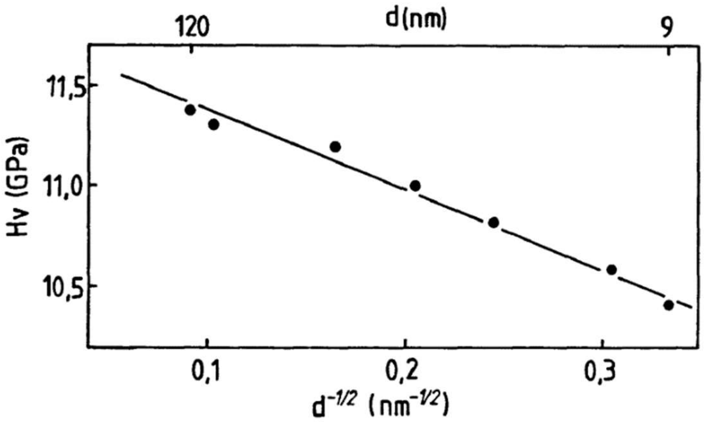

Figure 2.15 – Hall-Petch response observed for Ti and Fe related to yield strength behavior [30].

Yadav and colleagues [33], in their two-phase model for inverse Hall–Petch effect in nanocrystalline thin film, proposed two methods to attempt to better understand the mechanical behavior of nanocrystalline thin films, i.e. the inverse Hall-Petch effect [33]. With a computational method, they simulated the strength of a nanocrystalline aluminum thin film using molecular dynamics. In their experimental results of elastic modulus and strength, they observed that the values are approximately 6 times smaller than the results obtained using the model, probably due to the presence of porosity in the real sample. In the simulation, the elastic modulus for a grain size of 40 nm (without porosity) was 67 GPa, but, with 50% grain-boundary porosity and 20% intra-granular porosity, it resulted in 30 GPa. The ultimate tensile strength was 3 GPa (without porosity) and 1.4 GPa for samples and with porosity. The breakdown of the Hall-Petch relationship in nanocrystalline BCC-type Mo alloys, as well as the hardness and deformation behavior were studied by Duan [34]. Samples with grain sizes from

120 to 4 nm were used. The break down was observed to occurred between 11 and 4 nm [34].

2.4 The Concepts of Biocompatibility and Biomaterials

Biomaterial and biocompatibility are terms understood intuitively, but what does biocompatibility really mean and what exactly is a biomaterial? A first approach to biocompatibility refers to a condition that must be met by a biomaterial and has to do directly with the host tissue response and its wound-healing process, in other words, not to cause any adverse reaction on the host [35]. This response depends on the kind of tissue where the biomaterial is implanted, thus biocompatibility is far from being an invariant property of the biomaterials [32, 35, 36]. The selected biomaterial needs to be tested to determine if it fulfills the criteria to be declared the biocompatibility. A formal definition of biocompatibility goes: “Is the ability of a material to perform with an appropriate host response in a specific application [2, 35].

In the case of biomaterials, the term is automatically associated with the health field. A biomaterial is used to manufacture medical devices for therapeutic purposes, diagnosis, otherwise employed as replacement of a body tissue or assist in a body function (permanently or not). The term ‘biomaterial’ started to being used in the 1960’s and, as well as biocompatibility, the most accepted and formal definitions are as follows: “[biomaterial is] any substance (other than a drug) or combination of substances, synthetic or natural in origin, which can be used for any period of time, as a whole or as a part of a system which treats, augments, or replaces any tissue, organ or function of the body.” or “a non-viable substance used in a medical device, intended to interact with biological systems.” [35, 36] Currently, the scope of biomaterials is going beyond the traditional uses and we can find them now in applications such as smart delivery systems for drugs, manufacture of synthetic tissues (engineered tissues e.g. a 3D printed ear), hybrid organs, and others [32, 36, 37]. Undoubtedly biomaterials have been conceived to improve the individual’s life quality and are a multi-disciplinary research field ever-expanding and continuously on development.

Metals (pure or alloyed), ceramics, polymers, and combinations of them are employed as biomaterials. Due to the fact that the implantable material will be directly in contact with tissues, organs, and the fluids in the body, it is necessary to assess its biocompatibility. To do so, a prerequisite is the characterization in vitro, carried out on raw material (e.g. evaluation of physical, chemical, and mechanical properties, among others.) [36]. Once the material passes these previous tests, it can be evaluated for biocompatibility, which is assessed under specific conditions simulating the exposure environment and the duration. Well-established controlled protocols and standards contain the criteria for evaluation, which may vary depending on the type of the host tissue. The methods for testing biocompatibility can be classified as *in vitro*, animal test experiments (nonfunctional, *ex vivo* and functional tests) and *in vivo*. Some tests carried out *in vitro* and *in vivo* are: chronic toxicity, acute systemic toxicity, reproductive toxicity, genotoxicity, test of implantation, carcinogenicity, hemocompatibility (interaction with blood), cytotoxicity, degradation of the implanted material, toxicokinetics, immunotoxicity, inflammatory response, irritation and sensitization, etc. [2, 35, 36].

In vitro tests are performed in a laboratory using cells and tissues. The methods permit us to process a larger quantity of material, reasonably fast and at a lower cost. A drawback of *in vitro* tests is that it evaluates just in a limited way considering the complexity of the physiological milieu. Hemocompatibility is an example of an *in vitro* test and has to do with the blood cells interacting with the implant. In this test, it is evaluated the formation of thrombus on the surface, possible damage on erythrocytes, etc [36].

Tests in animals (*in vivo*) contribute to determine the tissue-biomaterial viability, but it is not a test conclusive enough test to prove the biocompatibility in the human body due to post implantation, foreign body reactions may occur, although these cases are scarce. The biomaterial implantation causes surgical trauma and consequently a wound healing process starts, passing through stages such as: injury, coagulation, inflammation, and repair and modeling. Figure 2.16 presents the sequence of the three possible vias of the wound-healing process in the body, only one of them conducts to the implant integration to the surrounding tissue [35, 36].

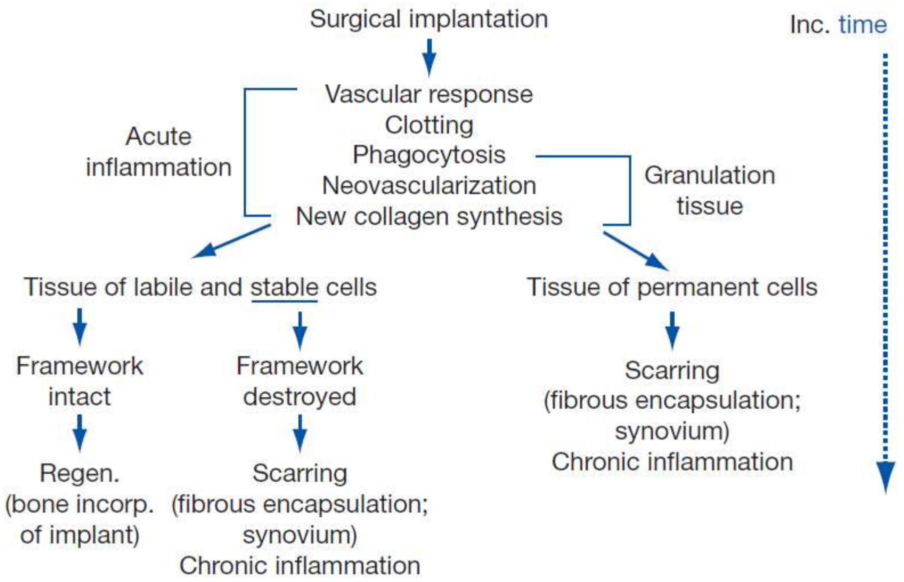

Figure 2.16 – The three possible routes of physiological sequence of wound healing [35].

Vascularized tissues are usually the type where implants are placed, as a consequence a vascular response is expected, basically the formation of edema and fibrin clots (through them cells can migrate). The process continues with the phagocytosis of cellular and extracellular debris, followed by the formation of new blood vessels, then fibroblasts enter fibrin clots. Fibroblast can compete with the other cells covering the implant with fibrous tissue, additionally the presence of macrophages on the surface, so this scenario may result in a fibrous encapsulation of the implant. On the other hand, satisfactory healing implies the covering of the "dead surface" with well-added desired cells e.g. osteoblasts expected in implants in contact with bone, and less or no collagen encapsulation [2]. A successful implantation implies no fibrous tissue between the implant and the tissue and comprises the following stages (Figure 2.17): 1) implant interaction with physiological fluid (i.e. water and ions), 2) protein adsorption forming a protein film, 3) neutrophils and macrophages interrogate the implant (only the protein film); the macrophages activity lead to the formation of foreign body giant cells. Finally, 4) cytokines (a type of bone morphogenetic protein) are released by macrophages that improve the differentiation of the osteoprogenitor cells on the implant surface to make bone [2, 38, 39].

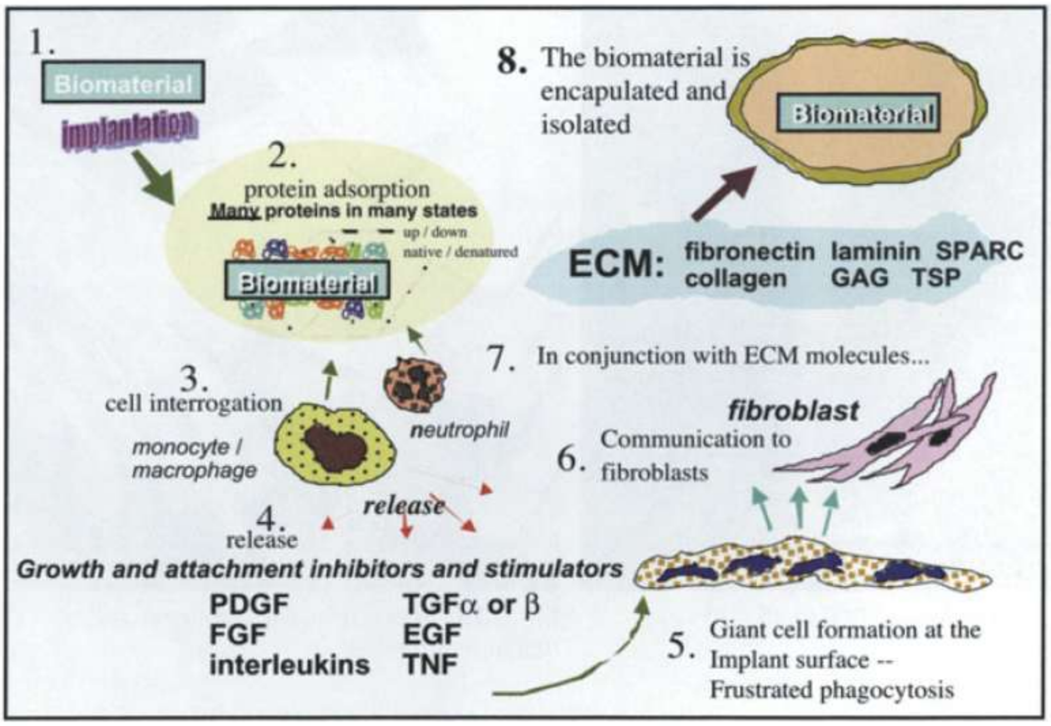

Figure 2.17 – The stages of wound-healing process showing the protein absorption [2].

2.5 Metals in biomedical applications

The materials for biomedical applications, especially implantable materials, must exhibit a set of properties that make them safe and reliable to be used in the human body. Although just a limited number of metals has demonstrated to be safe for long term implantation, for decades they have been preferred among many other types of materials due to the combinations of properties, such as high corrosion resistance and superior mechanical properties [35]. The most common implantable metals can be divided into four groups: 1) stainless steels, 2) cobalt-based alloys, 3) titanium-based alloys, and 4) other special grade alloys, i.e: platinum alloys, gold alloys, tantalum, zirconium and Ni-

Ti, known as NITINOL [39]. In table 2.3 some of these metals are listed and their most common applications as biomaterials.

Table 2.3 – The most common implantable metals and their applications [35].

Metallic Alloy	Reason for medical use	Application
Stainless Steels	Fatigue strength, corrosion resistance	Screws for fracture fixation, hip stems, cables, joint bearings
Titanium alloys	fatigue strength, corrosion resistance, shape memory, highly promotes osteointegration	Joint replacement, dental implants, spinal disc replacement, spinal fusion implants, fracture fixation.
Zirconium	wear resistance of ZrO	Joint replacement
Cobalt	Fatigue strength, corrosion and wear resistance	Joint replacement, stents, pacemaker conductor wires, spinal disc replacement

The austenitic stainless steels (SS) are the most frequently used alloys as biomaterials due to their low cost, the principal advantage in contrast with the other alloys. The addition of chromium in the SS leads to the formation of a passive film on the surface consisting of Cr_2O_3, but sometimes it may contain other oxide species that interact with the tissue in an undesirable way [35]. On the other hand, the human body fluid is detrimental for the passive layer, since it is not resistant to the chlorine ions attack, that reduces the duration of the implant in the body. The two commonly used SS's are AISI 316 L (with low nickel content) and AISI 304. They must be highly resistant to localized corrosion (i.e pitting), but under some conditions the corrosive process occurs, and significant quantities of corrosion products are released to the milieu [36, 37, 40]. The SS's offer the possibility to obtain a wide range of mechanical properties, however a drawback of SS is its higher elastic modulus (200-165 GPa) [41], in contrast with human bones (10 – 30 GPa). Figure 2.18 Illustrates a chart of various elastic moduli of different biomaterials in comparison with human bone [2, 41, 42]. The notorious difference between the Young's moduli of the SS and bone can cause a deleterious effect known as stress shielding that limits the bone formation and leads to the implant failure [2]. As can be observed in Figure 2.18, the cobalt alloys may produce the same effect as SS, despite they present excellent mechanical properties. The most suitable alloys for diminishing the stress shielding are the Ti-based alloys. The SS properties can be improved by depositing ceramic films to enhance wear resistance and the use of other metals for enhancing corrosion resistance.

Fellah *et al*. [43] studied the tribological properties of a 316L femoral stem, carrying out two different wear tests, the first one using tribometers ball on disc and sphere on plane, and the other one with a pin type tribometer. The results for wear and friction on both tests were the same, and they suggested the implementation of surface treatment and the coating deposition to improve the wear resistance.

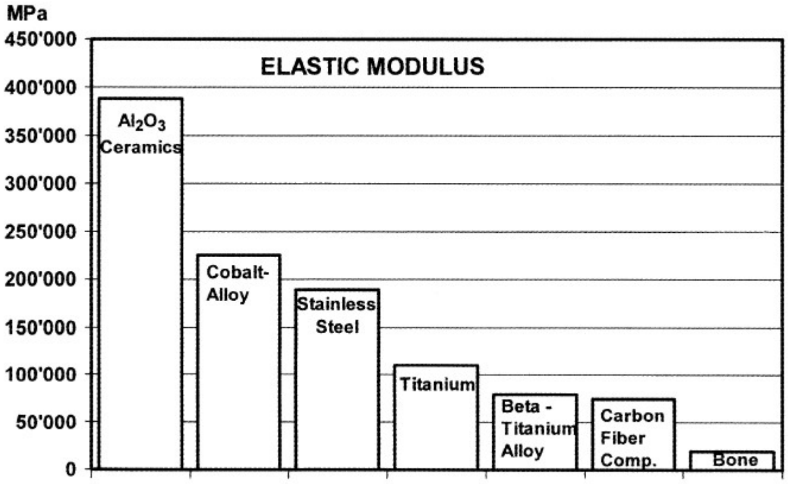

Figure 2.18 – Comparative chart of elastic modulus of various types of biomaterials with human bone [2].

2.5.1 Titanium and titanium-based alloys as biomaterials

Titanium is a transition metal, the ninth most abundant element on earth´s crust [44]. The most important titanium ores are ilmenite ($FeTiO_3$), rutile (TiO_2), and leucoxene (consisting of rutile or anatase, polymorphs of TiO_2) an alteration product of perovskite, ilmenite or sphene. The countries with the main ilmenite and rutile deposits are: Australia, South Africa, Canada, India, Mozambique, China, Vietnam, Ukraine, Norway, Greenland, United States, and Russia.

Titanium sponge, main raw material, is mainly produced in Russia, Kazakhstan, Japan, United States, United kingdom, and China [45].

Titanium presents a strong tendency to react with oxygen and nitrogen and they are always present as interstitial impurities in high or low concentrations. This reactive condition makes the extractive metallurgy process very difficult, and as consequence a controlled atmosphere and vacuum are necessary. Titanium sponge is produced by Kroll process, consisting on the titanium tetrachloride ($TiCl_4$) reduction by magnesium in inert gas atmosphere; the result is a porous and sponge-like product, known as the titanium sponge [44, 45].

Compared with high grade steels (e.g. AISI 316 L), it shows exceptional mechanical properties exhibiting high strength-to-density ratio (specific strength), which is ~78 kNm/kg for CP-Ti ($Ti_{density}$= 4.51 g/cm³), vs. iron's that is ~25 kNm/kg ($Fe_{density}$ =7.8 g/cm³). Titanium presents high reactivity and forms an oxide layer of about 4 nm of thickness, this is a non-toxic passive layer that confers its superior corrosion resistance, which is an important requisite for long-term biomedical implants. Due to its excellent biocompatibility characteristics, commercially pure (CP) and some titanium alloys (i.e. Ti6Al4V) are preferentially selected for surgical implantation above other options. The main drawback of titanium is the high price (4800 USD per metric ton, against 2500 USD per metric ton for 316 L and 304) [46,47].

Titanium crystallizes in two allotropic forms. Above 882°C (the average transus or β-transus temperature, T_β) it presents the body-centered cubic (bcc) structure, the β phase, and under T_β, it undergoes the transformation to the α phase with hexagonal close packed (hcp) crystal structure. The crystal structures of titanium are illustrated in Figure 2.19, indicating the lattice parameters and the most densely packed planes: basal (0002), pyramidal $(10\bar{1}\bar{1})$ and prismatric $(10\bar{1}0)$, and the (110) in the bcc [45,48].

Different alloying elements are added to stabilize one or another phase, these are known as alpha and beta stabilizers. The principal α stabilizers (α_s) elements are aluminum, carbon, oxygen and nitrogen and a secondary group of elements with very low solubility: boron, gallium, germanium, and rare earths, hence they are rarely used as alloying element [45]. The CP titanium within the α phase is called “unalloyed”, but in truth it presents different grades, depending on the strength level obtained by different oxygen concentrations. β stabilizers (β_s) elements are niobium, molybdenum, iron, chromium, and vanadium. Aluminum is the alloying element for excellence, due to its high solubility in the α and β phases, and it also contributes to increase the transition temperature like no other common element. Aluminum is also the main α_s element [44, 45].

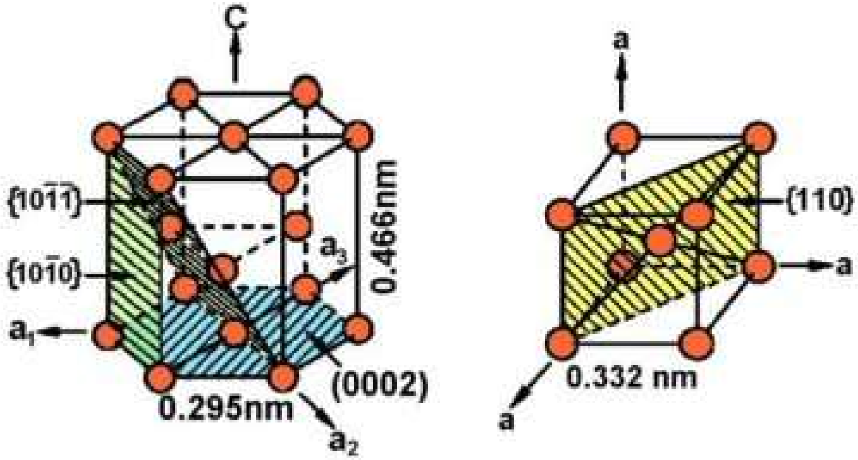

Figure 2.19 – hcp crystal structure of α-Ti (left) and bcc crystal structure of β-Ti (right) [48].

The titanium alloys can be classified as: α, near-α (super-α), α-β, and β [44, 45]. According to the type of alloying elements, their influence in the β-transus temperature and their grade of solubility, different types of phase diagram are obtained, the β stabilizers can be sub-divided into β-isomorphous and β-eutectoid; the diagrams are depicted in Figure 2.20.

When appropriate concentrations of the β-isomorphous elements (vanadium, molibdenum, and niobium) are added, the β phase is stabilzed at room temperature. In the case of the β-eutectoid, the most frequently used alloying elements are iron, chromium, and silicon. The other elements such as nickel, copper, manganese, palladium tungsten, and bismut are used only in very little number of special alloys.

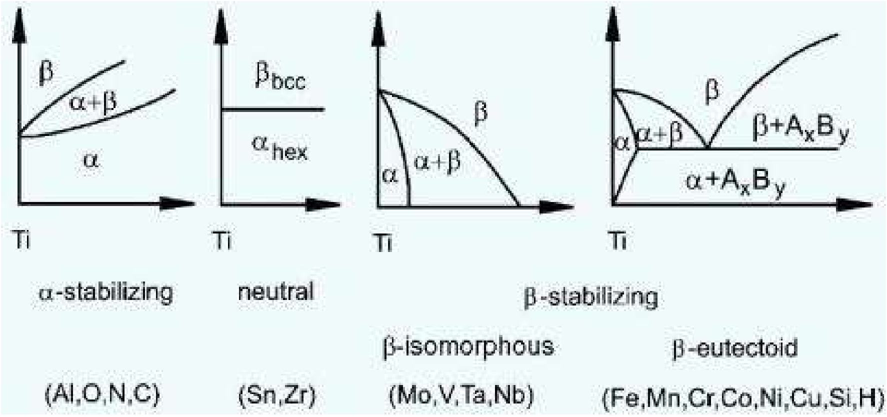

Figure 2.20 – The different types of titanium phase diagram according to the alloying elements [45, 48].

When appropriate concentrations of the β-isomorphous elements (vanadium, molibdenum, niobium) are added, the β-phase is stabilzed at room temperature.

In the case of the beta-eutectoid, the most frequently used alloying elements are iron, chromium and silicon. The other elements such as nickel, copper, manganese, palladium, tungsten, and bismut are used only in very little number of special alloys [49].

A β-alloy contents enough amounts of beta-stabilizers to completely retain the beta-phase after submitted to a quenching process from above the β-transus temperature, avoiding the formation of martensite. It exists a critical minimum value of the β-stabilizer element (β_c) that must be exceeded in order to reach the β-phase formation. However, to consider the β-alloy completely stable, the concentrations have to remain beyond the β-stabilizer value (β_s), as can be observed in Figure 2.21 [49].

A parameter that can be used to assess the overall stability of the β-phase in a β alloy is the so-called molybdenum equivalent (Mo_{eq}), and it can be calculated with equation (2.) [50] as follows:

$$Mo_{eq} = 1.0(Mo) + 0.67(V) + 0.44(W) + 0.28(Nb) + 0.22(Ta) + 2.9(Fe) + 1.16(Cr) - 1.0(Al) \qquad Eq.(2)$$

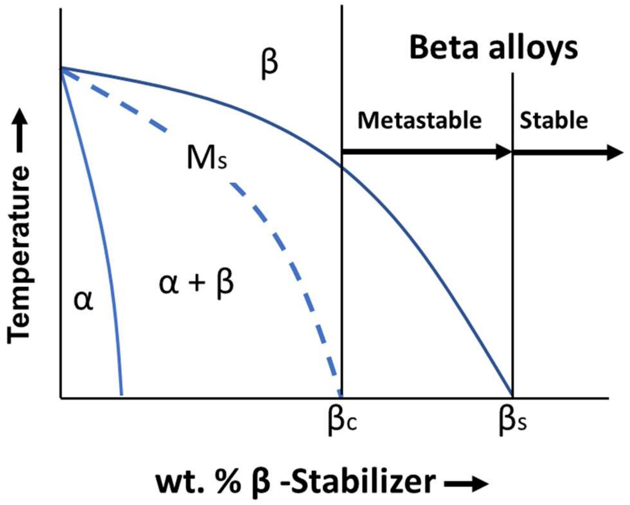

Figure 2.21 – The β stabilization diagram [49].

Where, the coefficient before each weight percent (wt.%) value of the alloying element indicates the ratio between the Mo baseline (i.e., 10.0) and the critical minimum value of the β-stabilizer element (β_c). Table 2.4 presents the types of β_s elements with their respective calculated values for β_c, which indicates the approximate weight percent needed to only retain β-phase when submitted to quenching. Aluminum was added as negative in order to represent its opposite tendency to stabilize the β-phase [49].

Table 2.4 – The β-stabilizer elements types [49].

βs	**βc (wt.%)**	**Type**
V	15.0	Isomorphous
W	22.5	
Nb	36.0	
Ta	45.0	
Fe	3.5	Eutectoid
Cr	6.5	
Cu	13.0	
Ni	9.0	
Co	7.0	
Mn	6.5	
Mo	10.0	

The phase transformation from β to α in pure titanium may occur in two different ways: the martensitic transformation or by diffusional means.

The martensitic transformation is a non-diffusional or displacive transformation produced by the cooperative movement of the atoms (military type) on the order of the interatomic distances or less, such movement can be originated by a homogeneous distortion, *by shuffling of lattice planes, by static displacement waves (periodic displacements of atoms from their original positions) or by a combination of these*. In an athermal process, the introduction of displacement waves in a parent lattice is produced by coordinated movements of the atoms, this will lead to the structural transition [51].

The martensite grains are constituted by platelets or disk-shaped particles. Each platelet presents shape changes which indicate strain during the transformation. The shape changes are caused by the action of shear parallel to the habit plane, with uniaxial expansion normal to the habit plane.

The transformation from bcc to hcp occurs as result of shear strain, and the β-phase can transform into twelve different α (hcp) crystal structures with different orientations depending on the orientation of the parent crystal structure [44, 52]. Two different types of martensite can result from the transformation: hexagonal (α'), and orthorhombic (α'') as a secondary phase.

Another secondary phase known as ω may also occur in Ti-X systems (where X represents a β_s element). The ω and α'' are usually known as the intermetallic ordered coherent Ti_3Al. The ω phase is undesirable since it produces embrittlement, and α'' is undesirable in some cases where stress corrosion cracking must be strictly avoided [44, 45, 52].

Two types of ω, isothermal and athermal, can be form from β-phase under specific conditions (e.g. a range of composition with specific electron-to-atom e/a ratios). At certain temperatures which may occur the formation of ω and α'', athermal ω forms into a tight range of composition (e/a), slightly above of the martensitic start, during rapid quenching processes. On the other hand, ω may appear as a precipitate during β decomposition in an even wider range of compositions [50]. Hume-Rothery [53, 54], pointed out the influence of electron concentration in the formation of intermediate phases in transition metals (e.g. σ-phase in chromium alloys), and showed the relation between the formation of σ-phase and the e/a ratio, as illustrated in Figure 2.22. On the same line, Collins and colleagues [55] studied the dependence of ω-phase occurrence on e/a ratio, in transition metals, as seen in Figure 2.23.

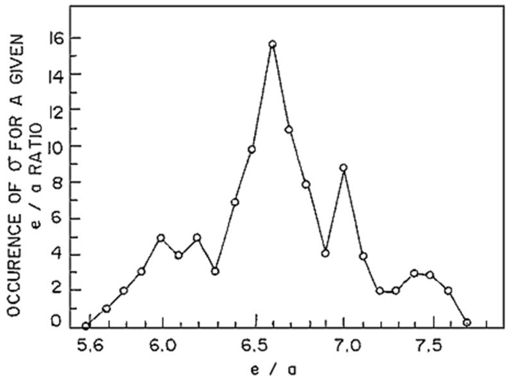

Figure 2.22 – Composition range of σ phase in transition metal alloy system as a function of e/a ratio, after Hume-Rothery [54].

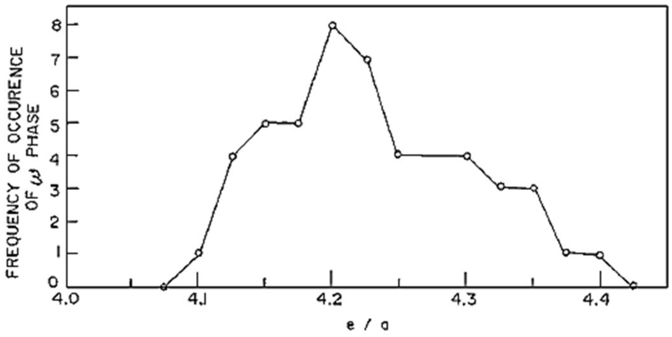

Figure 2.23 – Dependence of ω phase occurrence on e/a ratio, in transition metals [55].

When an α-β or β-alloys are highly β-stabilized, at normal pressures (i.e. P_{atm}), ω appears as metastable, and the composition range where this occurs is characteristic of the specific system. The athermal transformation of ω is similar to martensite, this means diffusionless. The athermal ω precipitates can be formed from rapid cooling during quenching and are extremely fine (less than 5 nm) and it is difficult to identify a well-defined shape of it, and it appears that it is generally aligned in the $<111>_\beta$ directions. On the other hand, isothermal ω precipitates have two types of shapes: ellipsoidal or cubic. Both non-equilibrium phases, ω and martensite form by the displacive non-thermal transformations by a homogeneous distortion [50].

The commercial Ti-based alloys for biomedical purposes (some of them with shape memory effect) belong to the β (e.g. Ti12Mo6Zr2Fe) and α + β groups (e.g. Ti6Al4 and Ti6Al7Nb). These alloys are Ni-free, which means that they have higher biocompatibility owing to the lack of any allergic effects in the human body [56, 57].

The study of titanium biocompatibility is mainly focused in its corrosion resistance and bio inertness, the interaction with cells and proteins, surface modification (textures or chemical), and the wound-healing process (e.g. the osteointegration). Titanium is able to adsorb proteins from the human fluids (i.e. albumin, laminin V, collagenase, fibronectin, fibrinogen, among many others) and interacts with cells supporting the cell growth and favors differentiation (i.e. when an osteoprogenitor cell migrates to the implant surface and differentiates into osteoblast, a process potentiated by bone morphogenetic proteins such as cytokines and metabologens) [2]. A scheme of this process is depicted in Figure 2.17. It exists a wide variety of studies in the literature about these subjects. The manufacture of non-periodic nanostructures on titanium implant surface, such as nanoleaves, nanotubes, nanoneedles, and nano-scaffolds, improves the osteoblasts activity allowing more proliferation and adhesion, on the other hand it inhibits the thriving of fibrous tissue at the tissue/implant interface. The leave-life nanostructure showed the most promising result among the other types demonstrating the best performance [38].

The Ti6Al4V alloy presents an exceptional combination of mechanical properties, corrosion resistance, and biocompatibility, in contrast with the other metals used for biomedical applications. However, some of the mechanical properties can be disadvantageous in some cases, for example, it exhibits high yield stress (795 MPa), fatigue strength, but it may decline due to notch sensitivity; high elastic modulus, but it may cause stress shielding in joint implantation [2]. Nevertheless, the Ti6Al4V (an α + β alloy), is by far the most widely used Ti-based alloy as biomaterial, and it was one of the first implantable components, however it presents clear disadvantages, such as its low wear resistance, that can produce debris under extreme wear conditions, compromising the life spam of the implant. The aluminum and vanadium contents are another drawback, since these elements can cause adverse reactions in the human body due to the liberation of ions in the implant vicinity increasing the toxicity risk [2, 35]. Due to the disadvantages found in the α + β alloys for implantation, in many cases β-alloys result in a better option for this purpose. Β-alloys present less notch sensitivity compared to the α + β; they are easier to deform at low temperatures due to the activation of more slip systems that make them cold-work strengthened, and present super elasticity due to the stress-induced martensitic transformation [35, 58].

Another Ti-based alloy is the so-called Gummetal® which is a relatively recent and innovative titanium alloy (2003) that exhibits unique properties. It was developed by Saito and coworkers [59] at Toyota Central R&D Labs in Japan, and it has been recognized for its remarkable combination of properties, which are not typically found together in conventional materials. Gummetal is primarily composed of Ti, Nb, Ta, Zr, and O, and the specific composition can vary according to specific desired properties [59, 60]. Gummetal exhibits super elastic behavior, low elastic modulus, high fatigue resistance (due to its unique microstructure, which can dissipate energy and prevent the initiation and propagation of cracks), high strength, high ductility, low Poisson's ratio, excellent corrosion resistance, and superior biocompatibility. In Figure 2.24 are compared the tensile strength vs. elastic modulus trend for various alloys used as biomaterials, with Gummetal. It is widely used for orthodontic wires [61], among many other uses. Gummetal deforms primarily through mechanisms that do not involve the movement of dislocations, and the deformation occurs through atomic-scale shifts and lattice rotations [59].

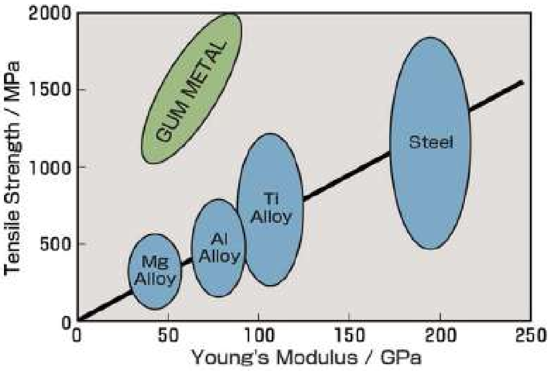

Figure 2.24 – The tensile strength vs. elastic modulus trend for various alloys used as biomaterials compared with Gummetal® [61].

Table 2.5 – Characteristics of some biocompatible metal alloys employed for biomedical applications.

Alloy	**Elements**	**E (GPa)**	**σ_y (MPa)**
12Au-Ag-Pd	Au, Ag, Pd	> 250	900
AISI 316	Fe, Cr, Ni, Mo	200	860
ASTM F562	Co, Cr, Ni, Mo	170	1000
CP Titanium	Ti	102	270
Nitinol	Ti, Ni	105	700
ASTM F136 (Ti6Al4V)	Ti, Al, V	85	860
GUMMETAL	Ti, Nb, Ta, Zr	45	1100

2.5.2 The Ti-Nb and Ti-Nb-Mo systems

Titanium, niobium, and their alloys have been widely used in diverse applications such as automotive, aeronautics, nuclear, steel industry, superalloys, and biomedical applications. Due to their superior properties and their proved biocompatibility (they are non-toxic elements), Ti-based alloys are preferred instead of stainless steels, Co and Ni-based alloys in many cases in spite of their higher cost. As can be noticed, Ti-based alloys employed in biomedical applications usually contain chemically inert elements as such as zirconium, niobium, molybdenum, and magnesium [39]. Some of the general features of these elements are listed in Table 2.6.

Niobium (Nb) and molybdenum (Mo) are both transition metals and belong to a group known as refractory metals [62], due to their high melting point (2477°C and 2623°C respectively), and both of them exhibit high corrosion resistance. Niobium is a strategic element in the composition of many special alloys, and over the last 60 years its application has grown considerably. Brazil holds the largest reserve and production of niobium ore (*pyrochlore*) in the world, accounting for about 98%. The mines are located in Araxa (MG), exploited by the CBMM company [63, 64].

The majority of the supply sources of Mo (as co-product or as a by-product) comes from copper mining (containing less than 0.1% of Mo in its ore), and only about a quarter of the Mo exploitation comes from primary mining. The most abundant ore is the molybdenite (MoS_2). About 83% of total reserves in the world are localized in Chile, United States, and China [65].

Nb and Mo, as well as Ti, exhibit high corrosion resistance, due to the formation of an adherent passive oxide layer on the surface. However, Mo can undergo fast oxidation at high temperatures (about 600°C) and Nb exhibits high corrosion resistance in the majority of aqueous media at room temperature [2, 62, 65]. Elements like Nb and Mo contribute to grain refinement, carbide formation, and increased resistance to dislocation movement, all of which enhance stiffness and increase the elastic modulus.

Table 2.6 – General features of titanium, niobium, and molybdenum [41, 62, 66].

Element	**Z**	**A (g/mol)**	**AR (Å)**	χ	**ρ (g/cm³)**	**Mp (K)**	**Bp (K)**	**E (GPa)**	**G (GPa)**	**HV (GPa)**
Ti $hcp \xrightarrow{882℃} bcc$	22	47.87	1.47	1.5	4.51	1941	3560	116	44	3.42
Nb (bcc)	41	92.91	1.46	1.6	8.58	2750	5017	105	38	1.58
Mo (bcc)	42	95.96	1.39	2.16	10.22	2896	4912	329	126	2.74

Ti-Nb and Ti-Nb-Mo systems belong to the β-alloys group and present better biomedical characteristics when compared to the Ti6Al4V alloy, since they are composed of inert elements. β-alloys have zero or low content of α-stabilizers, in the case of Nb and Mo, they are strong β-stabilizers with high solubility in titanium, as can be corroborate in the equilibrium phase diagrams of Ti-Nb (isomorphous type) and Ti-Mo (eutectoid type) (Figures 2.25 and 2.26, respectively).

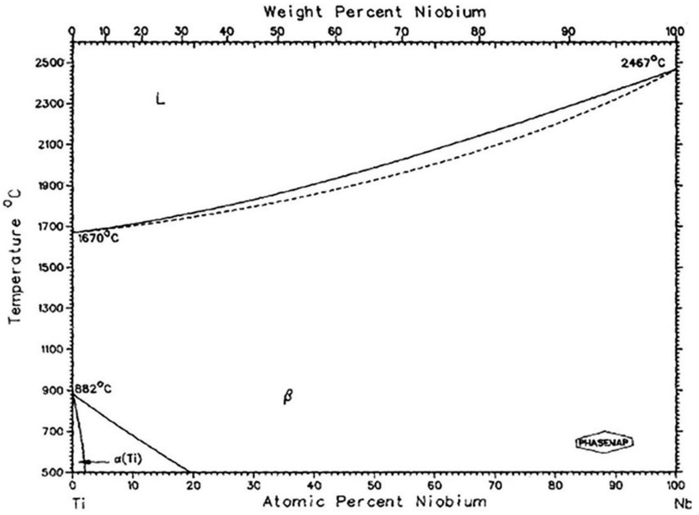

Figure 2.25 – The Ti-Nb equilibrium phase diagram [44].

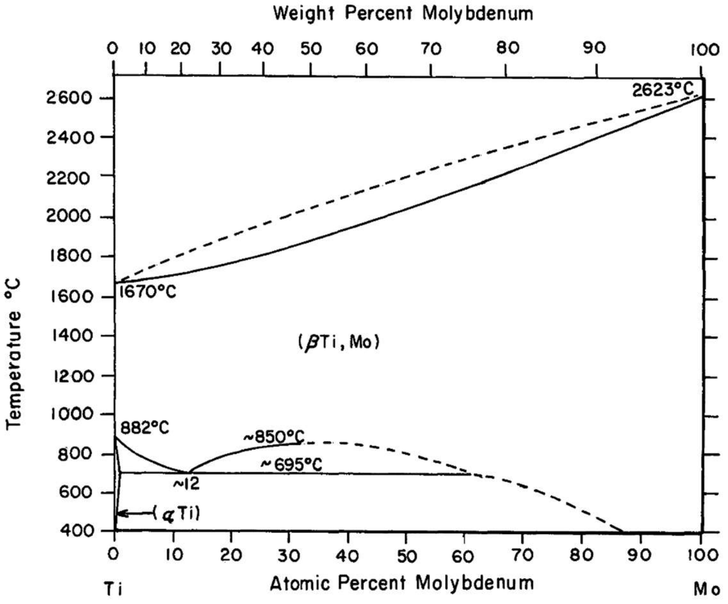

Figure 2.26 – The Ti-Mo equilibrium phase diagram [44].

The mechanical properties and corrosion resistance of nine as-cast Ti-Nb_x (x=5, 10, 15, 17.5, 20, 22.5, 25, 27.5, 30, 35 wt.%) binary alloys were studied by Lee and colleagues [67]. The samples were prepared by arc-melting casting process. It was observed that the microstructure evolution was highly influenced by the increasing in Nb content (a similar behavior was observed in Ni-Nb binary alloys as well [68]). The alloy containing 15 wt.% or less of Nb presented the α' phase with acicular morphology, and with the increasing content in a range of 17.5 to 25 wt.% of Nb, it occurred a transformation into the orthorhombic α''. Higher contents of Nb caused a transformation into the β metastable for contents from 27.5 wt.% Nb and more. Between 27.5 and 30wt.%, the ω phase was observed with coarser grains of β-phase. Fluctuations in the microhardness values were found. The sample with 27.5 wt.% Nb presented the highest hardness value, explained by the presence of the ω phase.

Achache *et al.* [58] investigated binary alloys $Ti_{1-x}Nb_x$ (x=3, 5, 9, 17, 22, 29, 34 at.%) coatings, deposited on glass substrate by means of the DC magnetron co-sputtering process with the aim to investigate de dependence of the β phase stabilization and the mechanical properties as function of the chemical composition. The coatings grew with thickness in the range between 2.41 to 3 µm. Fractions of β phase started to appear in concentrations above 17 at.% Nb and single β phase was observed above 30 at.% Nb. A competition occurred between the strain and surface energies that made the preferential orientation of β phase change from {110} to {111} at high Nb concentrations, and this was explained by the anisotropy caused by collision effect. The single β phase coatings exhibited high depth recovery that was attributed to the superelastic effect. The elastic modulus decreased as a function of the Nb content until it reached the lower values for Nb concentrations between 20 to 25 at.%. The same trend was followed by the hardness values, above 25 at.% Nb these values were observed to increase again, this could be explained by the presence of the α phase.

Gonzalez *et al.* [69] characterized the microstructure and morphology of Ti-Nb_x thin films having four different compositions (x=15, 20, 30, 40 at.%), deposited on AISI 316 L substrate by DCMS process, and they were characterized as function of the deposition parameters. Crystallographic texture was modified with the Nb addition due to the different growth modes. Increasing grain sizes were observed with the Nb content, and for 30 at.% Nb, the film exhibited cone-like morphologies, characteristic of the T zone in the SZD. The maximum thickness of the thin films was 800 µm. Nanostructured and partially oxidized surfaces (TiO_2 and Nb_2O_5) were obtained, and it was observed a Ti enrichment on the surface.

Photiou *et al.* [70] deposited Ti-Nb_x (x=15, 20, 32, 38, 44, 53, 63, 73 at.%) thin films on silicon surface using magnetron co-sputtering with the aim of studying the mechanical properties and microstructure. Stabilization of the β-phase was achieved at 20 at.% Nb, indicating that the magnetron sputtering process improved the stabilization of the β-phase at lower temperatures due to the possibility of controlling kinetic and impact energies. The 15 at.%Nb alloy had the lowest Young's modulus (68-85 GPa), and an explanation for this was the volume fraction of the coexisting phases and the porosity found in this thin film. Above 20 at.% Nb, the Young's modulus values increased due to the precipitation of the ω phase (E_ω ~ 130 to 200 GPa). The range of the obtained thicknesses were from 590 nm up to 1.35 µm.

Cardoso *et al.* [71] characterized four different chemical compositions of Ti-5Mo-xNb, prepared in arc melting furnace under argon atmosphere. They observed an increasing in β-phase fraction with the increasing in Nb content, as well as a decreasing in hardness, attributed to the increment in β-phase. Cytotoxic tests were carried out, and the alloys were found to be non-toxic for human cells.

Myslyvchenko [72] studied the solidus temperatures and hot hardness for eight compositions of Ti–Nb–Mo alloys produced by arc-melting. They did not observe significant changes in hardness. The XRD patterns for the four samples are presented in Figure 2.27.

Ti-Nb-Mo alloys may also exhibit memory form, as was reported by Al-Zain and colleagues [73]. They investigate the shape memory properties of various TiNbMo biomedical alloys and these four compositions (wt.%) Ti–24Nb–1Mo, Ti-

21Nb-2Mo, Ti18Nb3Mo, and Ti15Nb4Mo, exhibited the most stable superelasticity behavior.

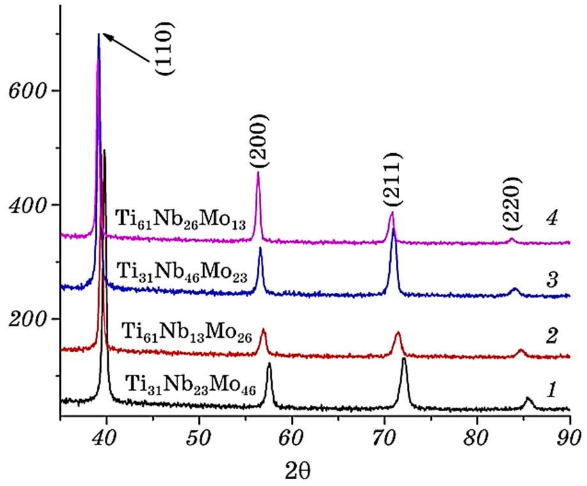

Figure 2.27 – XRD patterns for four as-cast Ti-Nb-Mo β-stable samples [72].

Xu *et al.* [74] studied the microstructure and properties of Ti–10Mo–xNb (x=3, 7, 10) alloys for biomedical application. The alloys were prepared by arc-melting casting. They found that the Young's modulus ranged between 24.7 and 28.4 GPa, and the samples exhibited hardness values between 3.9 and 4.4 GPa. The alloys exhibited advantageous elastic modulus values for biomedical application, also presenting high strength. Li Peiyou and colleagues [75] studied the microstructural and mechanical properties of four as-cast $Ti_{74-x}Mo_xNb_{26}$ (x=0, 2, 4, 6 and 8 at.%) alloys. They found that $Ti_{74}Nb_{26}$ binary alloy was composed of α″ and β-phases, but the$Ti_{74-x}Mo_xNb_{26}$ (x=2, 4, 6 and 8 at.%) ternary alloys were only formed by the β-phase, as can be observed in the diffractograms depicted in the Figures 2.28 They performed nanoindentation tests and measured hardness values that ranged between 2.82 and 3.61 GPa with a fluctuation in these values, but a trend to decrease. They attributed such decreasing to the desapperearance of the α” phase. A similar behavior was observed for the elastic modulus, whose range was between 54.5 and 75.1 GPa. The authors argumented that the reason for this decreasing was the higher concentration of Mo that leaded to instability and also the remaining of the α” phase.

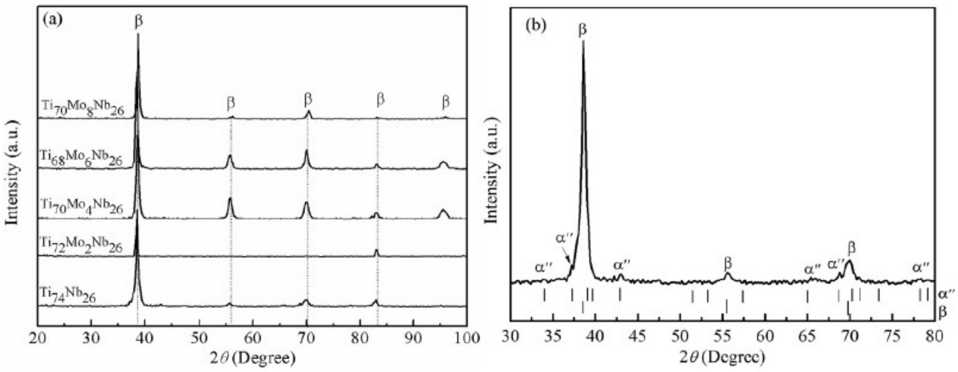

Figure 2.28 – XRD patterns for (a) $Ti_{74-x}Mo_xNb_{26}$ (x = 2, 4, 6 and 8 at.%) and (b) Ti_{74} Nb_{26} [75].

2.5.3 Corrosion resistance for the Ti-Nb-Mo systems

As previously mentioned, it is well known the corrosion resistance of Ti, Nb, and Mo; combinations among them to form β-stable alloys also exhibit an enhanced corrosion resistance characteristic, which is ideal for biomedical applications [42]. Extensive information about this topic can be found in literature. Chelariu *et al.* [76] studied the improved corrosion resistance in saline solution media for four β-metastable Ti-Nb-Mo alloys. To ensure only the formation of the β phase, they fixed the Mo_{eq} value around 12 wt.%. The compositions (wt. %) were as follows: Ti10Mo8Nb, Ti8Mo16Nb, Ti6Mo24Nb, Ti4Mo32Nb, and Ti12Mo for comparison. XRD analysis corroborated that the four samples containing Mo and Nb had only the β phase. The sample without Nb (Ti12Mo) presented very low intensity peaks associated to the ω phase. Potentiodynamic polarization and electrochemical impedance spectroscopy (EIS) were carried out in 0.9 wt% NCl and the results determined that the corrosion and passive current densities decreased with the increasing Nb content, due to the formation of a passive oxide film, and no evidence of any breakdown in the film was observed. The EIS results indicated the formation of a compact oxide layer that exhibited dielectric behavior, and the samples with higher Nb content presented capacitive characteristics. The lowest activity related to electron transfer was observed for two samples: Ti8Nb10Mo and Ti16Nb8Mo.

The corrosion resistance in 3.5 wt.% NaCl solution of Ni-Ti-Nb shape memory sputter-deposited thin films was studied by Kun Li *et al.* [77] by means of open-circuit potential and potentiodynamic polarization tests. The Ni-Ti-Nb alloys exhibited higher open circuit potential, higher corrosion potentials (E_{corr}), and lower corrosion current densities (i_{corr}) when compared with the binary Ni-Ti, indicating a better corrosion resistance. Such behavior was explained by the addition of Nb which improved the passive layer on the film. The results also showed an increment in open circuit potential with the increment of Nb concentration.

The corrosion resistance of two Ti-Mo-Nb aged alloys was investigated by Almeida *et al.* [78] using the potentiodynamic polarization curves in Ringer's solutions media. On the basis of the corrosion current density, the Ti10Mo20Nb ($Ti_{81.8}Mo_{6.1}Nb_{12.0}$) alloy exhibited better corrosion resistance as compared to the Ti12Mo13Nb ($Ti_{85.2}Mo_{7.1}Nb_{7.6}$) alloy and the commercial Ti6Al4V alloy. The result was attributed to the higher Nb content.

The corrosion behavior of β-type Ti-Nb and Ti-Mo surfaces modified by thermochemical treatments was studied [79]. An increasing the repassivation rate of Ti-Nb alloy with respect to CP Ti and Ti-Mo was observed, due to Nb diffusion that formed a stable passive layer.

The electrochemical stability and corrosion resistance of six different Ti-Mo alloys were studied by Oliveira and *et al.* [80]. Concentrations of: 6, 10, 15, and 20 wt.% of Mo were prepared by arc-melting in Ar atmosphere. The XRD patterns revealed the presence of the following phases on the alloys: Ti6Mo (α-type), Ti10Mo (α + β type), Ti15Mo and Ti20Mo (β-type) alloys, reinforcing the fact that Mo concentrations above 10 wt.% stabilizes the β-phase. The electrochemical tests were conducted in Ringer's physiological solution (NaCl 8.61 g L^{-1}, $CaCl_2$ 0.49 g L^{-1}, and KCl 0.30 g L^{-1}). The results of the electrochemical behavior in open-circuit potential (E_{oc}) showed passivation due to the formation of the protective layer. E_{oc} decreased with the increasing in Mo. Impedance values were high and increased with the immersion time of the samples, indicating an improvement in corrosion resistance. Mo addition improved the protection.

Finally, the potentiodynamic polarization test showed the formation of a barrier protective layer. Tomachuk *et al.* [81] Investigated wet corrosion of Mo thin film related to the effect of Ti and Nb addition. The thin films were deposited by magnetron sputtering. The electrochemical impedance spectroscopy (EIS) analysis was conducted in aqueous aerated 0.6 N NaCl solutions at standard room temperature. The results indicated that the Mo-Ti alloy exhibited better protective properties than the Mo-Nb and pure Mo films. Cremasco *et al.* [82] studied the effect of two heat treatments (furnace cooling and water quenching) on the electrochemical corrosion resistance of a Ti–35Nb (wt.%) alloy for medical prostheses. They immersed the samples in a NaCl solution at 0.9% at room temperature and observed a decrease in the corrosion resistance for the samples submitted to water quenching, due to the presence of acicular martensite.

2.6 Residual Stress in Thin Films

Magnetron sputtering involves material ejection from a target onto a substrate. A plasma is generated in the presence of a magnetic field, causing ions to bombard the target, which then releases atoms that travel to and deposit on the substrate [1]. The energy of the incoming atoms, deposition conditions, and substrate temperature play crucial roles in determining the properties of the resulting thin film, including residual stresses [83]. Residual stress in thin films constitutes an important issue on the film's mechanical properties and can significantly influence its performance in various applications. The residual stresses induced during this process can be influenced by several factors, such as the energy of the incoming atoms, the deposition conditions, pressure inside the chamber, bias voltage (negative bias can attract more ions, increasing stress), substrate temperature, among others [84]. A combination of various types of residual stresses can be found on the films, and these include thermal stresses (due to temperatures changes, substrate heating, cooling), internal stresses that may occur because of mobility of atoms on the surface of the growing film (*adatoms mobility*), film growth mode, and atomic peening [85]. The deposition conditions can directly influence the adatoms mobility, hence if the adatoms present low mobility is more likely to result in tensile stress, in the formation of voids or incomplete atomic bonding [86]. High mobility of adatoms promotes denser films that result in compressive residual stresses [87]. The film growth mechanism (e.g., layer-by-layer, island growth), also influences the development of intrinsic stresses, e.g. island growth can lead to tensile stresses as the islands coalesce [87, 88].Similarly, as in a shot peening process, the adatoms impact at high velocity onto the surface of the substrate inducing plastic deformation. The accumulation of many such impacts may generate a uniform layer of compressive stress. In some cases, these compressive stresses help enhance the fatigue strength, reduce the likelihood of stress corrosion cracking, and improve the overall durability of the material [88].

Residual stresses in sputtered thin films can be measured using methods like wafer curvature measurements [84], or by GIXRD that allows the assessment of such residual stresses by analyzing the strain-induced shifts in the diffraction peaks of the film material [86]. Residual stresses lead to lattice strains, which in turn cause shifts in the positions of the diffraction peaks; measuring these peak shifts, the strain in the film can be quantified. The relationship between the strain and stress in the film can be described using elastic constants, such as Young's modulus and Poisson's ratio [86]. The differences in thermal expansion coefficients (thermal mismatch) between the constituent elements (e.g. Ti-Nb-Mo) and the substrate leads to extrinsic residual stresses during cooling after deposition [86, 88].

Growth stress (intrinsic stress) occurs during deposition processes such as sputtering or evaporation. Atoms arrive at the substrate surface, and the film grows layer by layer. The way that the atoms arrange themselves can induce stress due to surface energy minimization, island coalescence during the early stages of growth, and differences in atomic radii of elements. These stresses are often compressive at lower temperatures due to atomic peening, and tensile as the film cools [88]. Volume changes during phase transitions may introduce tensile stresses, and compressive stresses in some oxides [86]. Since Ti-Nb-Mo alloys can exhibit phase transformations (e.g. formation of the β-phase), depending on the composition and the cooling rate, the resulting residual stress may vary depending on whether the β phase is stable or metastable.The grain structure and size are critical issues, since thin films with finer grains or columnar structures can have different stress states due to variations in atomic packing efficiency and grain boundary energy [85]. Small grains with constrained movement can introduce compressive stress and can improve adhesion to the substrate [87]. On the other hand, excess of compressive stress may lead to cracking or delamination if the stress becomes too high. In practice, both compressive and tensile stresses coexist within a thin film, and the resulting residual stress is the balance of these two opposite forces [85].

As seen until here, there are many different parameters involved in a thin film growth process, this turns the sputter deposition into a process with a high level of complexity, hence a wide variety of results, depending on the studied system, and consequently, alternative interpretations for each result are expected. For that reason, different research groups in the last fifty years have attempted different approaches pursuing to explain the physical and mechanical properties observed on thin films [86, 89]. As mentioned before, the crystal structure and temperature of the substrate, the nature of the deposited species, and their energy are factors that affect the growth mode of the film and its properties; for instance, the preferential orientation and the presence of strain that produces residual stresses are widely known [88, 89], the deposition process occurs far from equilibrium, this mean that the resulting material is not expected to be in a stable state [88]. Hence, this out of equilibrium state of the system also indicates that the atoms are not in complete relaxation positions, which contributes to create intrinsic residual stresses within the film. According with Grabow and colleagues [25], it is expected to find strain in the majority of the systems ought to intrinsic surface stress. Intrinsic stresses lead to a significant amount of strain energy within the films. These intrinsic stresses in magnetron sputtering deposited thin films tend to increase with the addition of alloying elements, as reported by Windishman [90].

A correlation between the inert gas low pressure and compression stresses have been observed. Compression stresses can be associated with low work pressures, among various factors, for example atoms mobility [89].

Chason *et al.* [84, 85, 91] studied the origin of compressive residual stress in polycrystalline thin films by developing kinetic equations to describe the evolution of residual stress and its dependence on growth parameters. During thin film growth the surface presents high chemical potential, the driving force for compressive stress generation. The rising in chemical potential is led by the deposition of atoms. At higher chemical potential the atoms can flow to the grain boundaries, and a subsequent excess of atoms accumulated into the grain boundary, i.e. at the triple junction, will cause compressive stress in the film. The triple junction is a point in common for the grain of the film, where the layers in the adjacent grains grow together to form new segments of grain boundary. Finally, the compressive stress caused by this excess of atoms will increase the chemical potential of the atoms now localized in the grain boundary and the driving force for additional flow of atoms decreases and a steady state of compressive stress will be achieved. A schematic representation of the geometry for modeling the residual stress at the triple junction is depicted in Figure 2.29 [84].

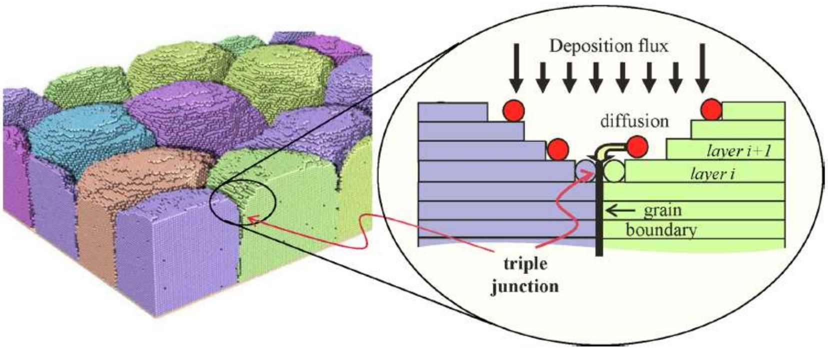

Figure 2.29 – Schematic representation of the triple junction modeling [84].

Compressive stress is typically better for adhesion and durability, but must be managed to avoid over-compression that can lead to buckling and delamination. Tensile stress can compromise mechanical performance, making the film prone to cracking under load or thermal cycling, and can also lead to buckling and delamination [92, 93], as observed in experiments carried out by Abermann [94] with the so-called type I and type II materials, low atomic mobility and high atomic mobility respectively. Low atomic mobility is associated with materials with high melting points (i.e. Fe, Ti, Nb, etc.) as counterpart, high atomic mobility has to do with low melting points (i.e. Au, Ag, Cu, etc.). The results showed a correlation between mobility and residual stress. Type I (high melting point) exhibited an evolution on the measurements that indicates just tensile stress in the films. As the low mobility suppresses grain growth, these films tend to growth with columnar morphology. Low atom mobility (high melting point) is more prone to tensile stress, and high atom mobility (low melting point) produces compressive stress. In some cases, mobility is affected by the nature of deposition process, for instance: atoms with no additional but just thermal energy (e.g. like in evaporation and electrodeposition). However, additional effects that can be induced by deposition of energetic species as occur in sputter deposition [84], and this fact explains why high melting point elements can gain higher mobility.Another factor often associated with densification is the formation of higher ‘smoothness’ in the film surface, that also leads to compressive stress, since “a more uniform surface is typically associated with higher compressive stress, due to fewer relaxation points, higher density, and more strain distribution” [84].

Yang *et al.* [95], intentionally produced porous Ti-Mo and Ti-Nb α and β alloys for biomedical application by means of gelcasting process. The microstructural and mechanical properties were characterized. The compressive strength increased, and the elastic modulus decreased until values were more similar with human tissue (about 5-18 GPa), besides the osteointegration significantly improved. The fabrication of porous surface or implants is reported in the literature, including processes such as powder metallurgy and plasma spray coating [96]. This agrees with the fact that a perfectly polished and defect free surface on the implant surface could result undesirable, but at the same time the process must be strictly controlled to obtain the appropriate percentage of porosity. Considering the inclusion of pores in thin films for biomedical applications would be a more realistic approach.

3 MATERIALS AND METHODS

3.1 Materials

High purity (99.99%)Ti, Nb, and Mo were used as target materials, and AISI 316L stainless steel disks with 15 mm in diameter and 1 mm thickness were used as substrates. The disk samples are shown in Figure 3.1.

The metallographic preparation was performed by SiC sand-papers mesh: 80, 120, 240, 320, 400, 600, 800, 1200, 1500, 2000, 2500, 3000, and 5000. Further polishing was made using diamond suspension of 3 and 1 μm. After polishing, all samples were submitted to ultrasonic bath with soapy water for 15 minutes, followed by ketone immersion for 15 minutes as well, and finally cleaned with isopropyl alcohol 90%.

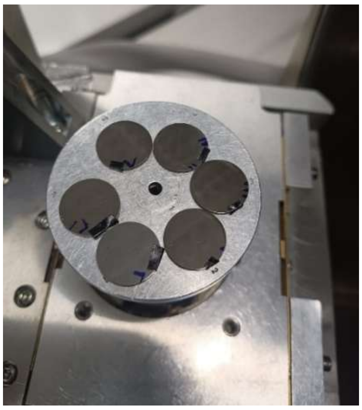

Figure 3.1 – Substrate samples of AISI 316L stainless steel.

3.2 Deposition of the Coatings

From here on, the word “coating” will be used instead of “thin film”, since thin films are associated with high-tech applications. In contrast, coatings are generally thicker and used for broader applications, such as protective and biomedical coatings. The chemical compositions of the coatings were selected according to the literature in order to ensure the β phase stabilization. Four compositions of Ti-Nb-Mo were chosen: $Ti_{75}Nb_{20}Mo_{5}$, $Ti_{73}Nb_{20}Mo_{7}$, $Ti_{71}Nb_{20}Mo_{9}$, and $Ti_{69}Nb_{20}Mo_{11}$ (at.%) [97, 98]. The $Ti_{71}Nb_{29}$ (the nominal composition was set as $Ti_{80}Nb_{20}$) was also produced for comparison. Those compositions were obtained by varying the power applied to the targets, and the power values are indicated in Table 3.1. The chemical compositions are identified as S1, S2, S3, S4, and S5, respectively.

3.2.1 Deposition of $Ti_{80-x}Nb_{20}Mo_x$ and $Ti_{80}Nb_{20}$ Coatings by DCMS

The deposition of this set of coatings was carried out at the Microfabrication Laboratory of the Brazilian Nanotechnology National Laboratory (LNNano) of the Brazilian Center for Research in Energy and Materials (CNPEM). The equipment, depicted in Figure 3.2, is a DCMS AJA Orion 8 Phase II J, a high-performance thin film deposition system equipped with a fast-cycle load-lock device which eliminates the need to vent the process chamber for loading the substrates, reducing the pump down time and contaminations of the targets and inner chamber surfaces. It utilizes motorized rotating substrate holder to achieve film uniform. The equipment offers different deposition modes: DCMS, RF, o-sputtering, balanced and unbalanced; also allowing control of temperature and thickness control. The maximum coating thickness that can be achieved is 1 µm, and five samples of each composition were prepared. In Table 3.1 are listed the deposition parameters that were used in the deposition process [4, 69].

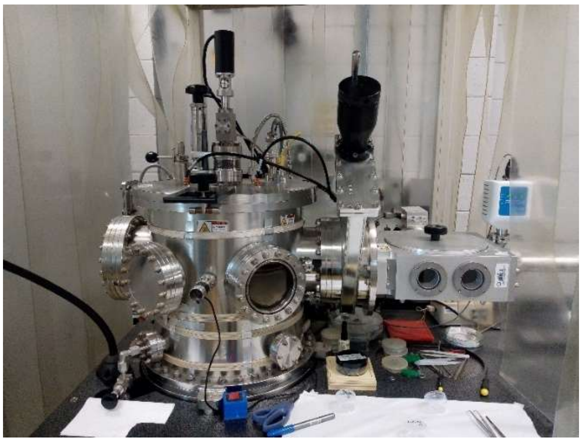

Figure 3.2 – The AJA Orion 8 Phase II J DCMS equipment at the LNNano facilities. Source: The author.

Table 3.1 – AJA Orion 8 Phase II J DCMS equipment deposition parameters.

Alloy	**S1**	**S2**	**S3**	**S4**	**S5**
Sample quantity	5	5	5	5	1
Temperature (°C)	200	200	200	200	200
Base Pressure (Torr)	4×10^{-8}	4×10^{-8}	9×10^{-8}	6×10^{-8}	1×10^{-7}
Work Pressure (mTorr)	3	3	3	3	3
Argon flux (sccm)	20	20	20	20	20
Power density on Ti (W/cm²)	320	320	320	320	300
Power density on Nb (W/cm²)	80	80	80	80	100
Power density on Mo (W/cm²)	30	40	50	60	-

3.2 Characterization Techniques

3.2.1 X-ray Diffraction (XRD)

X-ray is a form of short wavelength and high energy electromagnetic radiation, on the order of the atomic interplanar distances between atoms. The X-ray diffraction (XRD) is a technique used to determine the crystallographic structure of materials, based on the constructive interference of incident X-rays scattered by the atoms in a crystal lattice. This method provides insights into the arrangement of atoms in solids, identifying phases, measuring lattice parameters, and assessing crystallinity. The XRD method principle is based on the Bragg's law, used to calculate the interplanar distances of the crystal lattice as function of the X-ray wavelength and the angle formed between the impinging ray and the crystallographic plane. The Bragg's law can be expressed by the equation (3) as follows:

$$n\lambda = 2d_{hkl}sin\theta \qquad eq.(3)$$

Where:

n : order of reflection, an integer number consistent with $sin\theta$ not exceeding the unity

λ : wavelength of the incident X-ray

θ : angle formed between the incident X-ray and the plane of atoms
d : interplanar distance between two adjacent and parallel crystallographic planes of the material, as function of the lattice parameter and the Miller indices (h, k, l).

The interplanar distance (d_{hkl}), for cubic crystal symmetric structures is calculated using the following equation:

$$d_{hkl} = \frac{a}{\sqrt{h^2 + k^2 + l^2}} \qquad eq. (4)$$

a : lattice parameter
h, k, l : Miller indices

There exist various XRD techniques such as: powder diffraction (the most common), single crystal, grazing incidence (GIXRD) and high resolution (HRXRD). In this work, it was employed the GIXRD method since it is the most suitable for analyzing thin films and coatings. The XRD analysis was performed with a diffractometer Rigaku (Figure 3.3) with Bragg-Bentano mode (θ/2θ), Cu k-alpha radiation 40 kV, 40 mA. The equipment is located at the Sao Carlos Institute of Physics (IFSC) of the University of São Paulo. The indexation of the diffracted peaks was performed using the Crystallograpica Seachmatch software.

Figure 3.3 – Rigaku Diffractometer installed at IFSC.

3.2.2 Grazing-Incidence X-ray Diffraction (GIXRD)

GIXRD is a powerful type of XRD technique used for structural analysis of thin films, surfaces, interfaces, and multilayer coatings. In this method, a monochromatic X-ray beam (e.g., Mo or Cu K α radiation) impinges at a very low angle of incidence onto a sample, ensuring that the analysis is confined to the near-surface region. It is performed with high sensitivity and precision by means of an X-ray beam with a very low incidence angle, between 0,5° to 2° (depending on the specimen dimensions) [99]. The incidence angle is fixed, while the grains in the surface material exhibit random orientation. The beam is scattered inside the sample and the diffracted beams are detected by a 2θ scanning configuration. As the incidence angle increases its penetration, the depth increases as well, and this is the mean reason to maintain a very low angle to probe thin films (less than 1 micrometer of thickness) in order to avoid undesirable substrate contribution [99].

The GIXRD techniques, including high resolution GIXRD, are employed to obtain different features, such as: phase identification, microstructural determination, degree of crystallinity, lattice parameters, crystallite size and strain determination, uniform and non-uniform strains, preferred orientation (texture coefficient), depth profiling of multilayer, and residual stress determination [100].

Residual stress measurements using GIXRD rely on analyzing changes in the crystalline lattice spacings produced by distortions induced by the action of intrinsic and extrinsic stresses. XRD measures these spacing (*d*) using Bragg's law, and any change in *d* will shift the diffraction angle, thus residual stresses cause shifts in the diffraction peaks as the lattice planes experience tensile or compressive stresses. The diffraction peaks are measured collecting diffraction patterns at various tilt angles (ψ - rotation angles of the sample), then the *d* shift is calculated as function of ψ, also applying stress-strain relations considering elastic modulus (E) and Poisson's ratio (ν) [100]. The $sin^2\psi$ method is used to analyze data using the following expression:

$$\sigma = \frac{E}{1+\nu}\frac{\Delta d/d}{sin^2\psi} \qquad eq.(5)$$

Where:

σ: Residual stress

E: Young's modulus

v: Piosson's ratio

Δd/d: Relative change in the lattice spacing due to stress

ψ: Tilt (rotation) angle of the sample

The GIXRD mode was used to measure residual stress in the coatings, and it was carried out with a four circles diffractometer PANanalytical X'Pert PRO MRD-XL (Figure 3.4), installed at the CEPAME Research Center of the

Department of Materials Engineering of the Sao Carlos School of Engineering of USP.

Figure 3.4 – Diffractometer PANanalytical X'Pert PRO, MRD-XL. Source:author.

3.3 Scanning electron microscopy (SEM) and energy dispersive X-ray spectroscopy (EDS)

Electron microscopy is an imaging technique that uses beams of electrons to magnify and analyze the structure of materials at high resolutions. It enables visualization of structures at the nanoscale. It works using an electron gun that emits a beam of electrons. These electrons are accelerated using a high voltage (ranging from a few kilovolts to several hundred kilovolts), then electromagnetic lenses are used to focus and direct the electron beam toward the sample. The system operates in a vacuum to prevent the electrons from scattering due to interactions with air molecules [101].

Once the electron beam strikes the sample, it interacts with the atoms in the material, and various signals can be collected, such as secondary electrons (SE), backscattered electrons (BSE), characteristic X-rays (that can be used to analyze chemical compositions), Auger electrons (AE), and Bremsstrahlung [101]. The detectors collect these signals to generate images. The energy dispersive X-ray spectroscopy (EDS) is an analytical technique used coupled with electron microscopy in order to determine the elemental composition of materials. It works by detecting the characteristic X-rays emitted from the chemical elements present in the sample in consequence of the interaction with the electron beam.

The microstructure, morphology, and chemical composition of the coatings were analyzed using a TESCAN MIRA microscope coupled with an EDS detector Bruker installed at LCE/DEMa/UFSCar, and it is displayed in Figure 3.5. The chemical mappings, spectra, and images were obtained. The grain sizes were measured using the software ImageJ, by calculating the average length of the grains.

Figure 3.5 – TESCAN MIRA microscope coupled with a Bruker EDS detector. Source: the author.

3.6 Atomic Force Microscopy (AFM)

Atomic force microscopy (AFM) is a high-resolution imaging technique used to analyze surfaces at nanometer scale. It is a type of scanning probe microscopy (SPM) that provides information about surface topography, mechanical, electrical, and chemical properties of materials. AFM works using a sharp probe attached to a flexible cantilever to scan the sample surface. The probe-sample interaction generates electrostatic forces that cause the cantilever to be deflected. A laser beam is focused on the back of the cantilever and reflected onto a photodetector that measures the deflections of the cantilever, providing data about surface features [102].

The topographical characterization (rugosity) measurements ware carried out using a Bruker Nanoscope V Multimode with ScanAsyst. Images having 5 x 5 μm and 1 x 1 μm areas were produced. The rugosity values and images were obtained by means of the NanoScope Analysis and Gwyddion software, respectively. The equipment is installed at LCE/DEMa/UFSCar, and is illustrated in Figure 3.6.

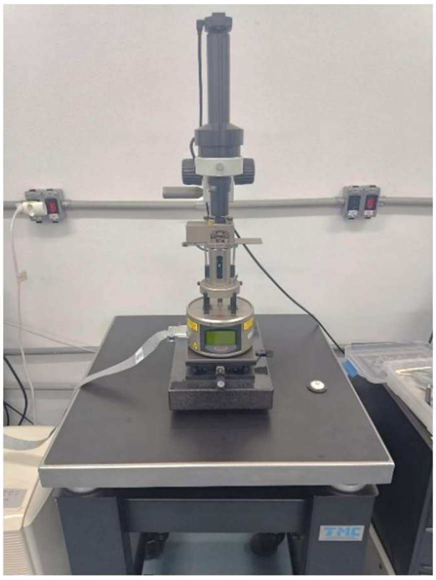

Figure 3.6 – AFM Bruker Nanoscope V Multimode ScanAsyst. Source: author.

3.7 Nanohardness Test

The nanohardness test involves the use of a Berkovich-type indenter, which penetrates the sample surface until a depth less than 10% of the total film thickness, ensuring that it does not reach the substrate, that could lead to undesirable results in the measurement. A continuous incremental load is applied, and the load value will depend on the material type and the film thickness. The maximum load is kept for a specified time period and is removed at approximately the same rate at which it was applied. A curve of loading-unloading is generated, that permits calculating both the hardness and the elastic modulus values. When the load is removed, the elastic material recovery is measured, then the hardness is calculated using the maximum load divided by the contact area of the indentation and the elastic modulus is derived from the unloading curve [103].

The measurements were carried out by means of of an Anton Paar – NTHIT^2 nanoindentation tester (Figure 3.7) with a Berkovich-type indenter. The equipment is installed at the Vitreous Materials Laboratory (LaMaV) of DEMa/UFSCar. It was applied a maximum load of 0.01 N, at a loading and unloading rate of 0.02 Nm^{-1}, pause time of 15 seconds, and Poisson's ratio of 0.3.

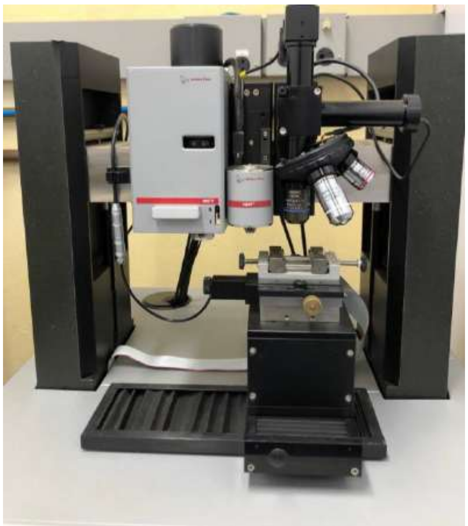

Figure 3.7 – Anton Paar – NTH^2 Nanoindentation tester. Source: author.

3.8 Pontentiodynamic Polarization (PP) test

The polarization is an electrochemical phenomenon in which the electrochemical equilibrium potential (the so-called E_{corr}) experiments a deviation. This means that the E_{corr} at which the anodic and cathodic reactions should reach an equal rate, and consequently instead of making the net current being zero, it exhibits a difference. In the potentiodynamic polarization method a controlled voltage (potential) is applied to a metal sample (working electrode), meanwhile, the resulting current flow is measured. The potential is varied at a fixed rate (the reason to call it potentiodynamic), and the current response (I_{corr}) is plotted to generate a polarization curve [104].

The device used to perform the PP test was a Gamry potentiostat, reference model 3000 (Figure 3.8), installed at the Corrosion Laboratory at the DeMA/UFSCar. The device is coupled with the DC105^{TM} DC Corrosion software for data acquisition, and the Echem Analyst^{TM} software for data processing and visualization.

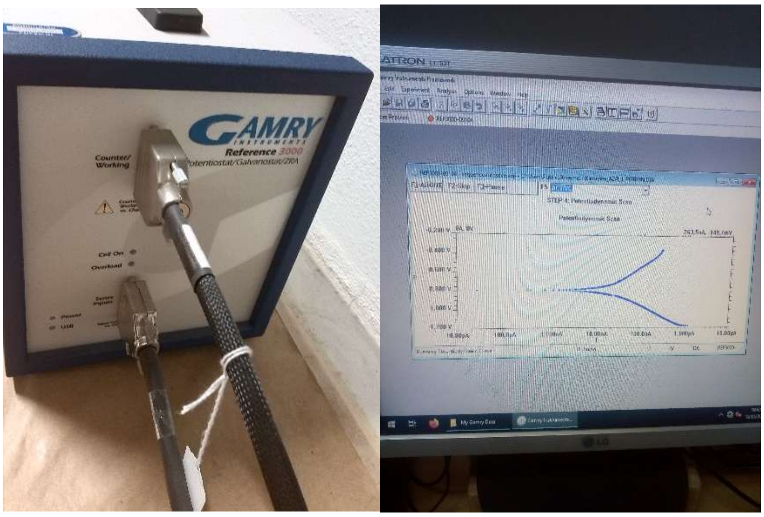

Figure 3.8 – Gammry 3000 otentiostat and DC105TM DC Corrosion software. Source: author.

The experiment setup for PP, shown in Figure 3.9, consisted of an electrochemical cell of silver-silver chloride (Ag/AgCl) or calomel reference electrode (SCE) immersed in a potassium chloride (KCl) saturated dissolution, a platinum (Pt) counter-electrode, and the samples acting as working electrode immersed in a 0.6 M NaCl aqueous dissolution, at room standard temperature. The samples were submitted to open circuit conditions for 60 minutes until the steady state was reached, so the potential reached was set as open circuit potential (E_{OC}). The sweep rate was set in 1mV/s, and the starting point set at a potential of 400 mV under E_{OC} value, finalizing with a new potential value in which the i_{corr} reached a value of 1 mA/cm^2. The area exposed to the dissolution during the test was 0.2 cm^2.

Figure 3.9 – Electrochemical cell setup for PP and EIS tests. Source: author.

3.10 Calculation of Phase Diagrams

The CALPHAD (Computer Coupling of Phase Diagrams and Thermochemistry) method is a thermodynamic modeling technique in which the Gibbs energies are calculated as function of pressure, chemical composition, and temperature in order to obtain binary or pseudo-binary equilibrium phase diagrams, predicting the formation of phases, intermetallic, or secondary phases. The Gibbs energies calculated for pure, binary, and ternary systems are extrapolated to multicomponent systems [105].

In this work, the pseudo-binary phase diagrams of the Ti-Nb-Mo compositions were obtained by means of thermodynamic calculations, using the ThermoCalc software (academic version) using the TCTI3 database, in order to obtain a preliminary approach of what phases are expected to form in the coatings.

4 RESULTS AND DISCUSSION

4.1 Scanning Electron Microscopy (SEM) and Energy Dispersive Spectroscopy (EDS)

Semi-quantitative analysis of the samples was performed using EDS technique to obtain the chemical compositions (%at), and the values are summarized in Table 4.1., that also indicates the power applied to the molybdenum target for each case, except sample 5.

Table 4.1 – Chemical composition of the samples obtained with EDS.

SAMPLE	Ti % at.	Nb % at.	Mo % at.	P (W)
S1	74	21	5	30
S2	74	19	7	40
S3	72	19	9	50
S4	67	22	11	60
S5	71	29	-	-

to the results above, it can be observed that the Mo content increases with the increment of the applied power. S5 is used as reference and only Ti and Nb were deposited, using power values of 300 W for Ti and 100 W for Nb. For the ternary coatings, the power applied to Ti and Nb targets were kept fixed at 320 W and 80 W, respectively. These values are higher than the power employed for the Mo target, and variations in both the Ti and Nb concentrations were observed, showing a tendency of decreasing in Ti and Nb concentrations. This phenomenon is explained by the fact that when a third element (Mo) is added, a redistribution of atoms occurs on the surface in order to reach the lowest energetic level of the system, resulting in lesser Ti and Nb concentrations on the homogeneous surface as compared with the Ti-Nb coating (S5). The formation of such coating surfaces with homogeneous distribution of the elements was corroborated by the chemical mappings obtained by EDS that are presented in Figure 4.1.

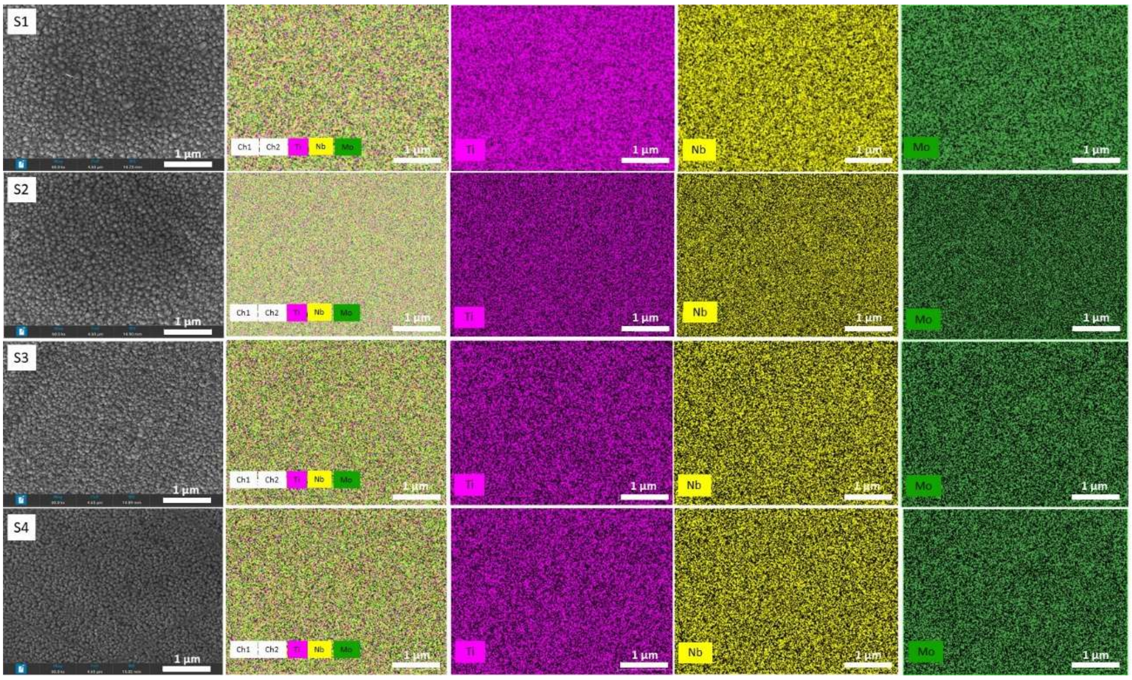

Figure 4.1 – Chemical mappings of the coating surfaces obtained by EDS.

Topographical Topographical images of the coating surfaces were obtained by SEM in secondary electrons mode (SE). General overviews of the S1, S2, S3, and S4 samples are depicted in Figure 4.2. It can be noticed the presence of clusters and pores in all samples, varying the quantity for each of them. It is important to point out that in the context of the present work, the term “cluster” must be understood as an analogy of the cluster definition used in geology, i.e. a group of crystals growing together from a shared base, and in this case, the grains (crystals) are forming the kind of structures observed here. The quantification of such pores and clusters will be presented later. Figure 4.3 displays SEM images in SE mode at magnifications of 35,000x (left side) and 100,000x (right side) showing a detail of a pore found in S3, and next to it, a cranberry shaped cluster. The pore seems to extend down to the substrate surface, and this is confirmed by the Fe EDS mapping presented in Figure 4.4 that clearly shows that Fe is the only element detected inside the pore. As detailed in the 100,000x image (Fig. 4.4.b), the grains are perfectly piled. They look like being forming grain layers, some of them located at the edge of the coating surface, exhibiting an undefined morphology.

Figure 4.5 shows three different higher magnifications for all samples as follows: 60,000x, 120,000x, and 300,000x. Each row of images in Figure 4.5 corresponds to a specific chemical composition, showing micrographs at three different magnifications, from left to right: 60000x, 120000x and 300000x. The grains are nanometric and some of them appear faceted, while others present elongated shapes, resembling the appearance of creek rocks. At first sight, it can be observed that the grain size decreases as the Mo content increases. In contrast, S5 (with no Mo content) exhibits even smaller grain sizes as compared to S4, the sample with the smallest grain sizes among the samples containing Mo. It can be perceived a slight difference in grain sizes among S1 and S2.

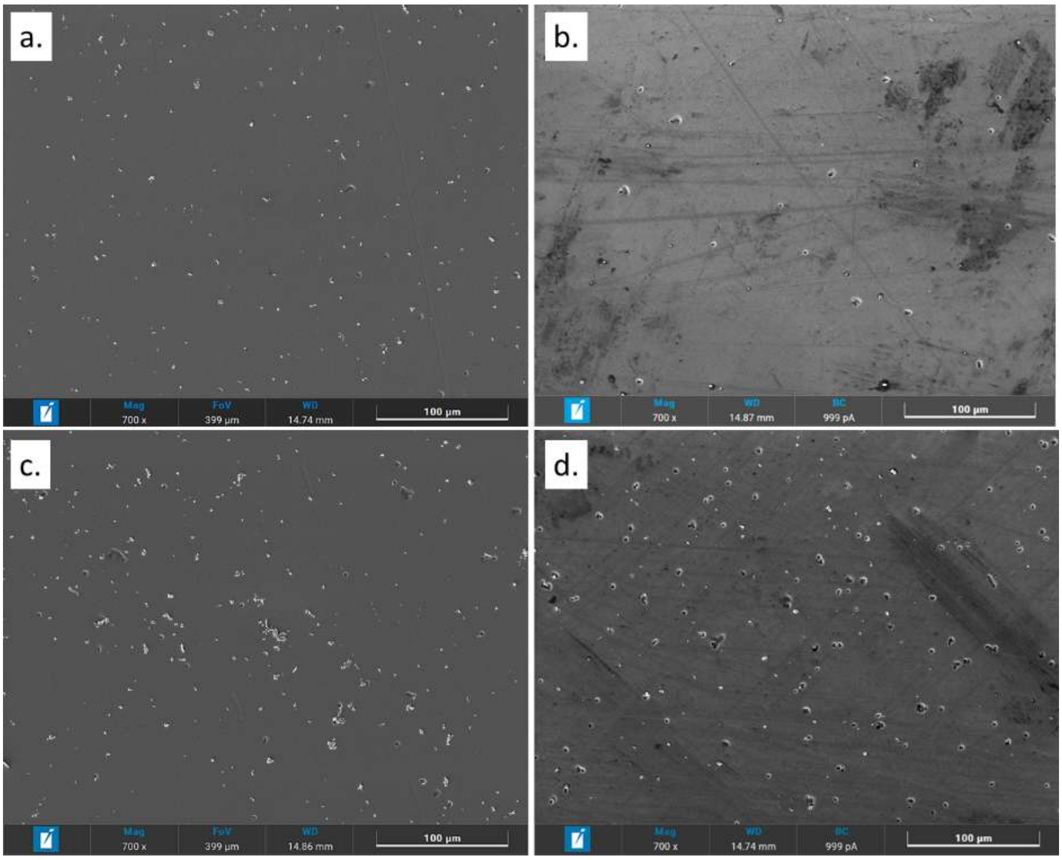

Figure 4.2 – SEM images obtained in SE mode for the (a) $Ti_{74}Nb_{21}Mo_5$ (S1), (b) $Ti_{74}Nb_{19}Mo_7$ coating (S2), (c) $Ti_{72}Nb_{19}Mo_9$ coating (S3), and (d) $Ti_{67}Nb_{22}Mo_{11}$ (S4) (S4) coatings.

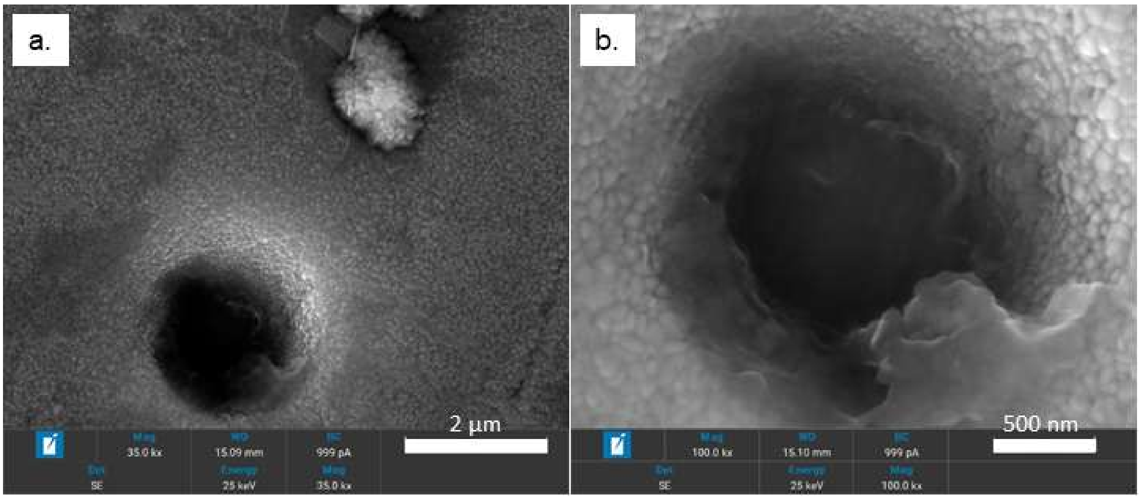

Figure 4.3 – SEM images in SE mode at for (a) 35,000x and (b) 100,000x magnifications, detailing a pore found in S3.

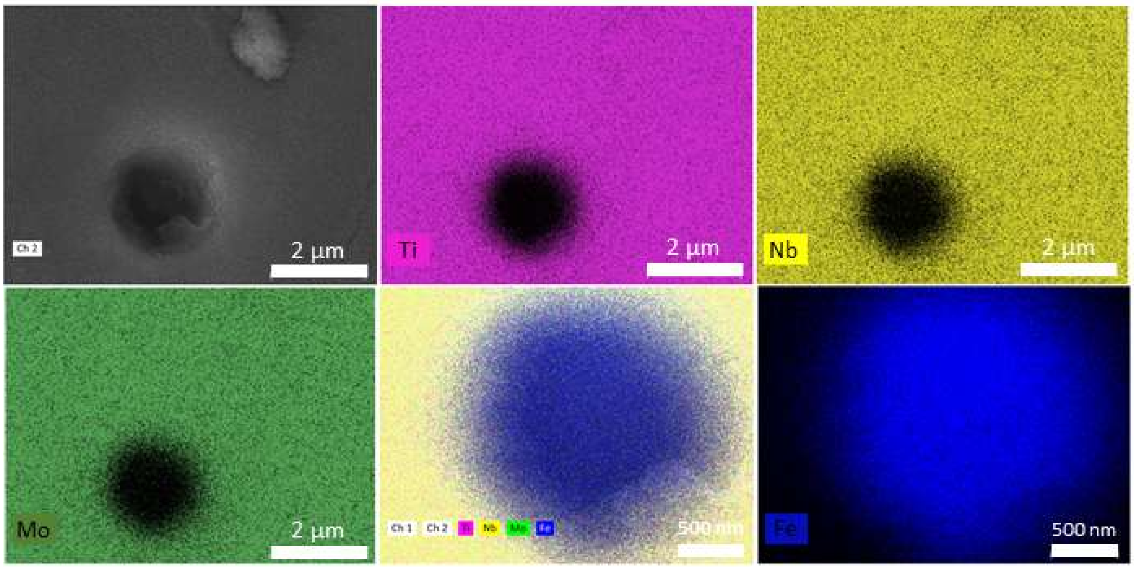

Figure 4.4 – EDS chemical mappings of a pore in S3, including a Fe scan.

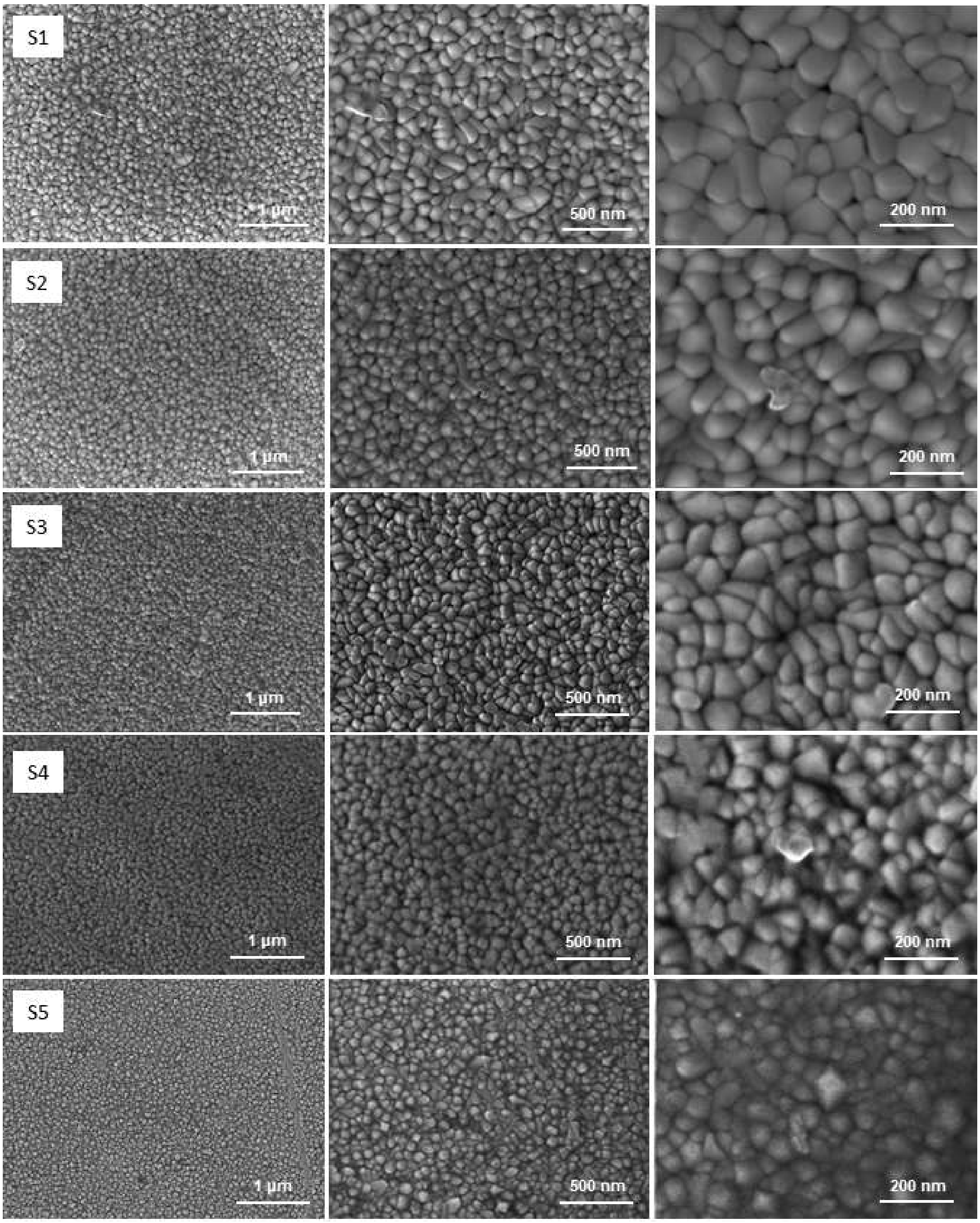

Figure 4.5 – SEM Images in SE mode showing magnifications of 60,000x, 120,000x, and 300,000x for all samples.

In Figure 4.5 tiny spaces (nanometric voids) can be noticed between some of the grains, however, there is no significant density of these spaces along the coating surface. It is a normal condition due to the natural configuration of the atoms as they form the grains during the deposition process delimitating the grain boundaries. The average grain size was determined using ImageJ 2.0 software.

The mean length of the grains was determined by analyzing the images having a magnification of 300,000x. The results are summarized in Table 4.2. and a chart of the grain size versus the power applied to the Mo target is illustrated in Figure 4.6. It can be observed that there is a reduction in the average grain size related to the increase in the power applied to the Mo target, and as a consequence, related to the increase in Mo concentration. The smallest grain size is observed for the sample with no Mo content ($Ti_{71}Nb_{29}$).

Table 4.2 – Average grain size

Sample	Applied power (W)	Mo (%at.)	Grain size (nm)
S1	30	5	134 ± 30
S2	40	7	114 ± 31
S3	50	9	89 ± 18
S4	60	11	70 ± 17
S5	0	0	63 ± 19

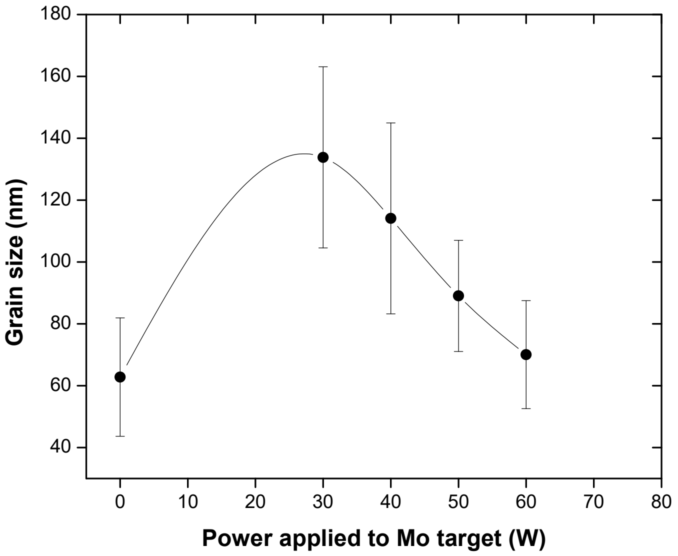

Figure 4.6 – Grain size versus power applied to the Mo target.

For all Ti-Nb-Mo coatings, nucleation and growth of three-dimensional clusters occurred, as shown in Figure 4.7. Different types of morphologies are observed, some of them resemble cranberries (Figure 4.7, S2) and others have the shape of cactus (Figure 4.7, S4) and cauliflower (Figure 4.7, S3). The S1 coating (5% at. Mo) presents a morphology that looks like natural quartz crystal clusters amethyst-like shape [106], as can be seen in Figure 4.8 (a) and (b) that shows a comparison between one of the clusters and a real amethyst quartz. The cluster exhibits tetrahedral structures, as observed in amethyst, which, in a homologous way, starts to grow from little clusters in a supersaturated solution (excess of atoms).

It is important to point out that reports of such morphologies or general views of thin films and coatings are practically inexistence. As a matter of fact, there are always the same type of images showing very little areas of the surface and the cross section, using high magnifications (usually 100,000x or above). Figure 4.9 displays the EDS chemical mapping of clusters for each Ti-Nb-Mo composition. As can be seen, there is a homogeneous distribution of the elements in the clusters and on the coating surfaces (as seen in Figure 4.1). Some of the clusters are surrounded by voids making part of their bases, those voids are the dark regions noted in the EDS images.

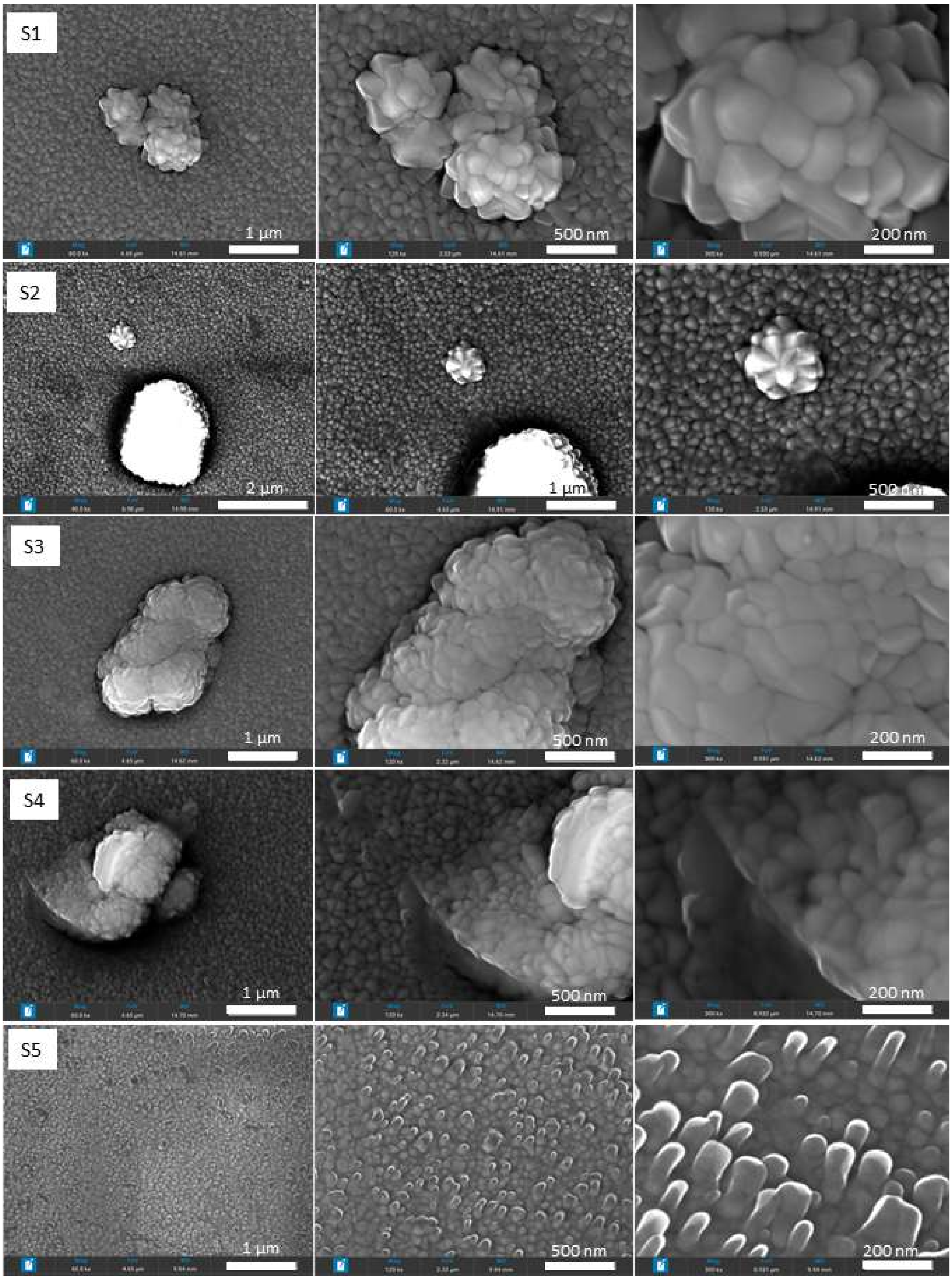

Figure 4.7 – SEM images obtained in SE mode of the cluster formation.

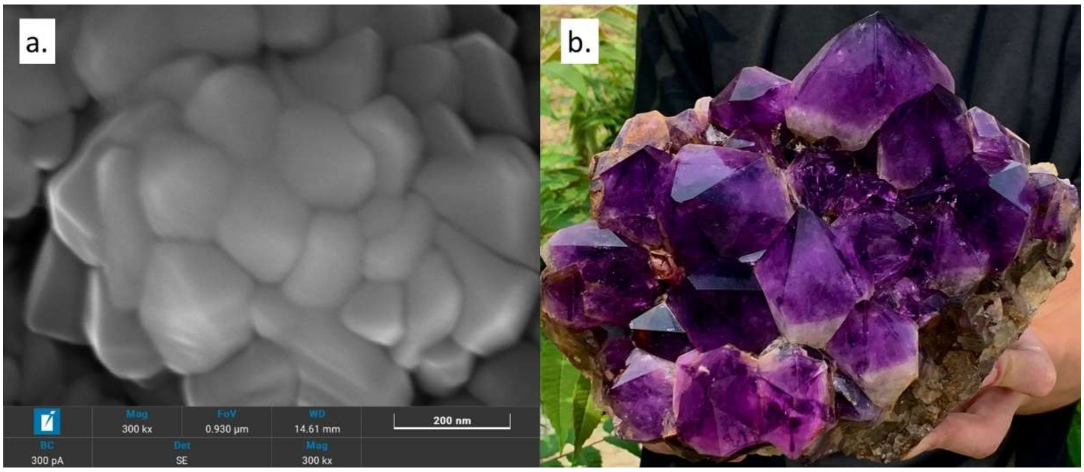

Figure 4.8 – Comparison between (a) amethyst-like shape clusters and (b) natural amethyst quartz crystal clusters.

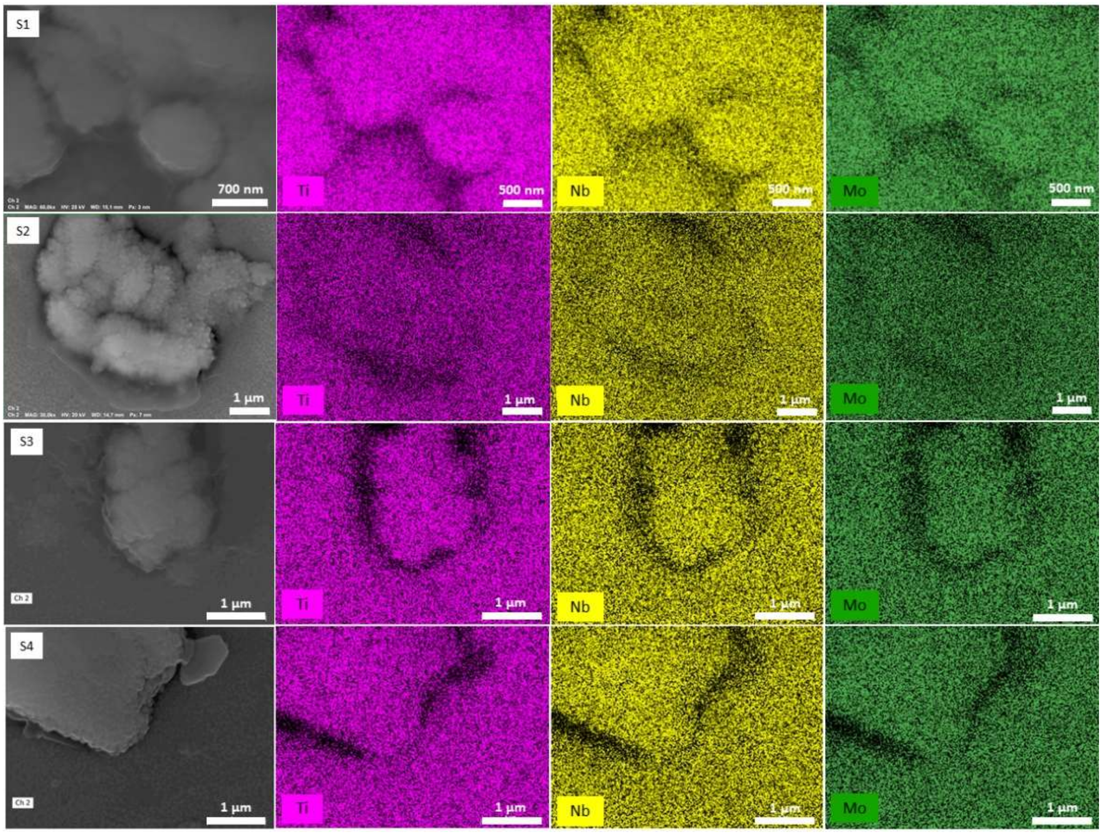

Figure 4.9 – EDS qualitative chemical analysis of the clusters and matrix areas on the coating surfaces.

Figure 4.10 shows the SEM cross-section images obtained in SE mode for the coatings with a magnification of 75,000x. The thicknesses for the four samples containing Mo were measured, resulting in (a) 671 nm for S1, (b) 841 nm for S2, (c) 573 nm for S3, and (d) 693 for S4. As can be noticed, in general, a thickness enlargement occurs with the increase in the power applied to the Mo target [107]. Figure 4.11 displays a wider view of S4 (magnification of 30,000x) with SEM images obtained in SE (left side) and BSE (right side) modes. It is possible to recognize 3D clusters on the surface, and the BSE mode micrograph corroborates the EDS results: the clusters are formed entirely of the constituent elements (Ti, Nb, and Mo).

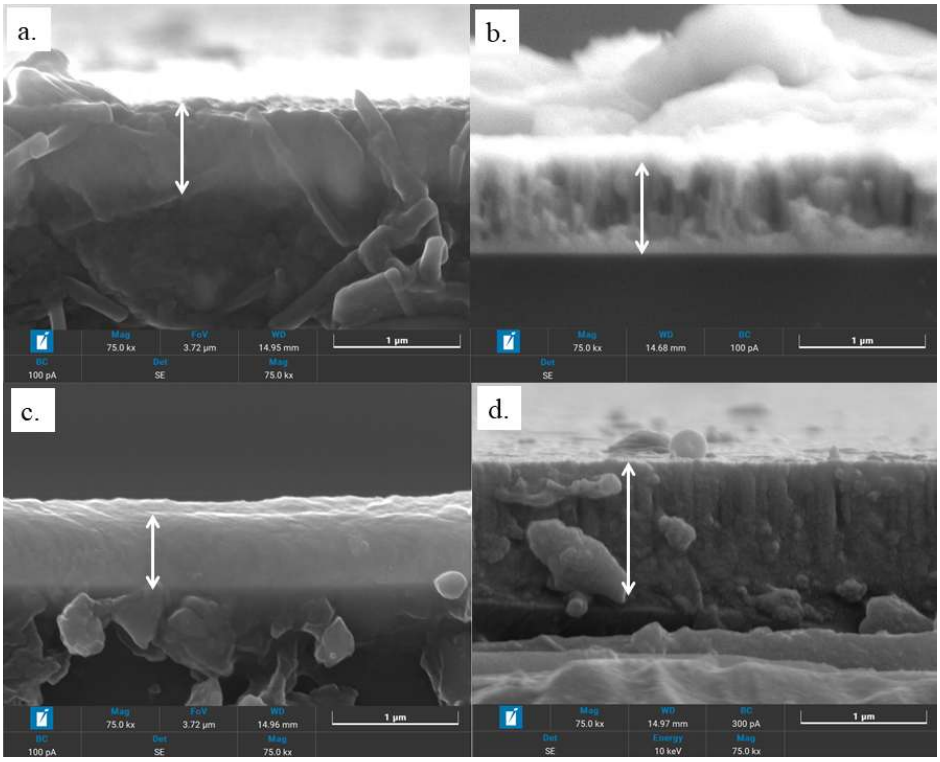

Figure 4.10 – SEM cross section images obtained in SE mode for the coatings with a magnification of 75,000x: (a) $Ti_{74}Nb_{21}Mo_5$, (b) $Ti_{74}Nb_{19}Mo_7$, (c) $Ti_{72}Nb_{19}Mo_9$, and (d) $Ti_{67}Nb_{22}Mo_{11}$.

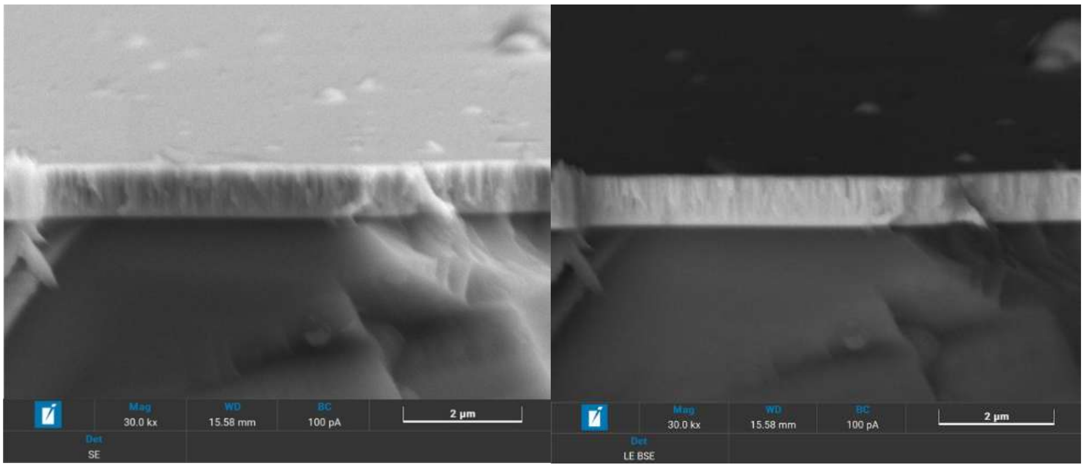

Figure 4.11 – SEM wider view images (magnification of 30,000x) of S4 obtained in SE (left) and BSE (right) modes.

S1 and S3 exhibit smoother densely packed fibrous grains, presenting a mix of characteristics between the final of zone I and the onset of zone T, presenting a competitive structure, according to Movchan's [18] and Anders' [21] growth types. A typical well defined and compacted columnar growth is more evident for S2 and S4 that exhibit an appearance characteristic of zone T and II. In Figure 4.11 it is possible to observe a biased tendency of grains to competitively grow forming a zone T structure. These growth modes are illustrated in Figure 2.10.

As previously seen in Figure 4.5, the top-surfaces of the coatings present grains associated to the column tips, where a change in the grain size can be observed as the power applied to the Mo target increased. Figures 4.10 (a) and (c) displays films that are a little bit tilted, which is more evident for S3. This can be attributed to the deposition flux, which has to do with the directional flow of the sputtered atoms as they travel from the target to the substrate [108]. This phenomenon is influenced by factors such as gas pressure. Higher pressures inside the chamber cause an increase in the atom scattering due to more frequent collisions among them, reducing their directionality. Conversely, lower pressures reduce collisions, leading to a more directional deposition flux. Thus, the films are more likely to exhibit tilted structures when there is a stronger directional deposition flux. In the present work, the deposition process was performed under very low pressure inside the chamber. In Figure 4.12 are shown the EDS cross section mappings for the coatings. Once again, the homogeneous distribution of the elements is confirmed.

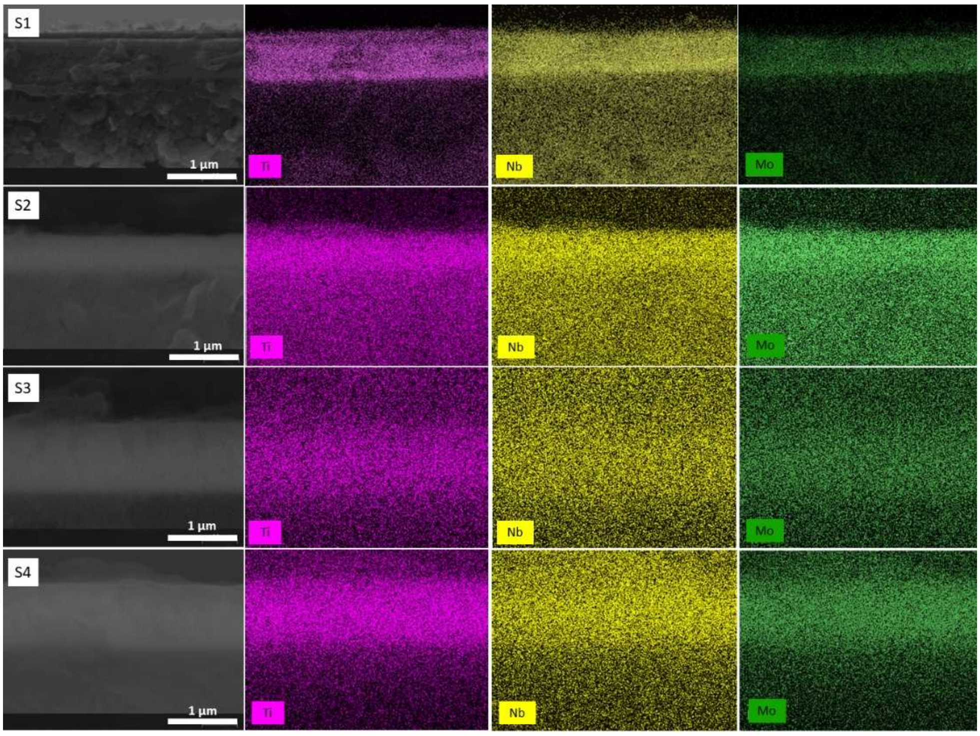

Figure 4.12 – EDS cross section mappings for the coatings: (S1) $Ti_{74}Nb_{21}Mo_5$, (S2) $Ti_{74}Nb_{19}Mo_7$, (S3) $Ti_{72}Nb_{19}Mo_9$, and (S4) $Ti_{67}Nb_{22}Mo_{11}$.

As it is well known, the formation of a thin film is a thermodynamically complex process due to the great number of variables involved; consequently, the cluster formation, whenever it occurs, is linked to various factors as well. In the first place, the nucleation phenomena that form such structures and their subsequent growth depend on the energy at which the atoms impinge the surface. When the deposition conditions provide high mobility, the atoms of the lighter elements are accelerated to the point of being reflected by the surface, preventing the formation of clusters rich in such elements. Conversely, when the deposition conditions result in low mobility, the atoms are quickly absorbed upon reaching the surface, favoring the formation of supersaturated metastable solid solutions. Despite the fact that Ti is lighter than both Nb and Mo, it occurs occurs a homogeneous distribution of the elements in the clusters as well as the matrix, as can be seen in Figure 4.9.

Grabow and colleagues [25] studied the thin film growth modes and cluster nucleation. They reported that uniform films can be produced only in a limited number of substrate-film systems. In some systems in which there exist strong interactions between the film and the substrate, it is common to produce non-uniform films with random thickness (e.g. microstructural misfit between the substrate and the film), but this strong interaction does not interfere in cluster formation, since the cluster atoms are beyond of the range of interaction; conversely, the nucleation depends on the mismatch and the temperature. The most common scenario for a non-uniform film is the formation of tridimensional clusters of the deposited material. This fact is corroborated by EDS semi-qualitative chemical analysis performed on the clusters-matrix areas, as can be seen in Figure 4.9, which exhibits the compositional homogeneity of the clusters.

Some other factors may contribute to the cluster formation. When the film growth typically occurs in a layer by layer mode, it is expected that a uniform film starts to grow. A uniform film can be metastable and, thus, this metastability can lead to the nucleation of three-dimensional clusters. Another possible cause can be the existing mismatch for the substrate-film system, where strain energy will be accumulated, acting as a driving force for the cluster formation in most cases. Besides strain, residual stress also contributes, and this will be further discussed [86].

A method used to increase the energy of ions in the plasma is to increase the power applied during the sputtering process. As they have more energy, they will collide with the target with even a higher impact, which results in a higher deposition rate. The more atoms are sputtered from the target, the higher the quantity of atoms available to be deposited onto the substrate surface, increasing the chances of obtaining thicker films. Besides, it exists a correlation between deposition rate and the atom diffusion on the film surface that helps to improve the moment transfer to the nucleation and growth of the films [107]. An excess of atoms on the surface will also contribute to the formation of clusters.

4.2 AFM

Figures 4.13 and 4.14 present the topographical AFM 3D images of the four Ti-Nb-Mo coatings, obtained within a 25 μm^2 and 1 μm^2 area., respectively. Table 4.3 presents the AFM results of surface roughness (Ra) values measured on each coating, also including the power applied to the Mo target and the grain sizes (mean length). These results show a reduction in surface roughness with the increase in the applied power, coincident with a reduction in grain size, and are corroborated by the SEM micrographs displayed previously in Figure 4.5.

The surface roughnesses range from approximately 6 to 12 nm. There is very scarce literature reporting the surface roughness for Ti-Nb-Mo thin films and/or coatings. One could intuitively assume that it is possible that less roughness on the surface could contribute to diminish the cell adhesion on the film surface, but further tests must be performed in order to corroborate this possibility.

Table 4.3 – Surface roughness results, including the power applied to the Mo target and the grain sizes.

Power Mo (W)	Ra (nm)	Grain size (nm)
30	11.6	134 ± 29
40	10.7	114 ± 31
50	9.5	89 ± 18
60	6.4	70 ± 17
0	-	63 ± 19

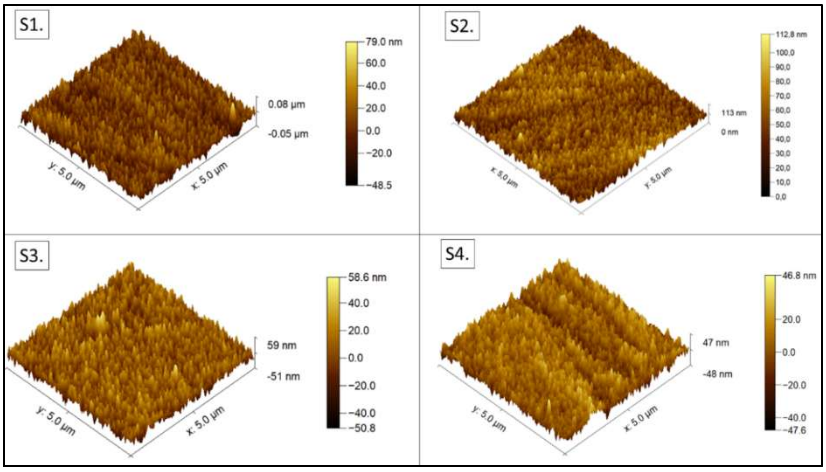

Figure 4.13 – AFM 3D images of the Ti-Nb-Mo coating topographies. Analyzed area 25 µm^2.

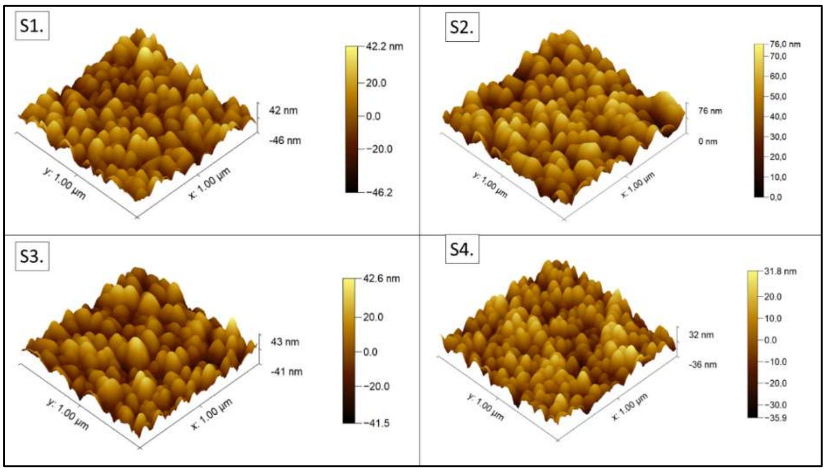

Figure 4.14 – AFM 3D images of the Ti-Nb-Mo coating topographies. Analyzed area 1 µm^2.

When compared with other processes reported in the literature, for instance the deposition of Ti thin films by HiPIMS, where the applied power is way higher (in the order of 1500 to 7900 W), surface roughness ranges from 14 up to 22 nm, indicating certain Ra dependance on the applied power [109]. It is important to note that, inspite of the expressive difference in the order of magnitude of the applied power, the lowest Ra value reported in the literature, 14 nm (obtained at 4500 W), is close to the Ra values obtained in this work, 12 nm (at only 30 W). In practice, rougher surfaces enhance the biological integration, conversely, smoother surfaces are preferred for wear resistance applications.

Thus, a balance must be reached in the case of biomedical application, since both features are important and depend on the specific biomedical device. Experiments must be carried out to accomplish the more suitable values of Ra.

4.3 Computational Thermodynamic calculations

Thermodynamic calculations were carried out using ThermoCalc software and pseudo-binary phase diagrams were obtained for each composition, as shown in Figures 4.15, 4.16, 4.17, and 4.18. It can be noticed the occurrence of only the β phase above β-transus temperature, which tends to increase with Mo content at the given Nb and Ti concentrations. The melting point also increases with the increasing in Mo content, since Mo presents the higher melting point among these refractory metals.

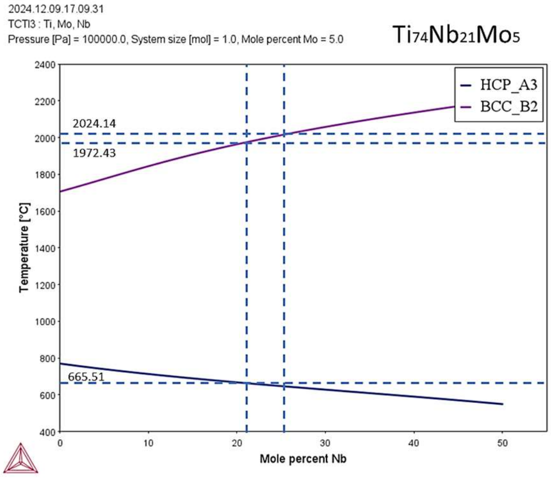

Figure 4.15 Pseudo-binary phase diagram for the $Ti_{74}Nb_{21}Mo_5$ alloy.

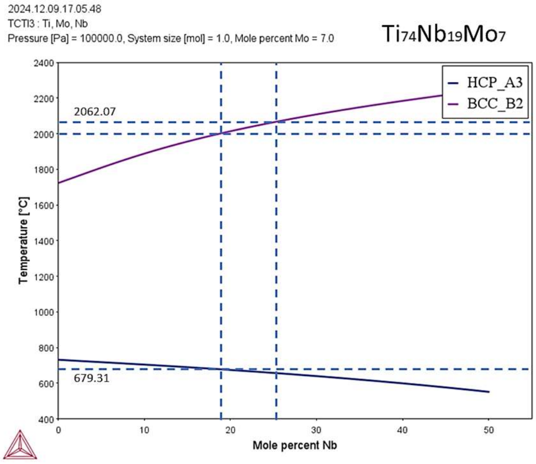

Figure 4.16 – Pseudo-binary phase diagram for the $Ti_{74}Nb_{19}Mo_7$ alloy.

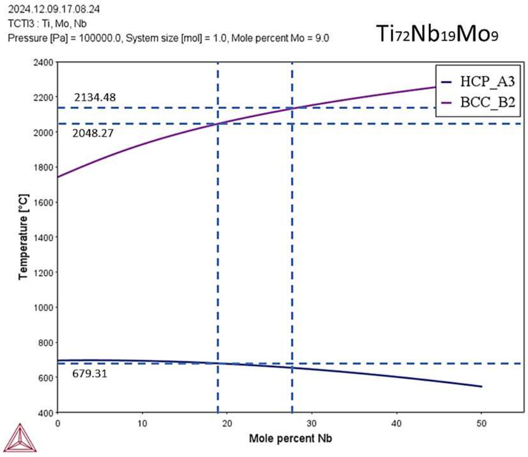

Figure 4.17 – Pseudo-binary phase diagram for the $Ti_{72}Nb_{19}Mo_9$ alloy.

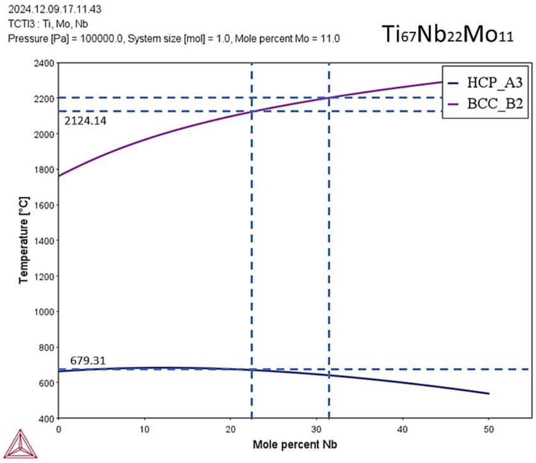

Figure 4.18 – Pseudo-binary phase diagram for the $Ti_{67}Nb_{22}Mo_{11}$ alloy.

4.4 GIXRD

4.4.1 X-Ray diffraction patterns

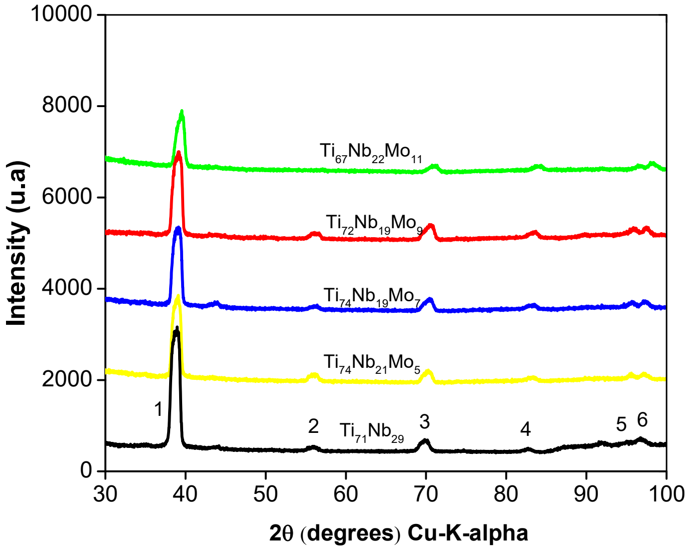

Figure 4.19 – X-ray diffractograms for the Ti-Nb and Ti-Nb-Mo samples.

In Figure 4.19 are presented the diffractograms for the deposited Ti-Nb and Ti-Nb-Mo coatings. In order to facilitate identification, each peak was numbered from 1 to 6. Table 4.4 presents the indexation of the diffraction peaks. As can be observed, all the characteristic planes of the β Ti phase are identified as follows: (110), (200), (211), (220), and (310), as well as other peaks related to Nb and Mo-Nb patterns. The majority of the peaks are overlapped with others, for instance: peak number 1 (110), corresponds to β-Ti, but also corresponds to Nb, Mo-Nb, and the (111) of Mo.

Table 4.4 – Indexation of the crystallographic planes and the corresponding card number.

Peak	**2θ**	**Element**	**Plane (*hkl*)**	**Card number**
1	38.98	Beta-Ti	110	44-1288
1	38.98	Nb	110	89-5291
1	38.98	Mo-Nb	110	65-5786
1	38.98	Mo	111	88-2331
2	56.10	Beta-Ti	200	44-1288
2	56.10	Nb	200	89-5291
2	56.10	Mo-Nb	200	65-5786
3	70.46	Beta-Ti	211	44-1288
3	70.46	Nb	211	89-5291
3	70.46	Mo-Nb	211	65-5786
4	83.42	Beta-Ti	220	44-1288
4	83.42	Nb	220	89-5291
4	83.42	Mo-Nb	220	65-5786
5	95.34	Beta-Ti	310	44-1288
5	95.34	Nb	310	89-5291
6	97.14	Mo-Nb	321	65-5786

The β-Ti phase is entirely identified, and being it a metastable phase, it is important to point out that no signal of CP-Ti, α-Ti, or metastable phases, as ω-phase, were detected in the diffractograms. Ti is alloyed with Nb and Mo, both of them exhibit bcc crystal structure and are elements that highly contribute to the β phase stabilization [58, 76]. This is in line with the thermodynamic calculation results seen previously. In spite of being calculations in equilibrium, they predict the exclusive occurrence of the β phase above the β-transus temperature. Although the films are formed out of equilibrium, the XRD results corroborate the presence of only the β phase.

The molybdenum equivalent (Mo_{eq}) was calculated for each composition and the results are presented in Table 4.5 It is well known that a Mo_{eq} value higher than 10 wt.% is sufficient to guarantee the β phase stabilization (at the same time, Nb is also a β-stabilizer) [76], however, as calculated here, values between 16 to 25 wt.% in Mo_{eq} were obtained for the samples containing Mo and the sample with no Mo, indicating strong β phase stabilization. Table 4.6 includes e/a ratios, which are related to the formation of the ω phase. According to the Collins' criteria

[54, 55], as can be seen in Figure 2.22, the e/a values obtained here are within the range of values for the ω phase formation; however, this phase was not detected by XRD.

Table 4.5 – Mo_{eq} results showing values far beyond the minimum for the β phase stabilization, and comparison with results from the literature [76].

Sample	**Ti (wt.%)**	**Nb (wt.%)**	**Mo (wt.%)**	**Mo_{eq} (wt.%)**
S1	59.3	32.7	8.0	17.17
S2	59.6	29.7	10.7	19.04
S3	57.1	29.3	13.6	21.79
S4	51.3	32.7	16.0	25.19
S5	55.8	44.2	0	12.38
+Chelariu *et.al.*	88	0	12	12
+	82	8	10	12.24
+	76	16	8	12.48
+	70	24	6	12.72
+	64	32	4	12.96

As can be seen in Figure 4.19, as Mo concentration increases, the intensity of #1 peak decreases and is slightly shifted to the right. Additionally, there was a slight shift to the right for all peaks as well. A similar behavior was previously reported by our research group for Ti-Nb coatings deposited on AISI 316L stainless steel substrate [97]. The authors observed positional shifts, along with an initial enhancement followed by a gradual reduction in the intensity of the (110) peak as the Nb concentration increased. This peak displacement was also observed by Myslyvchenko *et al.* [72] for different Ti-Nb-Mo compositions.

The Nb and Mo atomic radii are smaller than the Ti one, even though not considerably different, thus Nb and Mo have large miscibility in the β-Ti phase. As the Nb and Mo atoms replace Ti in the substitutional solid solution, they cause distortion in the lattice and modify the interplanar distances, consequently causing changes to the lattice parameter that give rise to the peak shifts and differences in the intensities that are observed in the diffractograms displayed in Figure 4. 20. These lattice distortions lead to strain and internal stress. The lattice parameters for the alloy coatings were calculated using the interplanar distances (d) of equation (4) and employing the Crystallographica SearchMatch 2.1.1.1 software. The values obtained are summarized in Table 4.6 showing the variations in lattice parameter, as expected. It was observed that there was a decrease in lattice parameter, and this can be explained by the deformations induced by the addition of Mo.

Table 4.6 – Interplanar distances and lattice parameters for the coatings.

Mo (at.%)	d (Å)	a (Å)		e/a
0	2.3248	3.2877	-	4.2
5	2.3087	3.2649	↓	4.31
7	2.285	3.2314	↓	4.33
9	2.2962	3.2473	↑	4.37
11	2.2795	3.2237	↓	4.44

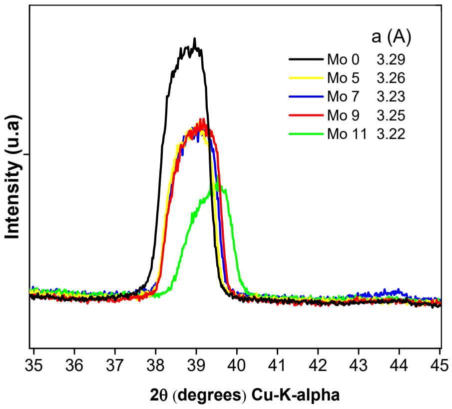

Figure 4.20 – Details of the intensity variations and position shifts for the XRD β-Ti (110) peak (#1 peak).

4.4.2 Residual Stress

The residual stresses were measured by means of GIXRD technique. Two groups of residual stress measurements were carried out. Compressive and tensile residual stress values were obtained, and the results are summarized in Table 4.7 The residual stress evolution is illustrated in Figure 4.21.

As can be seen in Table 4.7, there is a predominance of compressive stresses for all alloy coatings, although tensile stresses occurred for the coatings with 5, 9, and 11 at% Mo. A maximum compressive stress (i.e. -2557 MPa) was measured for the sample with 7 at% Mo, a value far higher than those obtained for the other samples that presented average stress values in the range of -488 and -700 MPa. These results agree with the fact that in sputtering deposition energetic particles bombard the substrate and the film producing preferentially compressive residual stresses. In a first attempt to correlate the residual stresses with some of the results, such as lattice parameter, elastic modulus, thickness, or deposition parameters (i.e. working pressure inside the chamber, temperature during deposition), no correlation was found. This is a very different scenario as compared to the studies reported in the literature, in which the residual stresses are correlated, in most cases, to the deposition parameters (working pressure and/or bias voltage), grain size, and thickness. For instance, compression stresses have been associated with low working pressures [83], Extrinsic residual stresses that appear during cooling after deposition, due to differences in thermal expansion coefficients (thermal mismatch) between the constituent elements of the coating, are probably one of the contributions of the resulting residual stresses. The arrangement of Ti, Nb, and Mo atoms can induce stress due to surface energy minimization during the early stages of the film growth, in which island coalescence occurs. The differences in the atomic radius of elements can also induce residual stress due to the lattice strain.

On the other hand, a correlation between surface morphology/topography and residual stress was observed, specifically with the occurrence of clusters and pores on the film surface. The wider view images with a 700x magnification that are displayed in Figure 4.2 exhibit these topological/morphological aspects. In order to facilitate the understanding of these images, the percentages per area of the clusters and pores were calculated, and results are also shown in Table 4.7. In Figure 4.21 are illustrated the residual tensile – compressive stresses as function of the Mo concentration in the Ti-Nb-Mo coatings, correlated with the percentages of clusters and pores on the surface.

Table 4.7 – Correlation between tensile – compressive residual stresses and the percentage of clusters and pores in the films surface.

Mo (at.%)	**Residual Stress (MPa) group 1**	**Residual Stress (MPa) group 2**	**Clusters (%)**	**Pores (%)**
0	-67 ± 11	-510 ± 26	-	-
5	51 ± 2	-489 ± 336	33	27
7	-17 ± 3	-2557 ± 13	910	18
9	35 ± 2	-700 ± 6	100	24
11	195 ± 19	483 ±188	28	100

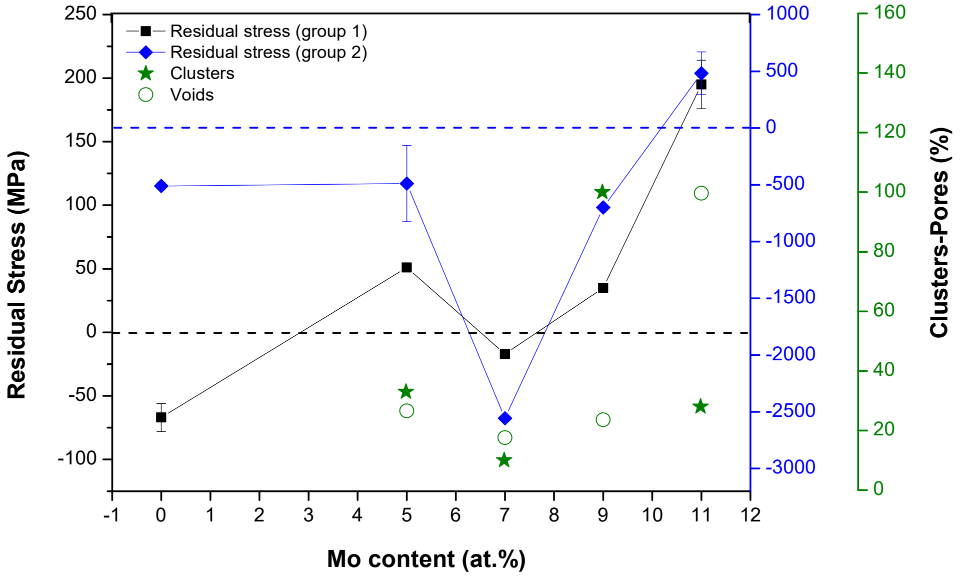

Figure 4.21 – Residual tensile and compressive stresses as function of the Mo concentration for the Ti-Nb-Mo coatings, correlated with the percentage of clusters and pores on the surface.

The $Ti_{74}Nb_{21}Mo_5$ coating (S1) presents 33% of clusters, uniformly distributed on the surface and 27% of pores (Figure 4.2 a). The $Ti_{74}Nb_{19}Mo_7$ coating (S2) exhibits the higher grade of surface uniformity, with only 10% of clusters and 18% of pores (Figure 4.2.b). In contrast, the $Ti_{67}Nb_{22}Mo_{11}$ coating (S4) presents a much higher quantity of pores (100%) than the other samples and 28% of pores (Figure 4.2 d). In contrast, the $Ti_{72}Nb_{19}Mo_9$ coating (S3) exhibits the highest quantity of clusters (100%), several of them much larger than those for the other coatings, and 24% of pores. The highest compressive stress value was observed for the $Ti_{74}Nb_{19}Mo_7$ coating (S2), and this result is in accordance with results reported in the literature that demonstrated that the higher uniformity on the film surface, the higher compressive stress values are expected. This is because a uniform film surface presents less pathways for stress relaxation as compared to a rough surface. In rough films, imperfections or irregularities act as release points for stress. Chason *et. al.* [84] described that as the film thickness enlarges, the residual stress becomes compressive, and the surface morphology is uniform and characteristic of polycrystalline films. Since uniform films usually have better atomic packing density due to control in the deposition parameters, which lead to more densification, this can result in compressive stress. In sputtering deposition, a smoother and continuous film ensures that strain from any lattice mismatch, if it occurs, is distributed more uniformly across the surface. This uniform strain also contributes to compressive stress rather than being localized and relaxed at surface defects or irregularities. However, if intrinsic stress mechanisms, such as grain growth or void formation, dominate, surface uniformity may have less impact, making stress more dependent on the material properties and less on the film surface topography [84].

Only tensile stress occurred in the $Ti_{67}Nb_{22}Mo_{11}$ coating (S4), on account of the fact that the higher presence of voids leads to more residual tensile stress. High mobility of adatoms promotes denser films that result in compressive residual stresses. If the adatoms present low mobility it is more likely to result in tensile stress, owing to the formation of voids or incomplete atomic bonding. Alternatively, this coating has the highest concentration of Mo (11% at.), and as a consequence of its higher melting point, it can contribute with lesser atomic mobility that yields to additional tension [94].

The $Ti_{74}Nb_{21}Mo_5$ coating (S1) presents less tensile stress (less voids) than the $Ti_{67}Nb_{22}Mo_{11}$ coating (S4), 51 ± 2 MPa versus 483 ±188 MPa, but more tensile stress than the $Ti_{72}Nb_{19}Mo_9$ coating (S3), 51 ± 2 MPa versus 35 ± 2 MPa. Conversely, the $Ti_{72}Nb_{19}Mo_9$ coating (S3) presents more compressive stress (-700 ± 6 MPa) than S1 (-489 ± 336), due to its higher percentage of clusters. Nevertheless, it is important to pay special attention to the fact that these relationships depend on the particular system being studied, in other words, the mechanisms that produce stress and the specific deposition conditions. It must not to be forgotten that the accumulation of one or another type of stress can lead to detrimental effects, for instance, the formation of extended lattice imperfections, three-dimensional voiding, and micro-cracking. Compressive stress is typically better for adhesion and durability but must be controlled to avoid over-compression and delamination. Tensile stress can compromise mechanical performance, making the film prone to cracking under load or thermal cycling.

4.5 Hardness and Elastic modulus

Measurements of hardness and elastic modulus were carried out and the results are summarized in table 4.7. The hardness decreases as Mo concentration increases, except for S3 (9% at. Mo). Figure 4.22 presents a chart of the correlation between hardness and Young's modulus with Mo concentration. Conversely, the elastic modulus follows an incremental tendency, and once again this is not in agreement with the typical cases reported in the literature. For these cases, it is expected that the hardness and elastic modulus follow the same tendency. As reported earlier by Peiyou [75], it was observed a decreasing in hardness values, attributed to the desapperearance of the α" phase. Constrasting with the present work, they observed for both hardness and elastic modulus a decreseasing with the increasing in Mo concentration.

Table 4.9 and Figure 4.23 display the correlation between the lattice parameter and elastic modulus. As the lattice parameter decreases, the elastic modulus increases, which is the same behavior displayed by bulk material.

Table 4.8 – Hardness and elastic modulus values obtained for the Ti-Nb and Ti-Nb-Mo coatings.

Mo (at.%)	**H (GPa)**	**E (GPa)**
0	7 ± 1	95 ± 5
5	6 ± 1	127 ± 24
7	4 ± 0.4	164 ± 14*
9	5 ± 0.5	141 ± 9
11	4 ± 0.4	190 ± 43

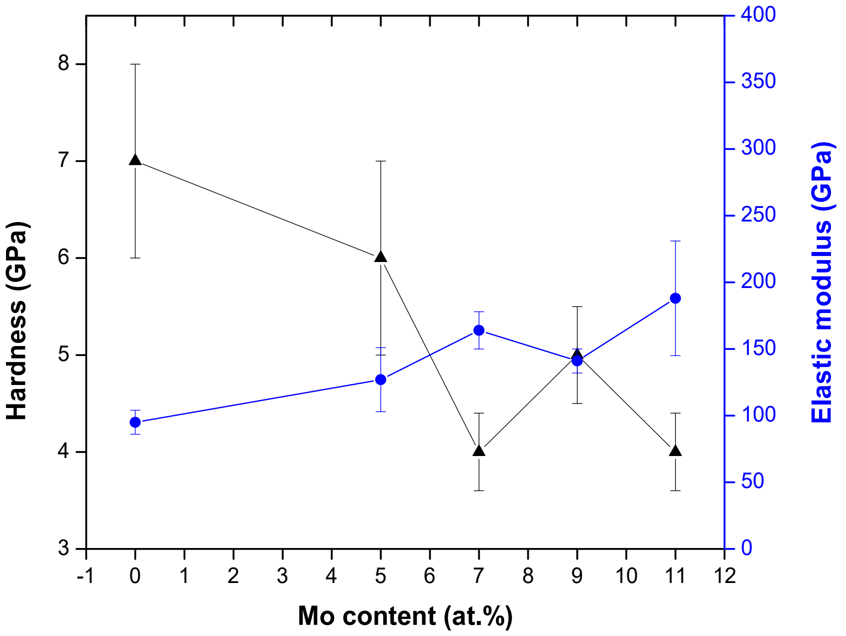

Figure 4.22 – Correlation between Mo concentration with hardness and elastic modulus.

Table 4.9 – Elastic modulus and lattice parameter trends.

Mo (at.%)	a (Å)		E (GPa)	
0	3.2877	-	95 ± 5	-
5	3.2649	↓	127 ± 24	↑
7	3.2314	↓	164 ± 14	↑
9	3.2473	↑	141 ± 9	↓
11	3.2237	↓	188 ± 43	↑

Materials with uniform bonding and minimal microstructural defects present a stronger relationship between the elastic modulus and hardness, however, despite the elastic modulus and the hardness are related, they describe different mechanical phenomena. Microstructural variations and deformation mechanisms can introduce deviations. For example, grain size, defects, and phase distribution can directly influence hardness independently of elastic modulus (e.g. grain boundary strengthening). In this work, it is observed that deformation mechanisms like atomic peening and atom mobility contribute to obtaining these characteristic results for both hardness and elastic modulus.

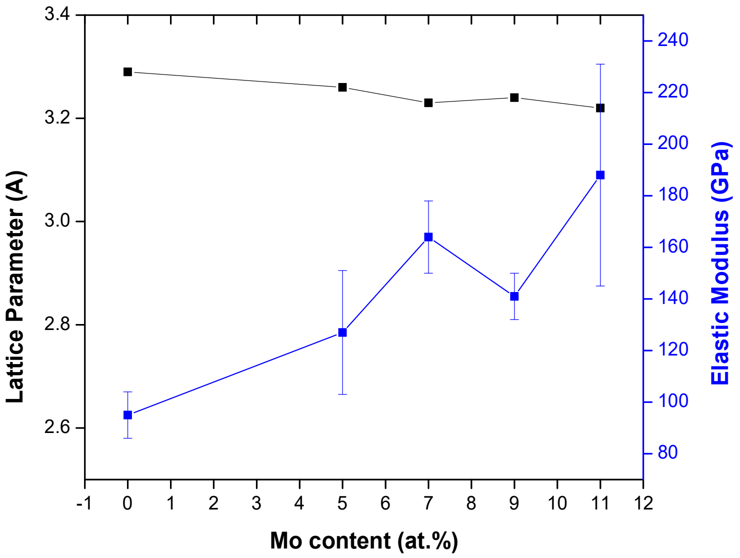

Figure 4.23 – Correlation between Mo concentration with lattice parameter and elastic modulus.

As a matter of fact, a hardness test involves localized deformation, while an elastic modulus test measures bulk properties, and this can lead to discrepancies, as in this case that shows a different trend of hardness. The hardness represents the material resistance to permanent deformation (i.e. indentation, scratching, etc.) and such kind of deformation may include contributions from intrinsic factors (atomic bonding, crystal structure) and/or extrinsic factors (microstructure, defects, and grain size).

As seen in section 4.1, the grain size decreases as Mo content increases, however, the hardness values are not increasing, so it does not obey the Hall-Petch relationship that establishes that a strengthening of the material is expected after grain refinement. Contrary, at critical grain size values (below ~100 nm), the relationship breaks down and materials can exhibit the so-called inverse Hall-Petch behavior in which an extreme grain refinement weakens the material. This can be attributed to mechanisms like grain boundary sliding or diffusion in which grain boundaries can slide, diffuse, or rearrange under stress, weakening the material instead of strengthening it. Since grain boundaries act as barriers to dislocation motion, smaller grains (less than ~100 nm) may not have enough space for dislocations to exist or operate effectively. Malygin [110] studied the breakdown of the Hall-Petch law in microcrystalline and nanocrystalline materials and explained that dislocation sinking occurs at the grain boundaries of nanocrystalline materials. Thus, the plastic deformation can occur by other deformation mechanisms such as grain boundary-mediated processes (e.g., Coble creep diffusional flow). A deformation process dominated by dislocation movement may shift to a process dominated by grain boundary. In nanometric grain sizes, grain boundaries represent a significant fraction of the material's volume, and a higher number of grain boundaries leads to an increase in atomic disorder, consequently reducing the cohesive strength, weakening the material, and causing softening as grain boundaries become more prone to deformation, which can be manifested in a hardness (strength) decrease, as was observed here.

Additionally, a correlation between the hardness values and the defects present in the coatings was observed, as can be seen in Table 4.10. The hardness value is higher for samples with a higher percentage of clusters ($Ti_{74}Nb_{21}Mo_5$ coating with 33% of clusters and $Ti_{72}Nb_{19}Mo_8$ coating with100% of clusters), and lower in samples with higher percentage of pores ($Ti_{74}Nb_{19} Mo_7$ coating with 18% of pores and $Ti_{67}Nb_{22}Mo_{11}$ coating with 100% of pores). Even though the grain sizes obtained here are larger than the critical grain sizes reported in the majority of published articles (less than 30 nm), the anomalous observed strength-hardness behavior evidences an inverse Hall-Petch relationship, with contribution from the defects within the film, i.e. pores and clusters. Such a breakdown in the Hall–Petch relationship can be attributed to different deformation mechanisms that become dominant once the grain size is reduced below a critical value. The calculated $d^{-1/2}$ values that are presented in Table 4.11 corroborate the inverse Hall-Petch behavior observed for the Ti-Nb-Mo coatings. The corresponding dispersion chart is displayed in Figure 4.24, showing the correlation between hardness and the $d^{-1/2}$ factor of the Hall-Petch relationship.

Table 4.10 – Hardness values and defects percentages for the Ti-Nb-Mo coatings.

Mo (at.%)	**H (GPa)**		**Clusters (%)**	**Pores (%)**	**Grain size (nm)**
0	7 ± 1	-	-	-	62.72
5	6 ± 1	↓	33	27	133.82
7	4 ± 0.4	↓	10	18	114.09
9	5 ± 0.5	↑	100	24	89.05
11	4 ± 0.4	↓	28	100	70.05

Table 4.11 – Values obtained for the d-1/2 factor of the Hall-Petch law.

Sample	**H (GPa)**	**$d^{-1/2}$ ($nm^{-1/2}$)**
S1	6 ± 1	0.086
S2	4 ± 0.4	0.094
S3	5 ± 0.5	0.106
S4	4 ± 0.4	0.119
S5	7 ± 1	0.126

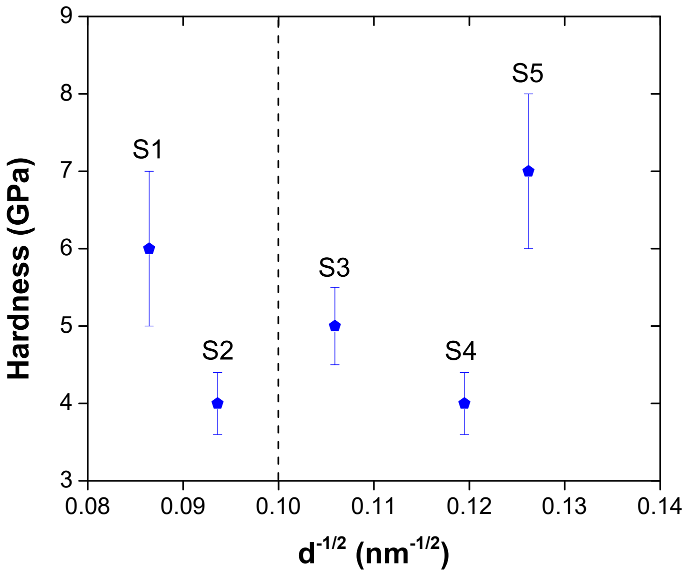

Figure 4.24 – Correlation chart of hardness and the d-1/2 factor of Hall-Petch law.

From Table 4.10 it can be noticed that the $d^{-1/2}$ factors for the S1 and S2 coatings are lower than the 0.1 nano-crystallinity criteria, indicating a factor for micro-sized grains (grain size > 100 nm), however it is evident the anomalous behavior even for the smallest grain size observed for the Ti-Nb reference sample ($Ti_{71}Nb_{29}$ coating). Even though both S1 and S2 exhibit “no nanometric” grains, the hardness values are decreasing. A similar behavior was observed by Meyers *et al.* [30] for Ti samples (Figure 2.14).

Alternatively, the decreasing of hardness observed in this work can also be correlated with the great number of porous present in the coatings, in spite of the notable variation in the porous percentage from one sample to another, being S4 the one having the greatest amount. This trend is in perfect agreement with some published results, for instance, Lu *et al.* [32] reported the inverse Hall-Petch behavior for Ni-P thin films for a $d^{-1/2}$ factor < 0.1 (Figure 2.15).

Ankit *et al.* [33]. noticed that high values of porosity parameter included in the simulation to assess the hardness behavior caused mechanical instability of the samples; reductions in hardness and strength were observed.

A similar behavior was observed by Duan *et al.* [34] for extremely fine nano-grained Mo thin films; they argued that the inverse Hall-Petch law was influenced by grain sizes smaller than 11 nm and also by porosity in some of the films.

4.6 Corrosion Resistance for the Ti-Nb-Mo Coatings: Potentiodynamic Polarization Test

The Ti-Nb binary and Ti-Nb-Mo ternary alloy coatings have been tested by potentiodynamic polarization method in a chloride medium, and both the corrosion potential (E_{corr}) and transpassivation potential (E_t) were measured. The experiments were conducted at room temperature. The plotted polarization curves are displayed in Figure 4.25 and data results are presented in Table 4.12, that includes additional information, as percentage of pores within the Ti-Nb-Mo coatings. It can be noticed in the polarization chart that all samples maintain a E_{corr} value close to each other. The E_{corr} values remain in a range between -275 and -296 mV. It starts with -290.6 mV for S1, then E_{corr} decreases to -295.7 mV for both S2 and S3, and in sequence it raised to -274.6 mV for S4. E_{corr} starts to get more negative up to 9 at.%, but with a even higher amount of Mo (11 at.%), the E_{corr} has the smallest value among all coatings. Analyzing E_{corr} in relation to the Nb amount, it can be seen that the two samples with higher Nb content, S1 and S4, E_{corr} tends to increase, exhibiting a less negative behavior. Conversely, the Ti-Nb coating presents the most negative E_{corr} value. This behavior observed for S1 and S4 agrees with some studies published in the literature that report about the passivation enhancement with the Nb addition in different binary and ternary alloys. For instance, Martinez-Orozco *et al.* [68] reported a progressive decrease in E_{corr} with the increase in the Nb concentration in Ni-Nb alloys, and a strong passivation behavior was also observed for some Nb concentrations. A better passivation behavior for Ti-Nb alloys as compared with Ti-Mo and CP-Ti [79, 80].

Nonetheless, it can be perceived that the transpassivation potential (E_t), present significantly higher values in contrast with E_{corr} up to S4. E_t rises almost to 1500 mV, but once Mo content is augmented to 11%, an abrupt drop occurs. At the same time, S4 exhibits the higher i_{corr} among all samples. This could mean that, in spite of S4 having the higher content of Nb, further Mo additions seen to induce a deleterious effect in the corrosion resistance, however another possible, and more plausible, explanation is related to the coating morphology. As expected from published studies previously menioned, the $Ti_{71}Nb_{29}$ coating (S5) exhibits a good passivation behavior (difference between E_{corr} and E_t), but not as good as S1, S2 and S3, which present a nobler E_t. This may help to corroborate that Mo indeed improves the corrosion resistance.

Table 4.12 – Potentiodynamic polarization test results for the Ti-Nb-Mo coatings.

Sample	**Composition**	**E_{corr} (mV)**	**E_{transp} (mV)**	**$\|E_{corr} - E_t\|$**	**I_{corr} (Acm^{-2})**	**Pores (%)**
S1	$Ti_{74}Nb_{21}Mo_5$	-290.65	1397.64	1688.29	3.92×10^{-8}	27
S2	$Ti_{74}Nb_{19}Mo_7$	-295.70	1397.64	1693.34	4.12×10^{-8}	18
S3	$Ti_{72}Nb_{19}Mo_9$	-295.71	1493.68	1800.57	4.66×10^{-8}	24
S4	$Ti_{67}Nb_{22}Mo_{11}$	-274.64	711.87	985.2	6.77×10^{-8}	100
S5	$Ti_{71}Nb_{29}$	-344.57	1050.54	1397.21	5.41×10^{-8}	-

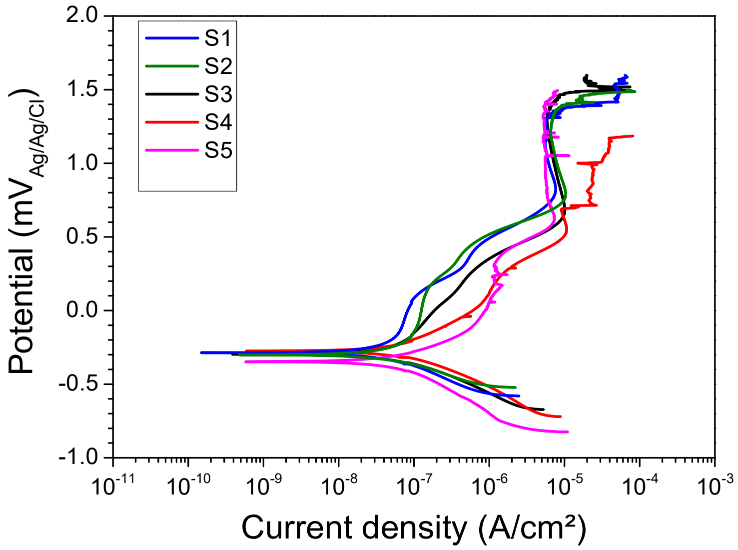

Figure 4.25 – Plot of potentiodynamic polarization curves for (S1) $Ti_{74}Nb_{21}Mo_5$, (S2) $Ti_{74}Nb_{19}Mo_7$, (S3) $Ti_{72}Nb_{19}Mo_9$, (S4) $Ti_{67}Nb_{22}Mo_{11}$, and S5) $Ti_{71}Nb_{29}$.

In contrast with seeking a correlation of corrosion resistance with coating morphology for the $Ti_{67}Nb_{22}Mo_{11}$ coating (S4), the high percentage of pores exhibited by this sample, as displayed in Figure 4.2 and Table 4.11, could be an alternative plausible explanation for such decay in the corrosion resistance, as illustrated in Figure 4.26. The more porous a structure is, the greater is the number of reactive sites, which can lead to an anticipated onset of transpassivation potential, as occurs for S4. Its anodic region is clearly below the other ones for the Ti-Nb-Mo coatings. The electrolytic dissolution may stay stagnant within the pores, thus, creating “micro-environments” with a different concentration of species (i.e. ions), which represent a starting point for localized corrosion, consequently diminishing the E_t or producing irregular transpassivation along the coating. Contrary to the Nb and Mo content which tend always to improve the corrosion performance. The $Ti_{74}Nb_{19}Mo_7$ coating (S2), which has the most uniform and homogeneous surface, exhibits a good balance between the passivation behavior with acceptable i_{corr} value among all the samples.

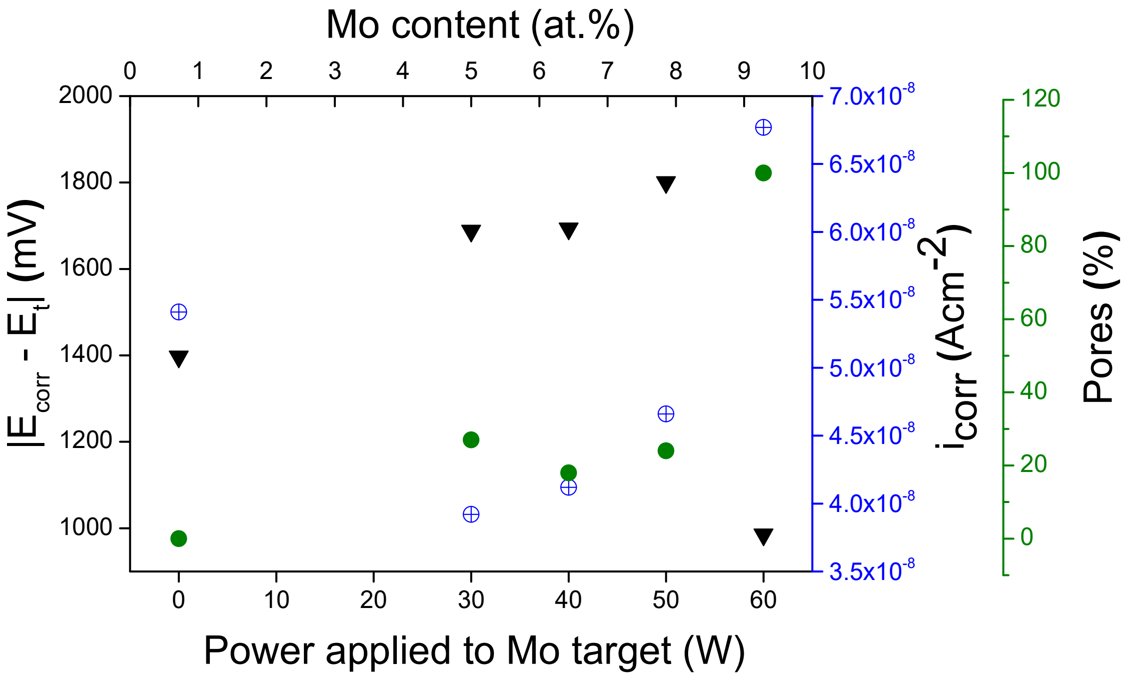

Figure 4.26 – Correlation between $|E_{corr} - E_t|$ (mV), i_{corr} (Acm^{-2}) and pores percentage versus power applied to to the Mo target and Mo at.%.

5 CONCLUSIONS

In the present exploratory work, four different compositions of Ti-Nb-Mo alloy coatings were deposited on AISI 316L stainless steel substrate by means of DCMS PVD process, as well as one Ti-Nb coating as reference. From the microstructural and mechanical characterization results, it can be concluded the following:

1. The compositions obtained by EDS were $Ti_{74}Nb_{21}Mo_5$ (S1), $Ti_{74}Nb_{19}Mo_7$ (S2), $Ti_{72}Nb_{19}Mo_9$ (S3), and $Ti_{67}Nb_{22}Mo_{11}$ (S4), for the ternary alloy coatings, with corresponding thicknesses were: 671, 573, 841, and 963 nm. The composition for the binary alloy was also obtained: $Ti_{71}Nb_{29}$ (S5).
2. Homogeneous distributions of all constituent elements for all coatings were corroborated by EDS chemical mapping.
3. SEM images revealed the presence of defects on the coating surfaces, i.e. clusters (agglomerates of grains), as well as different grades of porosity. S4 was the most porous coating, while S3 had the highest number of clusters. S2 exhibited the most uniform surface with low concentration of clusters and pores. An EDS analysis of the pores revealed that the depth reached the substate surface. Both the grain size and the roughness decreased with the increase in Mo content. However, the $Ti_{71}Nb_{29}$ coating exhibited even smaller grain size, perhaps due to the fact that Nb is a strong grain refiner.
4. The alloy coatings exhibited compact and columnar grains, identified as a combination of zone I and T (competitive growth) for S1 and S2, and zone T and II in S3 and S4.
5. The GIXRD results revealed that the coatings were formed exclusively by the β-phase, and this was expected due to the fact that Nb and Mo are strong β-stabilizers, and Mo_{eq} calculation showed values much higher than 10%, which is the value that stabilizes the β-phase.
6. GIXRD peak shifts and intensity changes were observed, since Mo and Nb cause deformation in the interplanar distance and, consequently, in the lattice parameter.

7. An increment in the elastic modulus was observed, in accordance with the decreasing in lattice parameter.
8. Residual stress was measured by GIXRD, and two groups of results were obtained, showing compressive and tensile stresses. An expressive value was observed for S2, which was the coating with the most uniform surface. Uniform films tend to accumulate more compressive stresses due to the scarce presence of points of relaxation. Compressive stresses are more desirable than tensile ones, but an equilibrium, depending on the application, must be considered. Only tensile stress occurred for S3, consistent with the higher concentration of pores.
9. Unexpected results in hardness were measured. It decreased with the decrease in grain size, which is a counterintuitive behavior explained by the breakdown of the so-called Hall-Petch law. This is due to the fact that the Hall-Petch law cannot be applied at certain critical $d^{-1/2}$ values (i.e. > 0.1) for nanometric grain sizes (≤ 100 nm). However, in this work the inverse Hall-Petch effect was observed even for $d^{-1/2}$ values < 0.1, and this had been also reported in the literature for other alloys.
10. The potentiodynamic polarization test results showed a similar behavior among S1, S2, and S3, which exhibited good corrosion resistance in comparison with the TiNb sample (S5).
11. The worst corrosion behavior was observed for S4, associated with the higher pore concentration.
12. The best behavior was observed for S2, that exhibited a good combination between the E_{corr} and E_t difference and the i_{corr}.

6 SUGGESTIONS FOR FURTHER RESEARCH

- Perform impedance tests in order to evaluate the corrosion behavior in more detail.
- Create a library of the chemical composition of each group of samples, dividing each sample in regions, in order to assess a more accurate value for chemical composition, due to the variations that are intrinsic of the type of deposition process.
- Create computational models to understand why and how the agglomerate of grains form, also the particular way the pores constitute.
- Perform cell adhesion experiments to evaluate biocompatibility.

7 REFERENCES

[1] D. M. Mattox, Handbook of Physical Vapor Deposition (PVD) Processing, second ed., New York: William Andrew, 2010.

[2] D. Brunette, P. Tengal, M. Textor, P. Thomsen, Titanium in Medicine: Material Science, Surface Science, Engineering, Biological Responses and Medical Applications, first ed., New York: Springer, 2012.

[3] K. Wasa, I. Kanno, and H. Kotera, Handbook of Sputter Deposition Technology: Fundamentals and Applications for Functional Thin Films Nano-Materials and MEMS, second ed., New York: William Andrew, 2012.

[4] D. A. Tallarico, A. L. Gobbi, P. I. Paulin, M. E. Maia da Costa, and P. A. P. Nascente, “Growth and surface characterization of TiNbZr thin films deposited by magnetron sputtering for biomedical applications”, Materials Science and Engineering C, vol. 43, p. 45–49, 2014.

[5] K. Holmberg and A. Matthews, Coatings Tribology: Properties, Mechanisms, Techniques and Applications in Surface Engineering. second ed., Maryland Heights: Elsevier Science, 2009.

[6] R. Fitzpatrick, Plasma Physics: An Introduction, first ed., Boca Raton: R Press, 2015.

[7] T. M. York, H. Tang, Introduction to Plasmas and Plasma Dynamics, first ed., New York: Elsevier Science & Technology Books, 2015.

[8] A. Fridman, Plasma Chemistry, 1 st Ed., Victoria-Ca: Cambridge University Press, 2008.

[9] J. Shang and S. T. Surzhikov, Plasma Dynamics for Aerospace Engineering, Cambridge-UK: Cambridge University Press, 2018.

[10] R. K. Waits, Planar Magnetron Sputtering, Journal of Vaccum Science Technology, vol. 15, no. 2, p. 179–187, 1978.

[11] N. Hardy, What are planar magnetrons in PVD oatings? Available: http://www.semicore.com/news/66-planar-magnetron-pvd-coating

[12] J. E. Greene, Tracing the recorded history of thin-film sputter deposition: From the 1800s to 2017. Available: https://www.researchgate.net/figure/

Color-online-Upper-Illustrations-of-circular-and-rectangular-planar magnetron_fig10_319603857

[13] M. Hughes, What is DC Sputtering? Available: http://www.semicore.com /news/94-what-is-dc-sputtering

[14] VacCoat, “Balanced and Unbalanced Magnetron Sputtering” Available: https://vaccoat.com/blog/balanced-and-unbalanced-magnetron-sputtering/.

[15] D. L. Smith, Thin-film Deposition: Principles and Practice. New York: McGraw-Hill, 1995.

[16] U. W. Pohl, Epitaxy of Semiconductors: Physics and Fabrication of Heterostructures, 3rd ed. New York: Springer International Publishing AG, 2021.

[17] D. Lundin, T. Minea, and J. T. Gudmundson, High Power Impulse Magnetron Sputtering. New York: Elsevier, 2020.

[18] B. A. Movchan and A. V Demchishin, “Study of the structure and properties of thick vacuum condensates of nickel, titanium, tungsten, aluminium oxide and zirconium dioxide,” Fiz. Metal. Metalloved, 1969.

[19] H. Sabet, H. B. Bhandari, H. Kudrolli, and V. V. Nagarkar, “Fabrication of X-ray/Gamma-ray Detector by Growth of Microcolumnar CSI:Tl onto Silicon Photomultipliers” Phys Procedia, vol. 37, p. 1523–1530, 2012.

[20] A. Anders, “A structure zone diagram including plasma-based deposition and ion etching,” Thin Solid Films, vol. 518, no. 15, p. 4087–4090, 2010.

[21] P. B. Barna and M. Adamik, “Fundamental structure forming phenomena of polycrystalline films and the structure zone models” vol. 317, no. 1-2, p. 27–33,1998.

[22] K. Sarakinos, J. Alami, and S. Konstantinidis, “High power pulsed magnetron sputtering: A review on scientific and engineering state of the art,” Surf Coat Technol, vol. 204, no. 11, p. 1661–1684, 2010.

[23] J. P. Rivière, Nanostructured coatings. First ed., New York: Springer, 2007.

[24] A. Zeeshan, “Growth, Transport, And Magnetic Properties of Oblique-Angle-Deposited Permalloy Thin Films.” Available: https://www.researchgate.net/figure/a-The-Movchan-and-Demchishin-structure-zone-model-14-b-Thornton-structure-zone_fig2_334683586

[25] M. H. Grabow, G. H Gilmer, Thin Film Growth Modes, Wetting and Cluster Nucleation, Surface Science, vol. 194, no. 3, p. 333–346, 1988.

[26] J. Johansson, “Heteroepitaxial growth modes revisited,” CrystEngComm, vol. 25, no. 48, p. 6671–6676, 2023.

[27] A. Baskaran and P. Smereka, “Mechanisms of Stranski-Krastanov growth,” J Appl Phys, vol. 111, no. 4, 2012.

[28] C. Suryanarayana, Nanocrystalline materials, International Materials Reviews, vol. 40, no. 2, p. 41–64,1995.

[29] S. N. Naik and S. M. Walley, “The Hall–Petch and inverse Hall–Petch relations And the hardness of nanocrystalline metals”, Journal of Materials Science, vol. 55, no. 7, p. 2661–268, 2020.

[30] M. A. Meyers, A. Mishra, and D. J. Benson, “Mechanical properties of nanocrystalline materials,” Progress in Materials Science, vol. 51, no. 4, p. 427–556, 2006.

[31] A. H. Chokshi, A. Rosen, J. Karch, and H. Gleiter, “On the Validity Of The Hall-Petch Relationship In Nanocrystalline Materials”, Scripta Metallurgica, vol. 23, no. 10, p. 1670–1683, 1989.

[32] K. Lu, W. Wei, and J. Wang, “Microhardness and fracture properties of nanocrystalline Ni-P alloy”, Scripta Metallurgica et Materialia, vol. 24, no. 12, p. 2319–2323, 1990.

[33] A. Yadav, L. Bajtošová, M. Cieslar, and J. Fikar, “Two-phase model for inverse Hall–Petch effect in nanocrystalline thin film: Atomistic simulation study,” Acta Materialia, vol. 276, p. 120084, 2024.

[34] F. H. Duan, Y. Naunheim, C. A. Schuh, and Y. Li, “Breakdown of the Hall-Petch relationship in extremely fine nanograined body-centered cubic Mo alloys,” Acta Materialia, vol. 213, p. 116950, 2021.

[35] P. Ducheyne, Comprehensive Biomaterials, vol. 53, no. 9. 2012.

[36] K. C. Dee, D. A. Puleo, and R. Bizios, Tissue- Biomaterial Interactions. New York: Wiley-Liss, Inc.2002.

[37] Z. Xia, S. Jin, and K. Ye, “Tissue and Organ 3D Bioprinting.” Available: https://journals.sagepub.com/doi/10.1177/2472630318760515

[38] V. V. Divya Rani, L. Vinoth-Kumar, V. C. Anitha, K. Manzoor, M. Deepthy, and V. N. Shantikumar, “Osteointegration of titanium implant is sensitive to specific nanostructure morphology,” Acta Biomater, vol. 8, no. 5, p. 1976–1989, 2012.

[39] L. D. Zardiackas, M. J. Kraay, and H. L. Freese, Titanium, Niobium, Zirconium and Tantalum for Medical and Surgical Applications. ASTM International, 2012.

[40] S. John Mary and S. Rajendran, “Corrosion behaviour of SS 316L in artificial blood plasma in presence of amoxicillin” Portugaliae Electrochimica Acta, vol. 31, no. 1, p. 33–40, 2013.

[41] Arcelor Mittal, “Industeel UR TM 316L”, Available: https://www.corporate.arcelormittal.com/

[42] M. Long and H. J. Rack, “Titanium alloys in total joint replacement, a materials science perspective,” Biomaterials, vol. 19, p. 1621–1636, 1998.

[43] M. Fellah, M. Labaïz, O. Assala, A. Lost, and L. Dekhil, “Tribological behaviour of AISI 316L stainless steel for biomedical applications,” Tribology - Materials, Surfaces and Interfaces, vol. 7, no. 3, p. 135–149, 2013.

[44] M. J. Donachie, Titanium - A Techinacal Guide, vol. 99, no. 5. ASM International, 2000 .

[45] J. C. Williams and G. Lütjering, “Titanium: Second Edition,” Wiley, 2007

[46] Metalary, “Titanium Price.” Available: http://www.metalary.com/titanium-price/

[47] Made in China, “Stainless Steel Prices.” Available: http://www.made-in-china.com/products-search/hot-china.com/products-search/hot-chinaproducts/316L_Stainless_Steel_Price.html

[48] D. Raabe, “Introduction to Titanium Alloys” Available: http://www.dierk-raabe.com/titanium-alloys/

[49] P. J. Bania, Beta Titanium Alloys and Their Role in the Titanium Industry, The Journal of Minerals, Metals & Materials Society, vol. 46, p. 16–19, 1994.

[50] S. Banerjee and P. Mukhopadhyay, “Phase Transformations Examples from Titanium and Zirconium Alloys”, New York: Pergamon Materials Series, 2007.

[51] E. W. Collings, The Physical Metallurgy of Titanium Alloys. New York: American Society for Metals, 1989.

[52] A. Gysler and S. Weissmann, “Effect of order in Ti3Al particles and of temperature on the deformation behavior of age-hardened TiAl alloys,” Materials Science and Engineering, vol. 27, no. 2, p. 181–193, 1977.

[53] W. Hume-Rothery and G. V. Raynor, The Structure of metals and alloys, 3rd ed,1954.

[54] G. P. Tiwari and R. V. Ramanujan, “Review The relation between the electron to atom ratio and some properties of metallic systems”, Journal of Material Science, vol. 36, p. 271–283, 2001.

[55] E. W. Collins, The Physical Metallurgy of Titanium Alloys. American Society for Metals, ASM, 1984.

[56] J. I. Kim, H. Y. Kim, T. Inamura, H. Hosoda, and S. Miyazaki, “Shape memory characteristics of Ti-22Nb-(2-8)Zr(at.%) biomedical alloys,” Materials Science and Engineering A, vol. 403, no. 1–2, p. 334–339, 2005.

[57] Y. Al-Zain, H. Y. Kim, H. Hosoda, T. H. Nam, and S. Miyazaki, “Shape memory properties of Ti-Nb-Mo biomedical alloys,” Acta Mater, vol. 58, no. 12, p. 4212–4223, 2010.

[58] S. Achache, S. Lamri, M. Arab Pour Yazdi, A. Billard, M. François, and F. Sanchette, “Ni-free superelastic binary Ti-Nb coatings obtained by DC magnetron co-sputtering,” Surf Coat Technol, vol. 275, pp. 283–288, 2015.

[59] S. Takashi, “Multifunctional Alloys Obtained via a Dislocation-Free Plastic Deformation Mechanism” 2003. Available: www.sciencemag.org

[60] S. Achache, S. Lamri, a. Alhussein, a. Billard, M. François, and F. Sanchette, “Gum Metal thin films obtained by magnetron sputtering of a Ti-Nb-Zr-Ta target,” Materials Science and Engineering A, vol. 673, p. 492–502, 2016.

[61] Ortho-Care (UK), “GUMMETAL® Titanium Niobium Archwires” Available: https://www.orthocare.co.uk/acatalog/GUMMETAL-Titanium-Niobium-Archwires-Natural-Form.html.

[62] C. K. Gupta and A. K. Suri, Extractive Metallurgy of Niobium, First. CRC Press, 1994.

[63] J. M. G. de Lima, “Relatório técnico 20: Perfil da Mineração do Nióbio” Ministério De Minas E Energia - Mme, vol. 2010, p. 49, 2010.

[64] CBMM, “Understanding Niobium: from properties to practical applications,” https://cbmm.com/en/about-niobium.

[65] E. Steifel, “Molybdenum And Molybdenum Alloys,” Kirk-Othmer Encyclopedia of Chemical Technology, 2010.

[66] G. C. K, Extractive Metallurgy of Molybdenum. CRC Press, 1992.

[67] C. M. Lee, C. P. Ju, and J. H. C. Lin, “Structure-Property Relationship of Cast Ti-Nb alloys,” J Oral Rehabil, p. 314–322, 2002.

[68] K. Martinez-Orozco, J. E. Spinelli, V. Amigó, C. A. Della Rovere, C. R. M. Afonso, and C. S. Kiminami, “Characterization, corrosion resistance and hardness of rapidly solidified Ni–Nb alloys,” Journal of Alloys and Compounds, vol. 829, p.154529, 2020.

[69] E. D. Gonzalez, T. C. Niemeyer, C. R. M. Afonso, and P. a. P. Nascente, “Ti-Nb thin films deposited by magnetron sputtering on stainless steel,” Journal of Vacuum Science & Technology A: Vacuum, Surfaces, and Films, vol. 34, no. 2, p. 021511, 2016.

[70] D. Photiou, N. T. Panagiotopoulos, L. Koutsokeras, G. A. Evangelakis, and G. Constantinides, “Microstructure and nanomechanical properties of magnetron sputtered Ti − Nb films,” Surface Coating Technology, vol. 302, p. 310–319, 2016.

[71] G. C. Cardoso et al., “Preparation and characterization of novel as-cast Ti-Mo-Nb alloys for biomedical applications,” Science Reports, vol. 12, no. 1, 11874, 2022.

[72] O. M. Myslyvchenko, A. A. Bondar, V. Voblikov, N. I. Tsyganenko, T. A. Silinska, and O. P. Gaponova, “Solidus Temperatures and Hot Hardness

of Ti– Nb–Mo Alloys," Metallofizika i Noveishie Tekhnologii, vol. 44, no. 4, p. 459–469, 2022.

[73] Y. Al-Zain, H. Y. Kim, H. Hosoda, T. H. Nam, and S. Miyazaki, "Shape memory properties of Ti-Nb-Mo biomedical alloys," Acta Materialia, vol. 58, no. 12, pp. 4212–4223, 2010.

[74] L. J. Xu, Y. Y. Chen, Z. G. Liu, and F. T. Kong, "The microstructure and properties of Ti-Mo-Nb alloys for biomedical application," Journal of Alloys and Compounds, vol. 453, no. 1–2, p. 320–324, Apr. 2008.

[75] Peiyou Li, X. Ma, T. Tong, and Y. Wang, "Microstructural and mechanical properties of β-type Ti–Mo–Nb biomedical alloys with low elastic modulus," J Alloys Compd, vol. 815, Jan. 2020.

[76] R. Chelariu, G. Bolat, J. Izquierdo, D. Mareci, D.M. Gordin,T. Gloriant, R.M. Souto. "Metastable beta Ti-Nb-Mo alloys with improved corrosion resistance in saline solution," Electrochimica Acta, vol. 137, p. 280–289, Aug. 2014.

[77] K. Li, Y. Lia, X. Huangd, D. Gibson, Y. Zheng, J. Liu, L. Sun, Y. Qing Fu "Surface microstructures and corrosion resistance of Ni-Ti-Nb shape memory thin films," Applied Surface Science, vol. 414, p. 63–67, 2017.

[78] L. H. De Almeida, I. N. Bastos, I. D. Santos, A. J. B. Dutra, C. A. Nunes, and S. B. Gabriel, "Corrosion resistance of aged Ti-Mo-Nb alloys for biomedical applications," J Alloys Compd, vol. 615, no. S1, p. S666–S669, Jan. 2015.

[79] J. Ureña, S. Tsipas, A. M. Pinto, F. Toptan, E. Gordo, and A. Jiménez-Morales, "Corrosion and tribocorrosion behaviour of β-type Ti-Nb and Ti-Mo surfaces designed by diffusion treatments for biomedical applications," Corros Sci, vol. 140, p. 51–60, Aug. 2018.

[80] N. T. C. Oliveira and A. C. Guastaldi, "Electrochemical stability and corrosion resistance of Ti-Mo alloys for biomedical applications," Acta Biomater, vol. 5, no. 1, p. 399–405, 2009.

[81] C. R. Tomachuk, D. B. Mitton, J. Springer, T. Monetta, and F. Bellucci, "The wet corrosion of molybdenum thin film - Part III: The effect of Ti and Nb," Materials and Corrosion, vol. 57, no. 5, p. 394–399, 2006.

[82] A. Cremasco, W. R. Osório, C. M. A. Freire, A. Garcia, and R. Caram, “Electrochemical corrosion behavior of a Ti-35Nb alloy for medical prostheses,” Electrochim Acta, vol. 53, no. 14, p. 4867–4874, 2008.

[83] D. W. Hoffman, “Perspective on stresses in magnetron-sputtered thin films,” Journal of Vacuum Science & Technology A: Vacuum, Surfaces, and Films, vol. 12, no. 4, p. 953–961,1994

[84] E. Chason and P. R. Guduru, “Tutorial: Understanding residual stress in polycrystalline thin films through real-time measurements and physical models,” Journal of Applied Physics, vol. 119, no. 19, p. 191101, 2016

[85] A. M. Engwall, Z. Rao, and E. Chason, “Origins of residual stress in thin films: Interaction between microstructure and growth kinetics,” Mater Des, vol. 110, p. 616–623, 2016.

[86] M. Huff, “Review Paper: Residual Stresses in Deposited Thin-Film Material Layers for Micro- and Nano-Systems Manufacturing”, MDPI, Micromachines, vol. 13, p. 2084, 2022.

[87] L. B. S. S. Freund, Thin Film Materials: Stress, Defect Formation and Surface Evolution. Cambridge-UK: Cambridge University Press, 2004.

[88] M. Ohring, Materials Science of Thin Films Deposition and Structure, 2nd ed. New Jersey: Elsevier, 2002.

[89] D. W. Hoffman and J. A. Thornton, Internal Stresses In Sputtered Chromium, Thin Solid Films, vol. 40, p.355-363 1977.

[90] H. Windischmann, “An intrinsic stress scaling law for polycrystalline thin films prepared by ion beam sputtering,” Journal of Applied Physis, vol. 62, no. 5, p.1800–1807, 1987.

[91] E. Chason, B. W. Sheldon, L. B. Freund, J. A. Floro, and S. J. Hearne, “Origin of Compressive Residual Stress in Polycrystalline Thin Films,” Phys Rev Lett, vol. 88, no. 15, p. 4, 2002.

[92] M.-W. Moon, J.-W. Chung, K.-R. Lee, K. H. Oh, R. Wang, and A. G. Evans, “An experimental study of the influence of imperfections on the buckling of compressed thin films,” 2002. Available: www.actamat-journals.com

[93] J. S. Wang and A. G. Evans, “Effects Of Strain Cycling On Buckling, Cracking And Spalling Of A Thermally Grown Alumina On A Nickel-Based Bond Coat”, Acta Materialia, vol. 47, p. 699-710, 1999.

[94] R. Abermann, “Measurements of the intrinsic stress in thin metal films”, Vacuum, vol. 41, p. 1279-1282, 1990.

[95] D. Yang, Z. Guo, H. Shao, X. Liu, and Y. Ji, “Mechanical properties of porous Ti-Mo and Ti-Nb alloys for biomedical application by gelcasting”, Procedia Engineering, Elsevier Ltd, p. 160–167, 2012.

[96] S. Endres, M. Wilke, P. Knöll, H. Frank, M. Kratz, and A. Wilke, “Correlation of in vitro and in vivo results of vacuum plasma sprayed titanium implants with different surface topography,” Journal of Mater Science, Materials in Medicine, vol. 19, no. 3, p. 1117–1125, 2008.

[97] E. D. Gonzalez, C. R. M. Afonso, and P. a. P. Nascente, “Influence of Nb content on the structure, morphology, nanostructure, and properties of titanium-niobium magnetron sputter deposited coatings for biomedical applications,” Surface Coating Technology, vol. 326, p. 424–428, 2017.

[98] E. D. Gonzalez, C. R. M. Afonso, and P. a. P. Nascente, “Nanostructural characterization of sputter deposited Ti-Nb coatings byautomated crystallographic orientation mapping,” Thin Solid Films, vol. 661, p. 92–97, 2018.

[99] D. Simeone, G. Baldinozzi, D. Gosset, S. Le Caer, and J. F. Bérar, “Grazing incidence X-ray diffraction for the study of polycrystalline layers”, Thin Solid Films, vol. 530, p. 9–13. 2013

[100] O. Werzer, S. Kowarik, F. Gasser, Z. Jiang, J.Strzalka, C. Nicklin, R. Resel, “X-ray diffraction under grazing incidence conditions”, Nature Reviews methods primers 4, p. 16. 2024

[101] M. Azad and A. Avin, “Scanning Electron Microscopy (SEM): A Review”, Proceedings of International Conference on Hydraulics and Pneumatics – HERVEX, Sealing Elements, Tools, Precision Mechanics, Specific Electronic Equipment & Mechatronics, Romania, ISSN 1454 - 80032019.

[102] N. Jalili and K. Laxminarayana, “A review of atomic force microscopy imaging systems: Application to molecular metrology and biological sciences,” Mechatronics, vol. 14, no. 8, p. 907–945, 2004.

[103] E. G. Mota and K. Subramani, Emerging Nanotechnologies in Dentistry Processes, Materials and Applications A volume in Micro and Nano Technologies. New York: William Andrew, 2012.

[104] R. Keshavamurthy, C. S. Ramesh, G. S. Pradeep Kumar, and V. Tambrallimath, “Experimental investigation of tribocorrosion,” Tribocorrosion: Fundamentals, Methods, and Materials, p. 17–42, Jan. 2021.

[105] Z.-K. Liu, “Thermodynamics and its Prediction and CALPHAD Modeling: Review, State of the Art, and Perspectives,” 2023. Available: https://www.elsevier.com/open-access/userlicense/1.0/

[106] Geology Wonders, Clusters of Quartz – Amethyst, Available: https://www.facebook.com/photo.php?fbid=939331581555701&set=pb.100064366044691.-2207520000&type=3.

[107] F. M. Mwema, J. M. Wambua, T. C. Jen, and E. T. Akinlabi, Influence of Sputtering DC Sputtering Power on the Surface Evolution of Ti Thin Films: A Fractal Description, JOM, vol.77, no 2, 2025.

[108] V. Elofsson, D. Magnfält, M. Samuelsson, and K. Sarakinos, “Tilt of the columnar microstructure in off-normally deposited thin films using highly ionized vapor fluxes,” Journal of Applied Physics, Vol.113, no. 17, p. 174906, 2013.

[109] N. J. Suliali, W. E. Goosen, A. J. van Vuuren, E. J. Olivier, B. Bakhit, H. Högberg, V. Darakchieva, J. R. Botha, “Ti thin films deposited by high-power impulse magnetron sputtering in an industrial system: Process parameters for a low surface roughness,” Vacuum, vol. 195, p. 110690, 2022.

[110] Malygin. G. A., “Breakdown of the Hall-Petch law in micro- and nanocrystalline materials”, Physics of the Solid State, vol. 37, no. 8, p. 1248–1253, 1995.